UNIVERSIDADE ESTADUAL DE CAMPINAS
FACULDADE DE ENGENHARIA MECÂNICA
E INSTITUTO DE GEOCIÊNCIAS

JULIANA MAIA CARVALHO DOS SANTOS

DIAGNOSING RESERVOIR MODELS USING SIMILARITY INDICATORS WITH 4D SEISMIC DATA: A MULTI-DOMAIN AND MULTI-ATTRIBUTES APPROACH

DIAGNÓSTICO DE MODELOS DE RESERVATÓRIO UTILIZANDO INDICADORES DE SIMILARIDADE COM A SÍSMICA 4D: UMA ABORDAGEM MULTI-DOMÍNIO E MULTI-ATRIBUTO

CAMPINAS
2023

JULIANA MAIA CARVALHO DOS SANTOS

DIAGNOSING RESERVOIR MODELS USING SIMILARITY INDICATORS WITH 4D SEISMIC DATA: A MULTI-DOMAIN AND MULTI-ATTRIBUTES APPROACH

DIAGNÓSTICO DE MODELOS DE RESERVATÓRIO UTILIZANDO INDICADORES DE SIMILARIDADE COM A SÍSMICA 4D: UMA ABORDAGEM MULTI-DOMÍNIO E MULTI-ATRIBUTO

Thesis presented to the Mechanical Engineering Faculty and Institute of Geosciences of the University of Campinas in partial fulfillment of the requirements for the degree of Doctor of Philosophy in Petroleum Sciences and Engineering, in the area of Reservoirs and Management.

Tese de Doutorado apresentada à Faculdade de Engenharia Mecânica e Instituto de Geociências da Universidade Estadual de Campinas como parte dos requisitos exigidos para obtenção do título de Doutora em Ciências e Engenharia de Petróleo, na área de Reservatórios e Gestão.

Orientador: Prof. Dra. Alessandra Davolio
Coorientador: Prof. Dr. Denis José Schiozer

Este exemplar corresponde à versão final da Tese defendida pela aluna Juliana Maia Carvalho dos Santos e orientada pela Prof. Dra. Alessandra Davolio.

____
Assinatura do Orientador

CAMPINAS

2023

Ficha catalográfica
Universidade Estadual de Campinas
Biblioteca da Área de Engenharia e Arquitetura
Rose Meire da Silva - CRB 8/5974

Sa59d

Santos, Juliana Maia Carvalho dos, 1985-
Diagnosing reservoir models using similarity indicators with 4D seismic data: a multi-domain and multi-attributes approach / Juliana Maia Carvalho dos Santos. – Campinas, SP : [s.n.], 2023.

Orientador: Alessandra Davolio.
Coorientador: Denis José Schiozer.
Tese (doutorado) – Universidade Estadual de Campinas, Faculdade de Engenharia Mecânica.
Em regime multiunidades com: Instituto de Geociências.

1. Método sísmico de reflexão. 2. Reservatórios de petróleo. 3. Reservatórios (Simulação). 4. Simulação computacional. I. Davolio, Alessandra, 1980-. II. Schiozer, Denis José, 1963-. III. Universidade Estadual de Campinas. Faculdade de Engenharia Mecânica. IV. Título.

Informações Complementares

Título em outro idioma: Diagnóstico de modelos de reservatório utilizando indicadores de similaridade com a sísmica 4D: uma abordagem multi-domínio e multi-atributo
Palavras-chave em inglês:
Seismic reflection method
Petroleum reservoirs
Reservoirs (Simulation)
Computational simulation
Área de concentração: Reservatórios e Gestão
Titulação: Doutora em Ciências e Engenharia de Petróleo
Banca examinadora:
Alessandra Davolio [Orientador]
Celio Maschio
Guilherme Daniel Avansi
Luiz Geraldo do Carmo Lucchesi Loures
Marcos Sebastião dos Santos
Data de defesa: 30-01-2023
Programa de Pós-Graduação: Ciências e Engenharia de Petróleo

Identificação e informações acadêmicas do(a) aluno(a)
- ORCID do autor: https://orcid.org/0000-0002-0044-1864
- Currículo Lattes do autor: http://lattes.cnpq.br/2264953019368275

UNIVERSIDADE ESTADUAL DE CAMPINAS

FACULDADE DE ENGENHARIA MECÂNICA

E INSTITUTO DE GEOCIÊNCIAS

PhD THESIS

DIAGNOSING RESERVOIR MODELS USING SIMILARITY INDICATORS WITH 4D SEISMIC DATA: A MULTI-DOMAIN AND MULTI-ATTRIBUTES APPROACH

Author/Autor: Juliana Maia Carvalho dos Santos
Advisor/Orientador: Prof. Dra. Alessandra Davolio
Coorientador: Prof. Dr. Denis José Schiozer

The Examining Committee composed of the members below approved this thesis:
A Banca Examinadora composta pelos membros abaixo aprovou esta tese:

Prof. Dr. Alessandra Davolio, President/Presidente
DE / FEM / UNICAMP

Dr. Celio Maschio
UNISIM / CEPETRO / UNICAMP

Dr. Guilherme Daniel Avansi
UNISIM / CEPETRO / UNICAMP

Dr. Luiz Geraldo do Carmo Lucchesi Loures
Equinor

Dr. Marcos Sebastião dos Santos
Consultant

A Ata da Defesa com as respectivas assinaturas dos membros encontra-se no processo de vida acadêmica do aluno.

Campinas, 30 de Janeiro de 2023

DEDICATION

This thesis is dedicated to my parents, Inês e Pedro.

ACKNOWLEDGEMENTS

As I write this section, I bear in mind this may be my last chance to publicly document my appreciation for all the people that supported me during my studies. I know these words are not enough to demonstrate my gratitude, but I will try my best.

I would like to thank my supervisor Alessandra Davolio for her guidance, setting the high standards, supplying the group with great opportunities and interesting projects. Thanks to my co-supervisor Denis Schiozer, for the opportunity to be part of the group and for always sharing his experience. To my research group, especially Daiane Rosa, you have always been so helpful and answering any questions, any time. Felipe Mesquita, thanks for all the discussions and contributions for mine and our group’s work. Thanks to the administrative and IT support personnel that work at the background, too.

This work was carried out in association with the ongoing project registered under ANP number 20372-9 as ″Desenvolvimento de integração entre simulação de reservatorios e sísmica 4D - Fase 2″ (UNICAMP/Shell Brazil/ANP) funded by Shell Brasil Petroleo Ltda. under the ANP R&D levy as “Compromisso de Investimentos com Pesquisa e Desenvolvimento”. For this reason, I have been very fortunate to be part of a high-level research group, with exceptional data available for my studies. Special thanks to Jorge Lopez for the technical guidance and discussions throughout the project. I also thank CMG, CGG and SLB for the software licenses.

I would like to thank my employer PGS for the support given during the final phase of my PhD, especially my manager Adrian Burke for being understanding and always so supportive.

My family and friends: thanks for understanding my distance during this and several other periods. My grandmas Mã and Vó Loira (in memoriam), you have raised a beautiful family and educated us to work hard. My aunts, you have set the best example of strong, self-dependent women. My parents, I appreciate your effort to providing me with the best education you could. My nephew Lino, I hope you have a good education too, and be a happy boy with a bright future. My nephews Bianca and Lucas and my extended nephews Joaquim and Manoela – aunty loves you and we will play much more once this is done. Filippo, you brought light and more joy to our family. My dear friends – your constant support means the world to me. Jessica, your unconditional friendship is the greatest gift one can have. Fernanda, thanks for always cheering me up no matter what. Elisa, thanks for always listening and replying with the kindest words.

My partner Guilherme, thank you for always being by my side and encouraging me. To the AWOWR support group, you have been the best company and care during the pandemic.

Thank you for the constant support. I appreciate you all.

RESUMO

Na última década, a aquisição de dados sísmicos 4D (S4D) incorporou sistemas de monitoramento permanente onde sensores são instalados no fundo do oceano, coletando dados sísmicos de forma recorrente de acordo com a demanda de monitoramento do projeto. Simultaneamente, os fluxos de trabalho de gerenciamento de reservatórios baseados em modelos evoluíram para incluir incertezas, onde centenas de realizações são consideradas. Processar, interpretar e avaliar todas as informações disponíveis rapidamente é crucial para tomar decisões críticas a tempo. Alguns dos principais passos das abordagens para desenvolver e gerenciar um campo baseadas em modelos dependem de minimizações de erro entre dados modelados e medidos, convencionalmente, através de dados de produção nos poços, e mais recentemente, adaptados para dados S4D. Quantificar estas incertezas é uma tarefa complexa, e estimativas globais para cada realização nem sempre são suficientes para capturar desajustes locais, que podem ser significativos e ocorrer, por exemplo, em uma região importante considerada para a perfuração de poços. O foco deste estudo é, portanto, apresentar um fluxo de trabalho rápido, robusto e com supervisão mínima para medir indicadores de similaridade entre um levantamento monitor sísmico observado e os modelos de simulação de reservatório, considerando-se todas estas complexidades. A metodologia compreende (1) calibrar um modelo petro-elástico; (2) modelagem direta para entendimento de possíveis sinais sísmicos 4D sob vários cenários de produção; (3) adaptação do fluxo de trabalho para lidar com centenas de modelos simulados para medir sua similaridade com o sinal de S4D observado; (4) medidas de erros que combinam estimativas de erros de formato e magnitude das anomalias 4D, com diagnósticos globais e locais (por regiões). O fluxo de trabalho foi aplicado a um reservatório turbidítico ultra profundo localizado no Brasil (denominado campo S), com monitoramento sísmico permanente desde o início de sua produção. A parte inicial do estudo reduziu as incertezas relacionadas à não singularidade na interpretação dos efeitos 4D que ocorrem simultaneamente e mediu seu impacto nas métricas de similaridade entre S4D observada e modelada. Em seguida, o estudo forneceu as principais contribuições da tese, demonstradas em quatro aplicações: (1) rápido diagnóstico de várias iterações de geomodelagem, (2) rápido diagnóstico de iterações de assimilação de dados sísmicos e de poço, (3) avaliação rápida de um novo levantamento monitor sísmico e (4) filtragem de modelos de classificação para estudos posteriores de tomada de decisão. O fluxo de trabalho foi essencial em todo o esquema de gerenciamento do campo S. Para a aplicação (1), sinalizamos, com sucesso, como as anomalias de S4D estavam sendo honradas nos modelos de simulação e quantificamos o impacto da melhora no entendimento das heterogeneidades do reservatório e na introdução de feições interpretadas na S4D na geomodelagem. Para a aplicação (2), quantificamos as melhorias nos modelos de simulação após diversas etapas de assimilação de dados. Para a aplicação (3), avaliamos rapidamente a qualidade dos modelos de simulação existentes com relação a um novo monitor sísmico assim que sua aquisição e processamento foram concluídos, validando a necessidade de recalibrar os modelos de simulação ou não. O fluxo de trabalho ainda foi fundamental para selecionar os melhores modelos, dentre centenas, para o processo de tomada de decisão, na aplicação (4). Por fim, o trabalho apresenta uma comparação entre o diagnóstico realizado em diferentes domínios: os domínios da amplitude sísmica, Impedância-P e saturação, onde discutimos e realizamos recomendações de cada domínio para cada aplicação específica.

Palavras-Chave: monitoramento sísmico; sísmica 4D; assimilação de dados; modelos de simulação; modelos de reservatórios.

ABSTRACT

In the last decade, 4D seismic (4DS) data acquisition has incorporated permanent monitoring systems where sensors are installed at the ocean bottom, collecting seismic data repeatedly according to the project's monitoring demand. Simultaneously, model-based reservoir management workflows evolved to include uncertainties, where hundreds of realizations are considered. Processing, interpreting, and assessing all the information available rapidly is crucial to make critical decisions on time. Some of the main stages of model-based approaches for developing and managing a field rely on error minimizations between modeled and measured data, traditionally from well production data, and hereafter adapted to 4DS data. Quantifying these uncertainties is a complex task, and global error estimates for each realization are not always sufficient to capture local misfits, which can be relevant when they occur, for example, in an important region being considered for well drilling. The focus of this study is, therefore, to present a fast, robust and minimal-supervision workflow to measure similarity indicators between observed seismic monitor and reservoir simulation models, considering all these complexities. The methodology comprises (1) calibrating a petro-elastic model; (2) forward modeling to understand elastic changes under various individual and combined production scenarios; (3) adapting the workflow to handle hundreds of simulated models to measure their similarity with the observed 4DS signal; and (4) error measures that combine 4DS signal format and magnitude evaluations with global and local diagnosis for each model. The workflow was applied to an ultradeep Brazilian turbidite reservoir (named field S) with a permanent seismic monitoring system since the field's production started. The initial part of the study reduced uncertainties related to non-uniqueness in the interpretation of competing 4DS effects and measured their impact at the 4DS similarity metrics. The next step provided the main contributions of the thesis, demonstrated in four applications: (1) feedback on various iterations of geomodeling, (2) feedback on well and seismic data assimilation, (3) quick evaluation of a new seismic monitor, and (4) ranking models for further decision-making studies. The workflow is proven essential in the entire field model-based management outline. For application (1), we successfully flagged which and how the 4DS anomalies were being honored in the simulation models, and it quantified the impact of introducing features interpreted from seismic monitors in the geomodeling and on heterogeneity behavior. For application (2), we quantified simulation model improvements provided by data assimilation.

For application (3), we rapidly evaluated the quality of the existing simulation models as soon as a new seismic monitor acquisition and processing was complete, validating the requirement to recalibrate the simulation models or not. The workflow was crucial to filter best models, out of hundreds, for the decision-making process in application (4). Finally, this work presents a comparison between the diagnosis performed in different domains: the seismic amplitude, P-impedance and saturation domains, where we discuss and make recommendations for each domain in each application.

Key Words: seismic monitoring, 4D seismic; data assimilation; simulation models; reservoir models.

FIGURE LIST

TABLE OF CONTENT

1 INTRODUCTION

4D seismic (4DS) data are critical for understanding reservoirs and have become the standard practice for reservoir monitoring. It provides input to predictive simulation models, contributing to insights regarding compaction, pressure and fluid changes and movement over the production and injection regime of a field. In the last decade, 4DS monitoring broadened from towed streamers to permanent systems where sensors are either installed or deployed on demand at the ocean bottom, collecting seismic data according to the project's monitoring requirements. Although the operational effort to place the receivers on the seafloor and the acquisition costs are higher in this kind of systems, the benefits are threefold: good illumination, high 4DS repeatability and 4DS monitors may be available more frequently. These are all recent demands of the giant Brazilian presalt fields, considering their complex geological settings with deep targets. However, once the 4DS data are acquired, it is necessary to process, interpret and assimilate important dynamic information. These are all time-consuming steps that may prevent operators from making reservoir management decisions on time.

On the reservoir management side, the frameworks under uncertainties, considering hundreds of realizations, add up more data to analyze, process and interpret. Diagnosing such a large number of models can be complex and time-consuming. Most studies on this topic have employed the closed-loop reservoir management concept presented by JANSEN.; BROUWER; DOUMA (2009), which involves the use of various uncertainties in the models related to the reservoir, economical settings, and production systems, in combination with measurements such as well production and 4DS, to continuously update the models. This concept was then detailed by SCHIOZER *et al.* (2019) in twelve steps, where all the main components, such as reservoir characterization, data assimilation, resulting scenario reduction and subsequent decisions, rely on the measurements of errors between modeled and observed data. In this context, the inclusion of 4DS information as observed data to be honored by the simulation models in a timely and practical manner is essential.

This thesis proposes practical and comprehensive frameworks to integrate 4DS into the decision-making process under uncertainties; more specifically, we provide robust and fast measurements of the matching quality between simulation models and 4DS data. We developed a workflow and tested the proposed methodology on a deepwater turbidite field (field S) that has been monitored through an ocean-bottom cable (OBC) seismic system since 2013 with five monitors up to this moment. We begin the work by calibrating a petro-elastic model (PEM) to the data, understanding the observed 4DS anomalies and revealing the competing effects, first in the 1D domain, applying the PEM at the well scale to understand the 4DS signal under various scenarios. Then, in the 3D domain, a few simulation models are used to understand the 4DS signal at the reservoir scale. Last, the workflow is adapted to ensembles of simulated models. The ultimate purpose of the workflow is to diagnose hundreds of models using similarity metrics between observed 4DS and predicted 4DS given by the simulation models.

Figure 1 illustrates the forward and inversion modeling steps and the various domains at which a diagnosis based on data comparisons can be performed. The forward modeling top arrow shows the conversion of the simulation models to the seismic amplitude domain, hereafter focused on the compressional amplitude and referred as the “amplitude domain” for simplicity. The grey double arrow 3 represents a diagnosis based on comparisons between observed and modeled 4DS amplitudes. The goal of this part of the work is to provide a quick data diagnosis as soon as the observed 4DS monitor is made available, which occurs in the amplitude domain.

The red double arrow 2 shows comparisons performed at the P-impedance (IP) domain. This is a very practical domain because it does not require the full forward modeling process and it results in layer properties (rather than interface properties) that can be more easily incorporated in the models. However, running a 4DS inversion may take several months and carries uncertainties: it is an ill-posed problem and depends on seismic data frequency content, which are discussed in detail in ROSA; SCHIOZER; DAVOLIO (2022). This work was developed for available acoustic data, i.e., considering full-stack seismic data and acoustic (P) impedance, but the workflow can be extended to the elastic domain where angle stacks and elastic attributes such as Vp/Vs, Lambda-Rho and Mu-Rho can be evaluated.

The data comparison workflow can be adapted to the saturation/pressure domain, through direct correlations between seismic amplitudes and physical effects, as illustrated by the double green arrow 4. The comparison from the blue arrow 1, on the other hand, is not a focus of this thesis because it requires running petro-elastic inversions, which are costly and time-consuming and therefore not qualified as a fast and robust approach. However, several inversion methods using deep neural networks are recently being developed to overcome this requirement (e.g. CÔRTE *et al.* 2020; MALEKI *et al.*, 2022; XUE *et al.*, 2019) where forward modeled data is used in the training dataset for obtaining inverted saturation changes estimates. Because of the inherent dependency of the PEM and the forward modeling steps, this work did not consider these results for making the comparison from arrow 1.

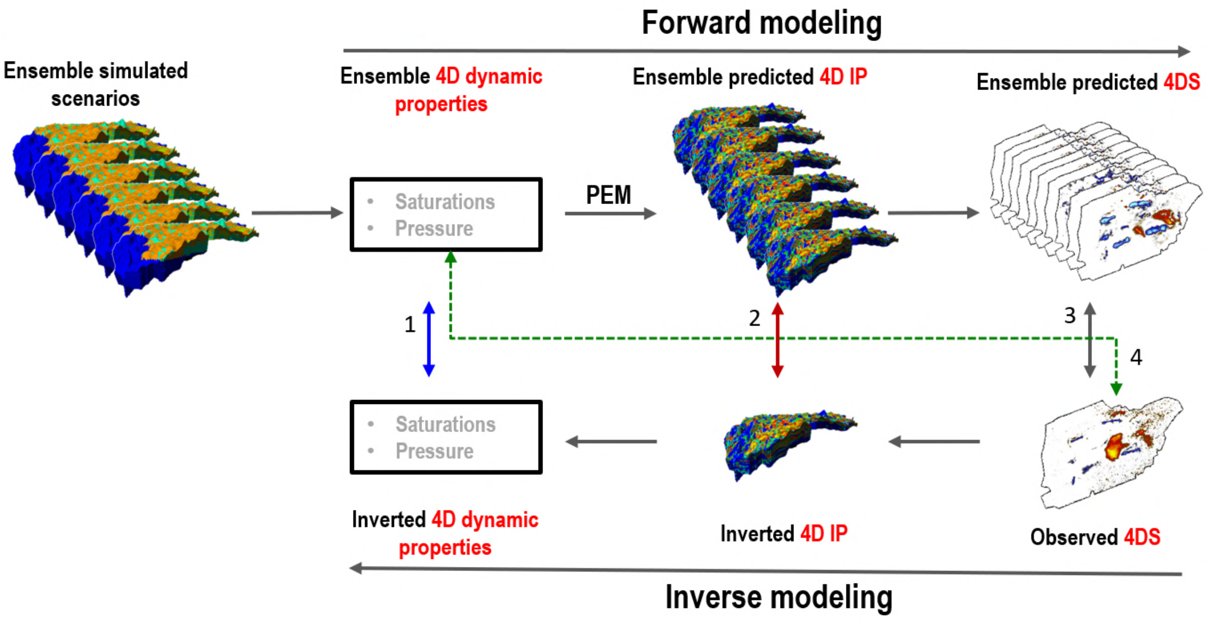

Figure 1 - The various data integration domains (modified from DAVOLIO (2013)) between the 4DS and simulation models. Blue arrow 1, red arrow 2, gray arrow 3, and green arrow 4 represent respectively comparisons made in the saturation/pressure, IP, amplitude and cross-domains.

Having established the methodology in several domains, the final contribution of this thesis is a comparison of the various diagnoses obtained for each domain. The working domain remains an open research question to which the thesis aims to propose recommendations. The expected outcome of this work is an advanced integration of 4DS data to reservoir simulation through a quick diagnosis of ensembles of simulation models, such as geomodeling and data assimilation quality assessment.

1.1 Motivation

The recent development of more complex fields, with very deep and complex geological structures, demand higher quality data, with good illumination and exceptional 4DS repeatability so that errors in reflectivity related to noise and processing of 4DS data are not incorrectly introduced in the workflows. The deepwater presalt reservoirs from the most recent Brazilian discoveries in the Campos and Santos basins, for example, are difficult to image not only due to their depths but also due to their tectonic complexity and multiple heterogeneities inherent to their depositional systems. In addition, a small 4DS signal may be expected in these types of reservoirs due to the rock’s response to physical changes (as low as 1.5% changes in IP reported in CRUZ *et al.*), and the importance of excellent 4DS data increases. The oil price volatility demands exploration and monitoring schemes to be developed at a lower cost and more efficiently; therefore, making accurate predictions that add more value to the project is essential. Besides, efficient exploration and production activities are crucial for supporting low-carbon targets.

The evolution of monitoring technologies has resulted in better imaging resolution, increased repeatability, high-quality and frequent 4DS signals. However, the value of this advancement highly depends on assimilating data on time to make decisions. Integrating 4DS in the reservoir management workflows for these decisions remains a challenging task, and there are limited studies on how to practically include these observations in the models.

A proper framework provides a quick diagnosis in a data-massive environment, where we can extract knowledge and insights from a large amount of data while addressing challenges with meaningful scenario reduction. Understanding this leads to more confidence in the decision-making process (reliable models), which is essential knowledge to guarantee that the 4DS are incorporated safely and rapidly with the simulation models.

1.2 Objectives

The general objective of this work is to propose a methodology to quickly diagnose simulation models according to their 4DS representation.

The specific objectives are as follows:

- To use seismic forward modeling to explore the interdependence between the sensitivity of the 4D seismic signal, the rock physics model and each simulated model;
- To develop a workflow for seismic forward modeling hundreds of simulation models;
- To develop similarity metrics to diagnose models based on the shape and magnitude of observed 4D anomalies; and
- To compare the different domains where to calculate the similarity metrics at.

1.3 Thesis structure

The thesis consists of eight chapters and three appendices, the last two in scientific papers format. In this subsection, we summarize these chapters and the articles.

Chapter 2 presents a literature review, with a discussion of the most current research concerning the 4DS and simulation model integration topic.

Chapter 3 proposes a methodology for 4DS and simulation integration under uncertainties and details the main steps developed and used.

Chapter 4 defines the geological setting and the dataset where the methodology is applied. This chapter provides details about the 4DS acquisition, field development, and main 4DS signals present in the data.

Chapter 5 presents the results obtained using the methodology proposed in several reservoir management steps. It also presents some important insights regarding the need to make region-by-region evaluations and complementarity between the shape and magnitude similarity metrics. The results are presented in three different sections, one for each analysis domain: the seismic amplitude, the IP and the saturation domain. This section also presents comparisons of diagnosis performed in different domains.

Chapter 6 shows the conclusions and recommendations.

Chapter 7 lists future work suggestions.

Although the application case comprehends 5 seismic monitors, we show examples on monitors 3 (that contains larger and stronger anomalies) and 5 (last monitor available to demonstrate model forecast applicability). The Appendix A, however, shows the results of the diagnosis performed in all different seismic monitors, with different levels of noise and repeatability. The Appendix B shows the well rates of the diagnosed models on a selected set, and their match with actual production data.

This thesis utilizes previously published material under the two appendix papers:

Appendix C is a conference paper presented at the American (ATCE): SANTOS, J. M. C.; SCHIOZER, D. J.; DAVOLIO, A. Multi attribute approach for quantifying competing time lapse effects and implications for similarity indicators in data assimilation. **Proceedings - SPE Annual Technical Conference and Exhibition**, [*s. l.*],.], v. 2020-Octob, 2020. Available at https://doi.org/10.2118/201426-MS. This paper details the first part of the general methodology of the thesis: calibrating a PEM and seismic forward modeling to understand the main 4D effects that occur in the reservoir. The outcome of this paper is an increased knowledge of the competing 4D effects and how they may affect the 4DS similarity indicators.

Appendix D is an article published at the Journal of Petroleum Science and Engineering: SANTOS, J. M. C.; ROSA, D. R. L.; SCHIOZER, D. J.; DAVOLIO, A. Fast diagnosis of reservoir simulation models based on 4D seismic similarity indicators, available at https://doi.org/10.1016/j.petrol.2021.110083. This paper presents the second part of the general thesis methodology that proposes similarity metrics between the observed 4DS signals and predicted 4DS signals. This work is the outcome of a workflow that handles hundreds of models and diagnoses them according to their shape and magnitude similarity with 4DS, region by region, with several interesting example discussions.

Appendix E shows the permissions to include the published work in this thesis.

2 LITERATURE REVIEW

This chapter explains how previous works handled the 4DS integration into reservoir management processes and introduces the key concepts used for the thesis.

2.1 The model-based reservoir development and management concept

JANSEN *et al.* (2005) presented the use of production measurements and other data, such as 4DS, to continuously update reservoir models, inspired by measurement and control theory from the process industry and data assimilation techniques from meteorology and oceanography. They discussed the closed loop concept, where initially only static information is available, such as 3D seismic and well tests. As production starts, the models can be history-matched so that their simulated dynamic behavior can reproduce the actual behavior while considering their uncertainties. The history-matching concept then evolved to the data assimilation process, where the focus is to find models with higher probability to make good predictions.

The main stages of the decision analysis process in model-based reservoir development and management based on the closed-loop concept rely on error measures between modeled and measured data. SCHIOZER *et al.* (2019) expanded the concept and presented a comprehensive methodology establishing 12 steps for model updating and production optimization under uncertainty, where building and calibrating models, data assimilation, selecting representative models, and risk assessment are steps supported by the errors measured from well production data and are increasingly being supplemented from 4DS.

2.2 4D data integration and its different levels

Finding a practical framework for integrating 4DS into decision analysis remains a major challenge in reservoir management. The amount of data to analyze and include in the procedures increases substantially as the project evolves and as new technologies, such as permanent seismic monitoring systems, are implemented. Another challenge in these workflows is the analysts’ subjectivity to evaluate, interpret and incorporate 4DS in the simulation models. This may vary according to experience, background, and availability of complementary data such as production rates and geological information.

Fundamentally, we need a quick way to diagnose if the generated simulation model ensembles are minimally matching dynamic data responses before they are inserted in the loops.

Assessing 4DS monitors as soon as they are made available for guiding critical decisions is therefore essential.

As an interdisciplinary task, reservoir simulation and 4DS data integration are complex, and data assimilation workflows have the potential to quantitatively incorporate these data into simulation models. An example of a powerful tool to perform data assimilation is the Ensemble Smoother with Multiple Data Assimilation (ES-MDA) proposed by EMERICK; REYNOLD (2013), which aims to modify uncertain properties from the models to match with observations (well and 4DS data), as they become available (OLIVER; ALFONZO, 2018). However, one assumption for a successful application of this method is to have a good prior ensemble with well-mapped prior uncertainties. A framework to diagnose the prior ensembles becomes an important step to be performed before running data assimilation, and 4DS integration in this prior generation phase is limited to manual and qualitative. The quantitative 4DS integration is mostly limited to the data assimilation process, where 4DS is used as a component of the objective function.

In many cases, integrating different domains requires conversions such as seismic forward modeling and/or seismic inversions. The best domains in which to incorporate the seismic at remain uncertain; however, the most common domain is seismic impedance (e.g. GOSSELIN *et al.* (2003), ROGGERO *et al.* (2007), EMERICK (2016), LORENTZEN *et al.* (2018), SILVA NETO; DAVOLIO; SCHIOZER (2021)), which requires running a petro-elastic modeling for the simulation model and the execution of a 4DS inversion to convert observed seismic amplitudes into impedance changes.

The amplitude domain has the advantage of being immediately available once the seismic campaign acquisition and processing finishes and avoids including time-consuming seismic inversions into the workflows. On the other hand, the amplitude is an interface property, while the impedance is a layer property, which can be more practical to integrate into the reservoir models. In addition, to convert reservoir properties into amplitudes, it is necessary to perform full forward modeling. AMINI (2014) established a structured workflow for the simulation-to-seismic (sim2seis) domain conversion process and demonstrated it with real case applications using a single model. LEEUWENBURGH; BROUWER; TRANI (2011) and SOUZA *et al.* (2018) selected the full petro-elastic and forward modeling approach to consider most characteristics of the seismic method, such as the influence from overburden, underburden, wavelet, and, most importantly, the combinations of dynamic effects. Their works were tested in 3D synthetic model ensembles, where the first used 4DS in their history matching workflow, and the second used 4DS similarity checks to rank and select optimum models.

LUO *et al.* (2016) adopted amplitude vs. angle (AVA) domain comparisons in a 2D case, where the AVA attributes were computed from the reflection coefficients calculated by a petro-elastic model, introducing a wavelet-based sparse representation to further assimilate 4DS into their ensemble of models. The authors then successfully extended their work to a 3D case in LUO *et al.* (2018). SOARES *et al.* (2020) also adopted the AVA domain and selected the main features of the 4DS attributes for history matching an ensemble of reservoir models using a dictionary learning method.

Meanwhile, several authors successfully used direct cross-domain comparisons between responses from simulator and different seismic attributes, avoiding the additional petro-elastic and forward modeling steps. OBIDEGWU; CHASSAGNE; MACBETH (2015) applied threshold values to provide binary maps of observed amplitude and simulated gas saturation 4D difference maps, where the threshold values separated the presence and absence of anomalies. They then used the Hamming distance to calculate the misfit between the binary 4DS map and the binary saturation difference map. TRANI *et al.* (2017) used k-means clustering to binarize maps of time-lapse relative changes in P-wave velocity and maps of simulated dynamic properties. They then measured the misfit between the maps according to distances to the 4D anomaly front. DAVOLIO; SCHIOZER (2018) also worked with k-means clustered amplitude and saturation maps, applying the misfit function proposed by TILLIER; DA VEIGA; DERFOUL (2013). ZHANG; LEEUWENBURGH (2017) adapted the Hausdorff distance to measure dissimilarity at fluid fronts.

Some authors also proposed interesting data-driven solutions to provide cross-domain misfits between 4DS and simulation models, such as the momenta tree method (SORIANO-VARGAS *et al.*, 2020) and deep learning using models trained by 4D experts using convolutional neural networks (ROLLMANN, 2020), which have been tested in synthetic cases and look promising on real cases.

As illustrated, the reported applications vary from deterministic to ensemble-based, where hundreds of simulation models can be converted into the elastic domain, facilitated by petro-elastic models coupled to the simulator (e.g. GOSSELIN *et al.* (2003) and SKJERVHEIM *et al.* (2007)). Few ensemble-based works have been reported with the full forward modeling (e.g. FAHIMUDDIN; AANONSEN; SKJERVHEIM (2010) and SOUZA *et al.* (2018)), which, although realistic, were synthetic cases. LIU; GRANA (2020) also report ensemble-based use of synthetic 4DS in the amplitude domain but sparsely represented to reduce data dimensionality.

2.3 The similarity metrics

For well data, it is common to use mean square errors measured between simulated and observed data series, such as the NQDS (Normalized Quadratic Deviation with Sign) used in several works (e.g. AVANSI; MASCHIO; SCHIOZER (2016); ALMEIDA *et al.* (2018); FORMENTIN *et al*. (2019)), to obtain a complete view of all objective functions in a concise plot. Regarding 4DS data, this comparison is not straightforward, as we need to compare maps (or 3D volumes) and not time series. Furthermore, these misfit measures may be affected by biases toward outliers or may generate global error values that mask significant local misfits, which emphasize the importance of evaluating the reservoir region by region.

The methods published thus far for providing these misfits are successful but cannot address all aspects of the problem at the same time. The most typically used least-square-based errors do not account for shape errors between both responses; likewise, shape-based methods disregard problems related to magnitude 4DS signal misfits. (CHASSAGNE; ARANHA, 2020) conducted a very comprehensive review of magnitude-based measures in the data assimilation context and discussed that the least-squares metric is as able to capture important information as other more sophisticated metrics.

Regarding the shape similarity metrics, several authors proposed approaches to represent the 4DS information by clustering their attributes into binary images and measuring errors considering pixel-by-pixel misfits. TILLIER; DA VEIGA; DERFOUL (2013), for example, effectively proposed a formulation with binary image analysis based on the Hausdorff distance between observed and simulated IP changes and demonstrated it with a deterministic history matching case. The binary approaches presented thus far have two main limitations: the 4DS attributes are compared to one single dynamic property change, and they only account for the existence and absence of a 4D signal, disregarding the polarity of the signal. In addition, assembling the shape of the 4DS attributes into clusters may be challenging because they rely either on threshold values for 4DS signal definition, filtering (e.g. DERFOUL *et al.*, 2013), or clustering algorithms, and their execution is not always straightforward, especially in a 4D project. The threshold approach may be impractical because cutoff values may have to be reviewed depending on the seismic monitor. Seismic monitors should ideally be acquired and processed in the same way, but in practice, this is not always possible. Repeatability and noise level may vary among vintages depending on the seismic acquisition conditions (e.g. different sources or acquisition parameters, seismic interference, and sea conditions). Moreover, the intensity of the 4D signal changes throughout the monitor surveys. Additionally, if hundreds of simulation models need to be compared with 4DS data, a fixed cutoff will probably not be enough to cluster the data, as different threshold values may be required across models. Regarding the clustering algorithms, the most applied in previous works is the k-means. However, its convergence assumes spherical clusters and equal probabilities for each cluster. Therefore, it may also not work for all kinds of seismic attribute value distributions because centroids can be dragged by outliers not assuring the definition of the expected number of clusters.

2.4 The Gaussian mixture models (GMM)

The GMM is an unsupervised learning technique, where data are unlabeled and the program fits Gaussians for the input data. The expectation-maximization (E-M) algorithm then estimates and optimizes the models based on their maximum likelihood that a certain observation belongs to each Gaussian.

The GMM labels input data considering posterior probability distributions. The models are fitted to data according to given or random initial conditions: the mean μ, the variance σ^2 and, optionally, the mixing proportions π for each cluster k. The program estimates the probability $p(x)$ that a sample occurs at a certain location x of the component densities p_k, given their parametric initial conditions.

$$\boldsymbol{p(x) = \sum_{k=1}^{K} \pi_k \, p_k(x|\mu_{k,} \sigma 2_k)} \qquad \textbf{(1)}$$

where

$$0 < \pi_k < 1 \qquad \text{and} \qquad \sum_{k=1}^{K} \pi_k = 1 \qquad \textbf{(2)}$$

The EM algorithm then fits the GMMs to the data, optimizing a maximum likelihood function. The E-step provides soft clustering; that is, it computes the posterior probability E that a component i belongs to cluster k.

$$E_{i,k} = \frac{p(x=x_i|\mu=\mu_i, \sigma 2=\sigma 2_i)}{\sum_{i=1}^{k} p(x=x_i|\mu=\mu_i, \sigma 2=\sigma 2_i)} \qquad \textbf{(3)}$$

The M-step estimates the distribution of each cluster based on the latest assignment.

$$\mu_{i,k}\, \sigma_{i,k} = \frac{\sum_{i=1}^{k} E_{i,k} x_i}{\sum_{i=1}^{k} E_{i,k}} \qquad \textbf{(4)}$$

Limited seismic applications are reported for the technique: clustering earthquake signals (SEYDOUX *et al.*, 2020), as inversion prior models (ASTIC; HEAGY; OLDENBURG, 2021; FJELDSTAD; AVSETH; OMRE, 2021), seismic facies analysis (WALLET; HARDISTY, 2019) and data assimilation schemes (DOVERA; DELLA ROSSA, 2011). Regarding specific 4DS applications, ZHAO *et al.* (2007) presented a modification of the EM algorithm, applied to find GMM’s that group and measure errors in 4DS and well production data. For the particular application of clustering 4DS anomalies and their integration with data assimilation (history-matching), AMINI *et al.* (2019) compared several objective functions to history match three models, including errors from binarized maps using GMM, initialized using manually defined 4DS amplitude thresholds. With this parameterization they concluded, however, that the GMM was not able to capture differences between the models. No other 4DS clustering implementations using GMM were found reported in previous works.

3 METHODOLOGY

The methodology of this work follows the diagram presented in Figure 2, in which the steps are numbered and described in the next subsections. The top boxes and the gray steps are the essential elements of a reservoir management workflow using 4DS (AMINI, 2014). Essentially, the workflow automatically selects each model from the simulation ensemble, extracts its dynamic information from a desired date to compare against the observed 4DS response. As discussed in the chapter 1, this comparison can be achieved in many different levels or domains, which in Figure 2 are indicated by the red, green and gray arrows, respectively representing the IP, saturation and amplitude domains.

The simulation models and their data assimilation results used for this thesis were generated in separate works performed and described by MASCHIO *et al.* (2021) and ROSA; SCHIOZER; DAVOLIO (2022), where the last authors also derived the 4DS inversion steps from the red boxes.

The blue steps are the specific methodologies which were developed as contributions of the thesis. The specific methodology supplies a region-by-region diagnosis according to the shape and magnitude similarity between simulation models and 4DS. It can be an iterative workflow depending on the application; for example, when problematic regions are flagged in the diagnosis step, the geological or simulation models can be revised, updated and re-diagnosed until an optimal error level is reached. The model update process, however, is not part of this work, although the outcome of the diagnosis we provide is a detailed guide for the updates. In addition, when new seismic monitors are acquired, new modeled 4DS response at the new dates can be obtained from the simulation ensemble to perform a new diagnosis. Moreover, when new knowledge on the reservoir generates updates on the simulation model, the workflow can be re-run, and the simulation ensemble can be re-evaluated.

The numbering of the boxes in Figure 2 follows the next sections’ numbering, where each step is explained in detail.

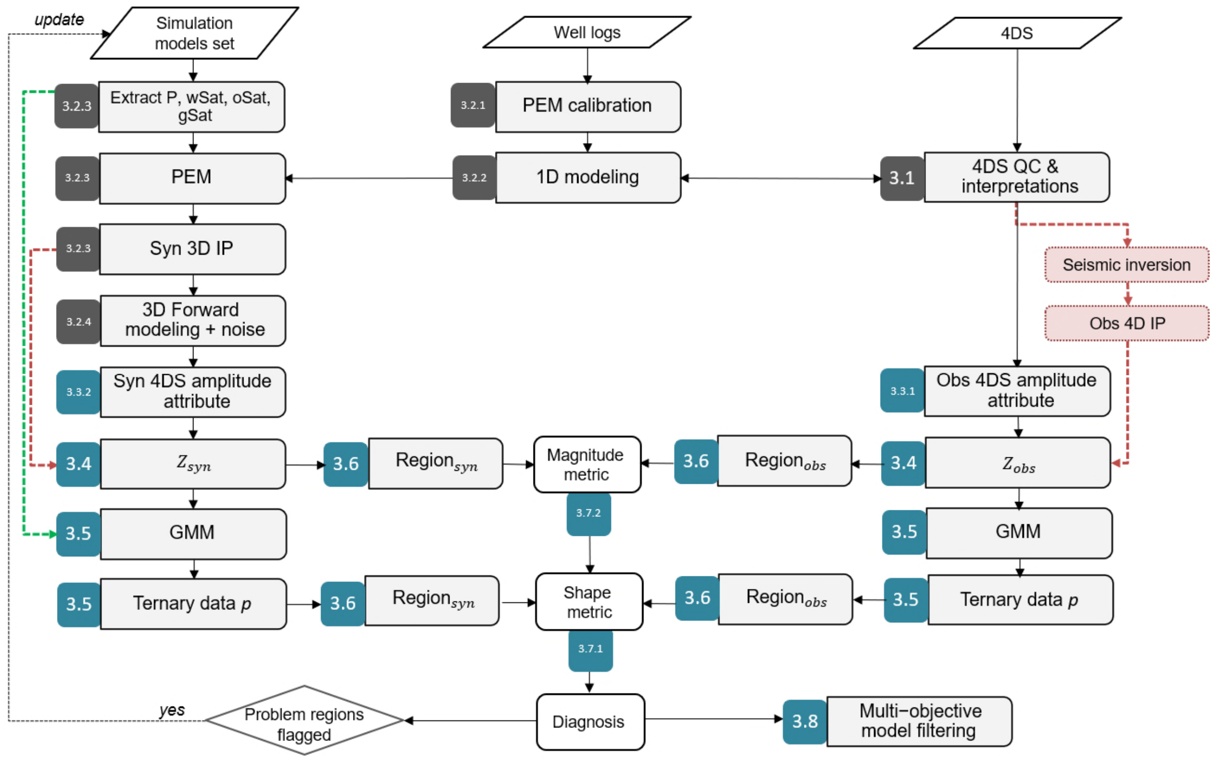

Figure 2 - Diagram describing the general (gray) and the specific (blue) methodology developed in this thesis.

3.1 Data quality analysis and initial interpretations

This step consists of understanding the observed 4DS signal and assessing its overall quality, according to the post-stack 4DS standard quality checks detailed in (STAMMEIJER; HATCHELL, 2014), such as:

- Understanding the polarity of time-lapse changes;
- Extracting seismic attributes that depict the 4DS signal and 4DS repeatability and processing issues; and
- Testing windows to map the seismic attributes.

To assess the 4DS repeatability quality, we used the NRMS metric calculated between the survey pairs, determined by KRAGH; CHRISTIE (2002) as:

$$NRMS = \frac{RMS(B - M)}{\frac{1}{2}(RMS(B) + RMS(M))} \tag{5}$$

3.2 4DS response modeling

3.2.1 Calibrating a petro-elastic model (PEM)

The PEM is a set of equations that describe the link between reservoir rock and fluid properties and elastic properties. Many theoretical and empirical methods are available for defining these relations.

3.2.2 1D modeling

The PEM calibrated in the previous step is used to generate elastic attributes in the 1D domain using available sonic and density logs. The 1D analysis aims to understand elastic changes under various individual and combined production scenarios, e.g., variations in pore pressure, gas and water saturation.

3.2.3 3D modeling using a simulation model

The aim of the 3D analysis is to evaluate elastic changes at the 3D scale using saturation, effective porosity and pore pressure values from a simulation model. The purpose is to understand the 4D changes under scenario interactions using reservoir conditions for simulated production scenarios. This step extracts the dynamic and static properties from each simulation model and calculates IP values (using the PEM defined in step 3.2.1) for each date as close as possible to the 4D seismic monitor acquisition date.

In this step, the IP and the saturation/pressure values for each model can be used for the IP and saturation/pressure domain comparisons (red and green arrows respectively in Figure 2 towards step 3.4). For the IP domain analysis, the IP ratio between monitor and baseline are used. For the saturation/pressure domain, we propose to use saturation/pressure differences between the monitor and the baseline.

3.2.4 Amplitude domain – forward modeling and noise

This step is performed in Petrel, where IP values from the previous steps are imported and re-grided from the simulation model grid to a seismic cartesian grid. A constant overburden and underburden are introduced, based on average measures from sonic and density logs, to establish reliable interfaces between the reservoir's top and base. For each seismic cell, the zero-offset reflectivity is calculated using the normal incidence equation, and the reflectivity values are convolved with a wavelet that mimics the frequency content from the observed data at the reservoir level. The result is one 3D seismic amplitude volume for each date.

Synthetic seismic data must mimic the observed data to make fair comparisons. The synthetic noise is generated and added to the synthetic amplitude to reproduce the seismic noise related to each vintage acquisition and to repeatability between vintages. The random noise is defined according to the signal-to-noise ratio observed in the actual seismic data, and it may be vintage-dependent.

3.3 Extracting 4DS attributes in the amplitude domain

3.3.1 Observed 4DS attribute

As the intention is to fast-track results to guide critical decisions, we generate $dRMS$ amplitude maps, extracted in key reservoir intervals from each 3D seismic vintage, described in STAMMEIJER; HATCHELL (2014) for an acoustically soft reservoir as follows:

$$dRMS_{obs} = RMS_{obs\,base} - RMS_{obs\,mon} \tag{6}$$

where the $RMS_{obs\,base}$ and $RMS_{obs\,mon}$ are the RMS values obtained from the observed 3D baseline and monitor surveys respectively, extracted at the reservoir interval of interest. The workflow can be adapted to any 4DS attribute.

3.3.2 Synthetic 4DS attribute

The steps described in sections 3.2.3 and 3.2.4 are carried out for all the models within the ensemble. The RMS_{syn} maps are extracted from each synthetic volume generated, at the same window interval as step 3.3.1, and the $dRMS_{syn}$ between a baseline and a monitor is obtained as follows:

$$dRMS_{syn} = RMS_{syn\,base} - RMS_{syn\,mon} \tag{7}$$

The result is, therefore, one $dRMS_{syn}$ map for each model within the ensemble.

3.4 4DS attribute standardization

The maps are then standardized to avoid distance-based problems in the error metrics and in the clustering algorithm and to compare units in similar scales.

The observed 4DS standardized Z_{obs} attribute value is given by:

$$Z_{obs} = \frac{4DS_{obs} - \mu_{obs}}{\sigma_{obs}} \tag{8}$$

where μ_{obs} and σ_{obs} are the mean and standard deviation of the $4DS_{obs}$ map, respectively.

Similarly, the synthetic 4DS standardized Z_{syn} attribute is described by:

$$Z_{syn} = \frac{4DS_{syn} - \mu_{syn}}{\sigma_{syn}} \qquad \textbf{(9)}$$

where μ_{syn} and σ_{syn} are the mean and standard deviation of the $4DS_{syn}$ map, respectively.

This step is performed both for the amplitude (black arrows towards step 3.4 in Figure 2), using the $dRMS$ as the $4DS$ term, and for the IP domain (red arrows towards step 3.4 in Figure 2), using the IP ratio between a monitor and a baseline as the $4DS$ term, which can be adapted to any 4DS attribute.

3.5 Run GMM and EM to cluster observed and predicted maps

For a 4DS attribute in any domain, we consider three clusters: (k_1) representing the negative polarity (softening) anomalies, (k_2) the zeroes (absence of 4D anomalies) and (k_3) the hardening anomalies, as schematized respectively by the red, green and blue cluster colors from the Gaussian distributions in Figure 3 b and e and the ternary maps in Figure 3 c and f. We assume that the repeatability noise level is low enough to be fitted in the same Gaussian k_2, and the random noise inherently has a normal distribution around zero.

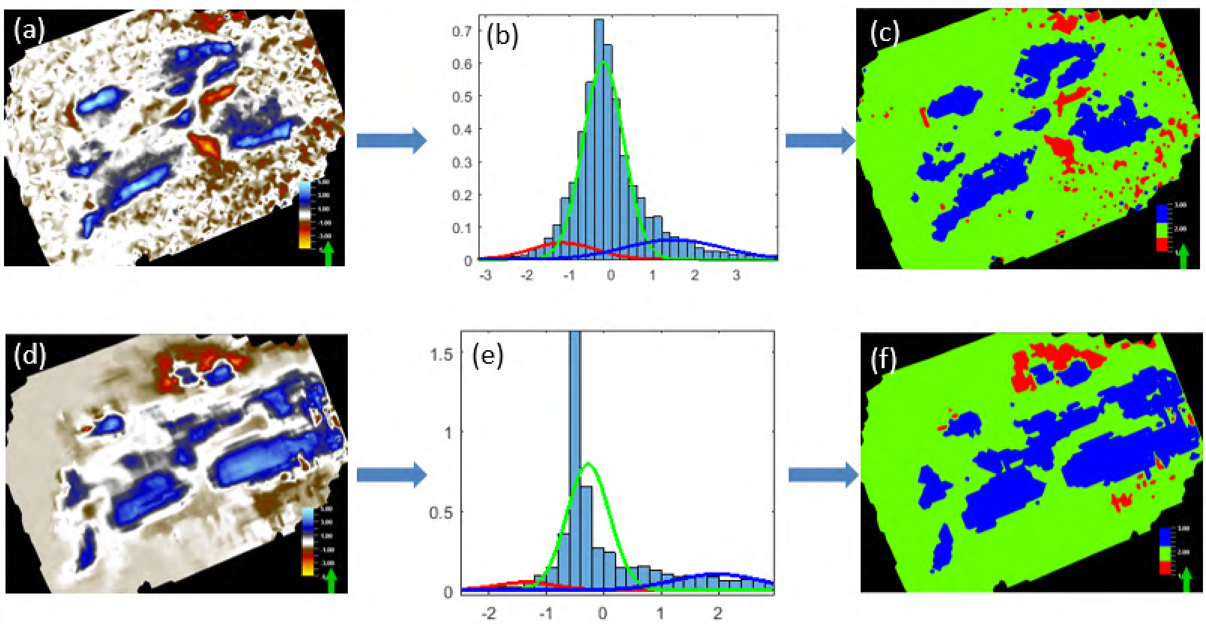

Figure 3 - Illustrative scheme of GMM clusterization and ternary comparison. (a) $4DS_{obs}$ and (d) $4DS_{syn}$ maps, respectively converted to ternary maps displaying observed pixels *o* (c) and predicted pixels *p* (f). The histograms from (b) and I show the clusters' gaussian distributions: red for k_1, green for k_2 and blue for k_3.

We use a value initialization for each cluster's mean and variance, providing the same initial conditions for each observed and synthetic seismic attribute map based on statistics of the normalized observed 4DS attribute Z_{obs} at the desired date.

The green arrow from Figure 2 shows that the saturation domain data may also skip from step 3.2.3 to step 3.5, where saturation difference maps are clustered and directly compared with amplitude maps. The three clusters in this case are: (k_1) representing a decrease in saturation between a monitor and a baseline, (k_2) the zeroes (absence of saturation difference) and (k_3) the increase in saturation.

3.6 Region segmentation

This step must be carried out in conjunction with the observed 4DS interpretation, where each region accounts for the presence and absence of a 4D signal, and proximity with well locations where a certain cluster of 4DS signal is expected.

3.7 Comparison of observed vs. synthetic seismic data

3.7.1 Shape evaluation: entire reservoir and region error calculation

The observed and predicted ternary maps are compared through a shape metric *SM* calculated by the Hamming distance between the observed pixel *o* and predicted pixel *p* from the ternary maps schematized in Figure 3 c and f, divided by n_r, i.e., the size *n* of each region *r* (or number of pixels inside each region), given by:

$$SM[o, p] = \frac{\sum_{i=0}^{i} \delta_i(o, p)}{n_r} \tag{10}$$

where

$$\delta_i(o, p) = \{ 1\ if\ o_i \neq p_i \quad 0\ if\ o_i = p_i \tag{11}$$

3.7.2 Magnitude evaluation: entire reservoir and region error calculation

The magnitude metric *MM* is given by the mean square error between Z_{obs} and Z_{syn}.

$$MM[Z_{obs}, Z_{syn}] = \frac{\sum_{i=1}^{nr} (Z_{obs} - Z_{syn})^2}{n_r} \tag{12}$$

3.8 Multi-objective filtering

We propose a multi-objective model filtering that creates separate high error model (outliers) lists on each metric *SM* and *MM*, and on each region *r*.

$$Out_{SM,r} = \mu_{SM,r} + a\ \sigma_{SM,r} \quad \textbf{(13)}$$

$$Out_{MM,r} = \mu_{MM,r} + a\ \sigma_{MM,r} \quad \textbf{(14)}$$

where μ and σ are respectively the mean and standard deviation of the error metrics *SM* and *MM* within the models' ensemble. The coefficient a may be project-dependent and may be based on the number of models to be filtered out.

The outlier lists can be used to discard models that do not honor 4DS observations. We propose them to be used simultaneously, that is, for a model to be considered good, it must not be contained in any outlier list from any region and any metric.

4 APPLICATION

4.1 Field S background

4.1.1 Geological information

Field S is a deep water turbidite located in the Campos Basin at the Brazilian east margin. The tectonic evolution of the Campos Basin has three main stages: (1) the pre-rift, characterized by South Atlantic crustal expansion; (2) the rift from the South Atlantic opening, establishing normal fault valleys and volcanism; and (3) the post-rift. The main petroleum system plays were established syn- and post-rift. The reservoir sandstones from field S are interpreted to belong to the Carapebus Formation, which is a marine regressive mega-sequence predominantly composed of successions of fluvial-deltaic systems, with deltaic fans, siliciclastic platforms and deep-water turbidites (WINTER; JAHNERT; FRANÇA, 2007).

The reservoir is located 1200 m below the mudline, and the water depth is between 1600 and 1700 m. The reservoir thickness is between 15 and 45 m, stratigraphically trapped, and pinching out to the northeast. To the west, the reservoir is structurally contained by 3 major faults oriented NE-SW. Figure 4 illustrates the mentioned structural characteristics interpreted from the 3D seismic dataset, where the bright hot colors represent the soft IP reservoir sandstones. The sandstone quality is good, with an average porosity of 25%, which may be contaminated with thin (sub-seismic resolution) shale intercalations. The seismic data resolution at the reservoir level, considering an average dominant frequency of 18 Hz, is estimated by ROSA; SCHIOZER; DAVOLIO (2022) to be approximately 30 m.

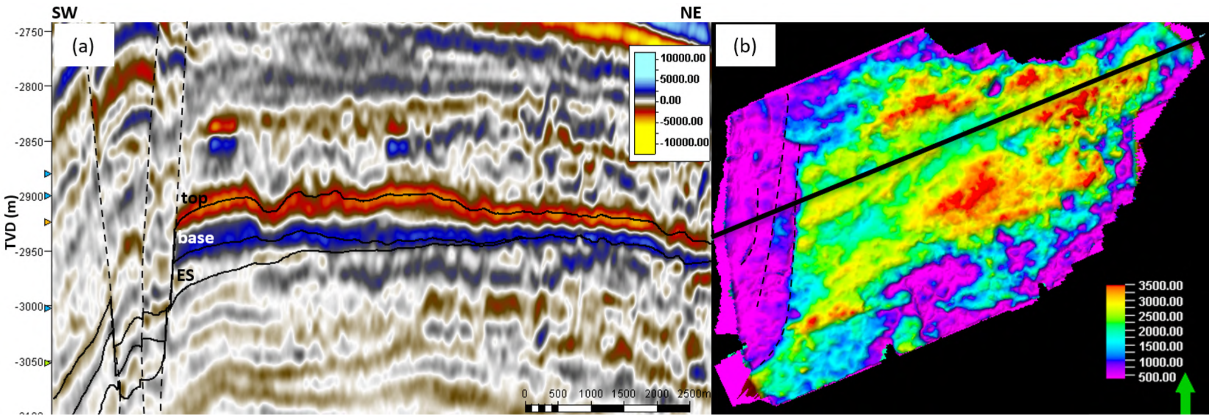

Figure 4 - (a) Vertical cross-section of the baseline seismic data. The black lines show the reservoir´s top, base and extra-sand interpretations, and the dashed lines are the major faults. (b) RMS amplitude map between the top and base horizons. The black line shows the cross-section location.

4.1.2 Field development and its seismic monitoring system

The field was initially developed with 7 horizontal producer wells (well trajectories in red from Figure 5) and 4 horizontal water injector wells (well trajectories in blue from Figure 5). The baseline survey was acquired shortly after production started. Since then, several seismic monitors were acquired: monitor 1 (7 months after the baseline, 4 months after water injection started), monitor 2 (9 months after monitor 1), monitor 3 (almost one year after monitor 2), monitor 4 (18 months after monitor 3) and monitor 5 (almost 3 years after monitor 4).

The initial reservoir pressure was approximately 0.7 MPa above the bubble point. The field's seismic monitoring uses 100 km of ocean-bottom cables (OBC) in 14 lines spaced 400 m crossline and 4 component sensors spaced 100 m inline covering the entire reservoir and extending over the 3 aforementioned major faults that limit the reservoir to the west (BUKSH *et al.*, 2015), represented by the black lines in Figure 5. The seismic source is a single source with 3 arrays shooting in a 50 x 50 m grid. The receiver array is permanently connected to a recording system located on the FPSO that supports production activities in the field. This equipment arrangement facilitates the need to mobilize only a shooting vessel to record subsequent monitor seismic surveys for field surveillance (CHEN *et al.*, 2015). Figure 5 shows the layout of the system over an amplitude map of the field.

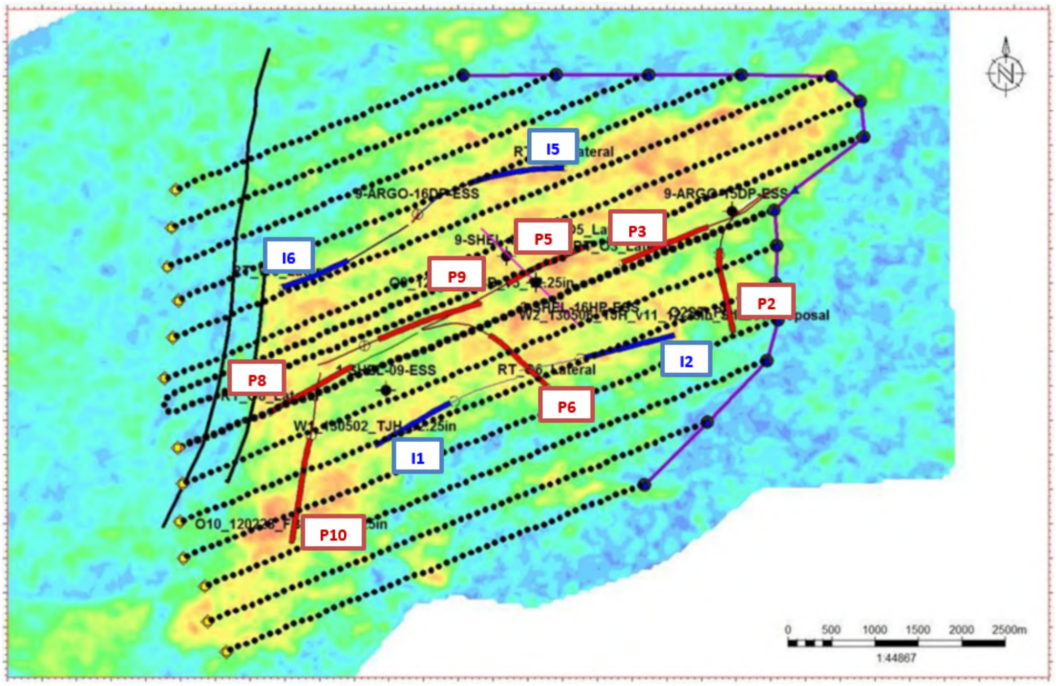

Figure 5 - Ocean bottom location of sensors and wells drilled up to 2015, overlaid with a seismic amplitude map (adapted from BUKSH *et al.* (2015)).

Monitors 1, 2 and 3 followed the same acquisition parameters and processing sequence. Monitor 4 is a “snapshot” survey, which was acquired as an opportunity throughout a neighbor survey being acquired with streamers. Because of that, this monitor has a different geometry, shooting direction and coverage than the other surveys. CHANG *et al.* (2019), however, argue that although noisier, the 4D signal is still clearly visible in the snapshot.

Monitor 5 has a different amplitude recovery compared to the other surveys because of a different processing sequence. The baseline was therefore co-processed again to be compared against this monitor.

4.2 Simulation models

The model ensembles and their data assimilation were generated by other specialist members detailed in ROSA; SCHIOZER; DAVOLIO (2022) of the research group and were not developed as part of this thesis. The simulation models have a total of 87,768 cells in a 73 x 38 x 32 grid, with approximate sizes of 150 m x 150 m x 4 m in the i, j and k directions, respectively, simulated using the black-oil numerical reservoir simulator IMEX (CMG). The models were generated under 53 scalar uncertainties, such as the initial water-oil contact depth, multipliers that define the absolute permeability in the vertical direction, connate water saturation, fluid relative permeability, irreducible oil saturation, and rock compressibility, with 200 geostatistical realizations of static properties, such as horizontal permeability, porosity, net-to-gross ratio and facies. The full details on the uncertainty parameters and ranges are detailed in MASCHIO *et al.* (2021). These uncertainties were combined using the discrete Latin hypercube with geostatistical realizations method (SCHIOZER; AVANSI; SANTOS, 2017), resulting in 200 different models.

Various iterations of geomodeling were performed and were constantly updated, according to new information acquisition or as the field understanding increased. All the sets were diagnosed using the proposed workflow. The following sets were selected to illustrate this thesis, all comprising 200 reservoir simulation models with different levels of reservoir characterization:

- <u>Set S3D</u>: Geomodeling iteration 1, using 3D seismic data (from the baseline survey) as co-variable, without introducing features interpreted from the 4DS.
- <u>Set S4D</u>: Geomodeling iteration 2, adding features interpreted from 4DS introduced (up to monitor 3), as described in MALEKI *et al.* (2021), and improved knowledge on the reservoir behavior and its heterogeneities.

- Set S4D_post_W: Set S4D after data assimilation using the ES-MDA method, including well history data only, up to year 5). The models were updated in four iterations, using BHP data for all wells and oil rates for producers and total liquid and water rates for producers and injectors, respectively, as boundary conditions.
- Set S4D_post_WS: Set S4D after data assimilation using the ES-MDA method, including well and 4DS data. The well data used are the same as Set S4D_post_W, and the 4DS map is the ratio of inverted acoustic impedances between the monitor 3 and the baseline, extracted between the reservoir top and base.

The seismic inversion and data assimilation used in the last two sets were generated and discussed in detail in ROSA; SCHIOZER; DAVOLIO (2021).

4.3 Petro-elastic modeling (PEM)

The seismic signal is a combination of the responses of the rock, frame, minerals and fluid and its ability to combine these responses (EMERICK *et al.*, 2007). Several authors proposed ways to describe the effective bulk and shear moduli of the rock's granular assembly, with the Hertz–Mindlin contact theory being one of the most used to model unconsolidated sandstones (MAVKO; MUKERJI; DVORKIN, 2009). Given the geological characteristics described in the previous section, the Hertz–Mindlin contact model is used to estimate the dry bulk and shear modulus (K_{dry} and μ_{dry}) of the rock at critical porosity and their dependency on effective pressure P_{eff} (MAVKO; MUKERJI; DVORKIN, 1998).

$$K_{HM} = \sqrt[3]{\frac{C^2(1-\emptyset_c)^2\mu_0^2}{18\pi^2(1-\nu_s)^2}P_{eff}} \quad \textbf{(15)}$$

$$\mu_{HM} = \frac{5-4\nu_s}{5(2-\nu_s)}\sqrt[3]{\frac{3C^2(1-\emptyset_c)^2\mu_0^2}{2\pi^2(1-\nu_s)^2}P_{eff}} \quad \textbf{(16)}$$

where C is the coordination number (number of contacts per sphere), ν_s is Poisson's ratio, and μ_0 is the grain shear modulus.

The lower Hashin-Shtrikman bound can then be used to calculate K_{dry} and μ_{dry} at porosities between 0 and the critical $\emptyset_c$ according to:

$$K_{dry} = \left[\frac{\frac{\emptyset}{\emptyset_c}}{K_{HM} + \frac{4}{3}\mu_{HM}} + \frac{\frac{1-\emptyset}{\emptyset_c}}{K_s + \frac{4}{3}\mu_{HM}} \right]^{-1} - \frac{4}{3}\mu_{HM} \quad \textbf{(17)}$$

$$\mu_{dry} = \left[\frac{\frac{\emptyset}{\emptyset_c}}{\mu_{HM} + \frac{\mu_{HM}}{6}Z} + \frac{\frac{1-\emptyset}{\emptyset_c}}{\mu_s + \frac{\mu_{HM}}{6}Z} \right]^{-1} - \frac{\mu_{HM}}{6}Z \quad \textbf{(18)}$$

$$Z = (9K_{HM} + 8\mu_{HM}) \quad \textbf{(19)}$$

Batzle & Wang (BATZLE; WANG, 1992) equations are used to define the bulk modulus for each fluid (K_o, K_g, K_w for oil, gas and water, respectively), and Wood's equation is used to define the bulk modulus for the fluid mixture (K_{fl}), according to:

$$\frac{1}{K_{fl}} = \frac{S_w}{K_w} + \frac{S_o}{K_o} + \frac{S_g}{K_g} \quad \textbf{(20)}$$

Finally, Gassmann's equations (GASSMANN, 1951) are used to state the final saturated bulk modulus (K_{sat}) using the saturation estimates from the well logs.

$$\frac{K_{sat}}{K_0 - K_{sat}} = \frac{K_{dry}}{K_0 - K_{dry}} + \frac{K_{fl}}{\emptyset(K_0 - K_{fl})}, \ \mu_{sat} = \mu_{dry} \text{ and } \rho_{sat} = \rho_{dry} + \Phi\,\rho_{fl} \quad \textbf{(21)}$$

where K_0 is the bulk modulus of the minerals that form the rock frame. The resulting K_{sat} is then used to predict the elastic parameters of the saturated rock according to:

$$V_P = \sqrt{\frac{\frac{K_{sat}+4}{3\mu}}{\rho}} \text{ and } I_P = \rho V_P \quad \textbf{(22)}$$

$$V_S = \sqrt{\frac{\mu}{\rho}} \text{ and } I_S = \rho V_S \quad \textbf{(23)}$$

We use the templates defined by (ØDEGAARD; AVSETH, 2004), adjusted using the RockSI software – the modeled data by the PEM's are compared against the measured logs: P-wave velocity (V_P), S-wave velocity (V_S) and density (ρ) to verify the well fit quality. After calibration of the above parameters at the well, the equations can be applied to each cell of the reservoir model, given their saturations and porosity.

5 RESULTS AND DISCUSSION

5.1 Data quality analysis

BUKSH *et al.* (2015) reported acquisition noise related to the in-field rig activities during the baseline survey and seismic interference from another survey during the first monitor. Pressure Inverted Echo Sounder (PIES) instruments provide water velocity and tidal depth data for deep-water statics (WANG *et al.*, 2015), which are also reported to have added insights into overburden integrity and geomechanics (EBAID *et al.*, 2017).

Regarding the seismic data processing, the seismic data used for this work are noise and multiple-attenuated, 4D processed, and time-shift corrected. A QC prior to the interpretations, however, showed residual time-shifts near gas-related 4DS anomalies and residual overburden energy at the 4DS differences between monitors 1, 2 and 3 and the baseline. These residual time-shifts had a minor effect on the interpretations between the reservoir top and base of the reservoir but were acknowledged and flagged throughout the work. Nevertheless, the 4DS repeatability quality is excellent, with NRMS values measured in the overburden of up to 5% with patchy areas up to 10% on ultrafast-track products (seismic volumes obtained using a faster processing sequence), providing confidence that these results can be used for influencing early field life management decisions (BUKSH *et al.*, 2015). Figure 6 shows the NRMS maps for all the vintages, highlighting a lower repeatability region in the northeast up to monitor 3 (Figure 6 a to c). This is the region where the reservoir pinches out (where tuning effects may occur) and has a slightly higher noise level. Therefore, the observed 4D signal interpretation confidence is lower than that of the other regions. Monitor 4 (Figure 6 d) has lower repeatability, as expected, due to the different acquisition parameters (different sail line acquisition azimuth, which imprints are visible in the stripes from Figure 6 d), and monitor 5 (Figure 6 e) has the best repeatability, where the improvement in NRMS values is clear across the entire survey with the new processing sequence.

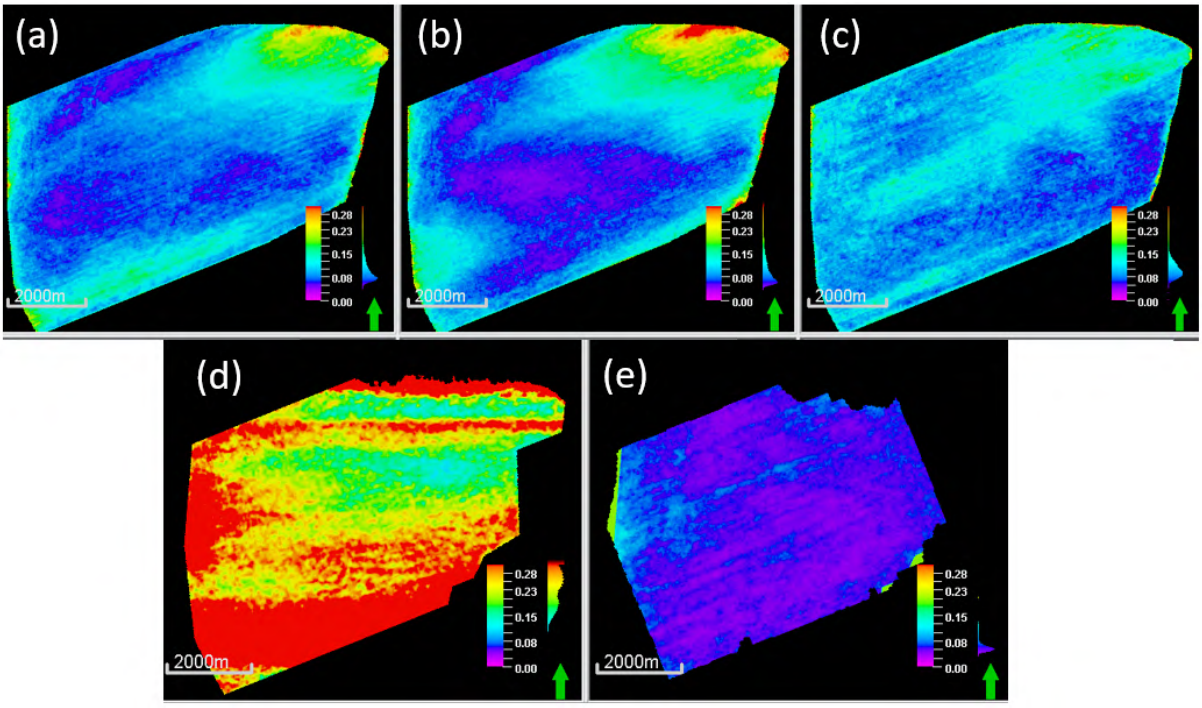

Figure 6 - NRMS maps calculated at the overburden for monitors 1 (a), 2 (b), 3 (c), 4 (d), and 5 (e) vs. baseline.

5.2 Initial data interpretations

Figure 7 shows the 4D $dRMS_{obs}$ map between the baseline and all monitors considering the reservoir zone (from top to base), illustrating the evolution of the 4DS anomalies. As the reservoir is thin (average 25 m), with a soft (through) reflection at the top and a peak at the bottom, $dRMS_{obs}$ maps between the top and base of the reservoir are considered appropriate to capture these anomalies. The main observed 4DS anomalies are hardenings (increase in IP) related to water injection (injected water replacing oil), formation water from the aquifer replacing oil (e.g. near P8 and P10), and softening (decrease in IP) related to gas going out of solution.

Strong 4D signals related to gas going out of solution are observed in two regions: near producer wells P5 and P6 and near producer wells P2 and P3. Pressure effects are not expected to be significant due to the pressure maintenance being supported by water injection; however, at monitor 4, re-pressurization caused some of the gas signal near wells P5 and P6 to attenuate. MALEKI *et al.* (2021) present more detailed interpretations.

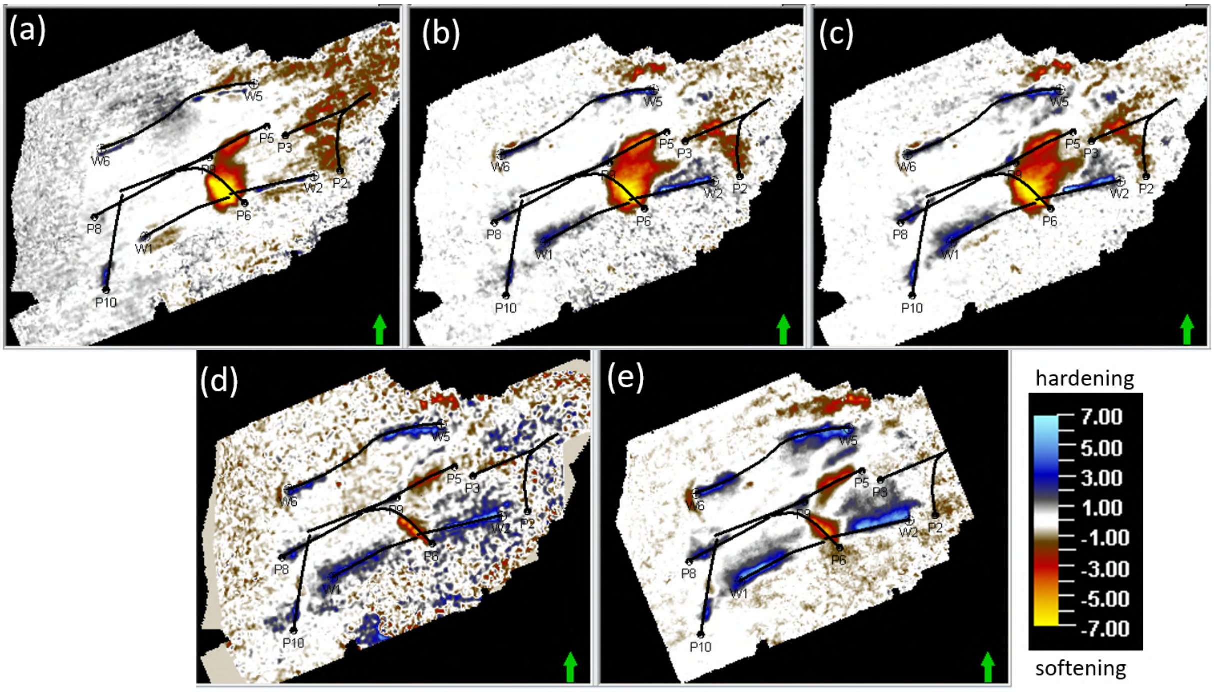

Figure 7 - $dRMS_{obs}$ (baseline against monitors, measured between the reservoir's top and base) showing the 4DS signal evolution: monitor 1 (a), 2 (b), 3 (c), 4 (d), and 5 (e). Note the different signal-to-noise ratios in (d) due to its different acquisition configuration.

5.3 Petro-elastic modeling (PEM)

Figure 8 shows a comparison of the predicted *Vp*, *Vs* and *ρ* (colored lines) with the measured sonic and density logs (black lines) using the predictions from Hertz–Mindlin with coordination numbers 6 and 9 (red and green, respectively). The figures demonstrate that all the models predict the density very well. The models also predict *Vp* and *Vs* fairly well, except for the zones with abrupt changes in lithology, as highlighted by the blue arrows (Figure 8 d). These are interpreted as high-velocity cemented sandstones. The Hertz–Mindlin PEM with coordination number 9 was selected for use in this work because of its better fit with *Vp* (and IP). Table 1 summarizes the other parameters used for the PEM.

Table 1 - Main parameters used for the PEM.

Parameter	Quartz	Clay
K_0 (GPa)	36.6	25
G_0 (GPa)	45	9
ρ (g/cm^3)	2.65	2.55

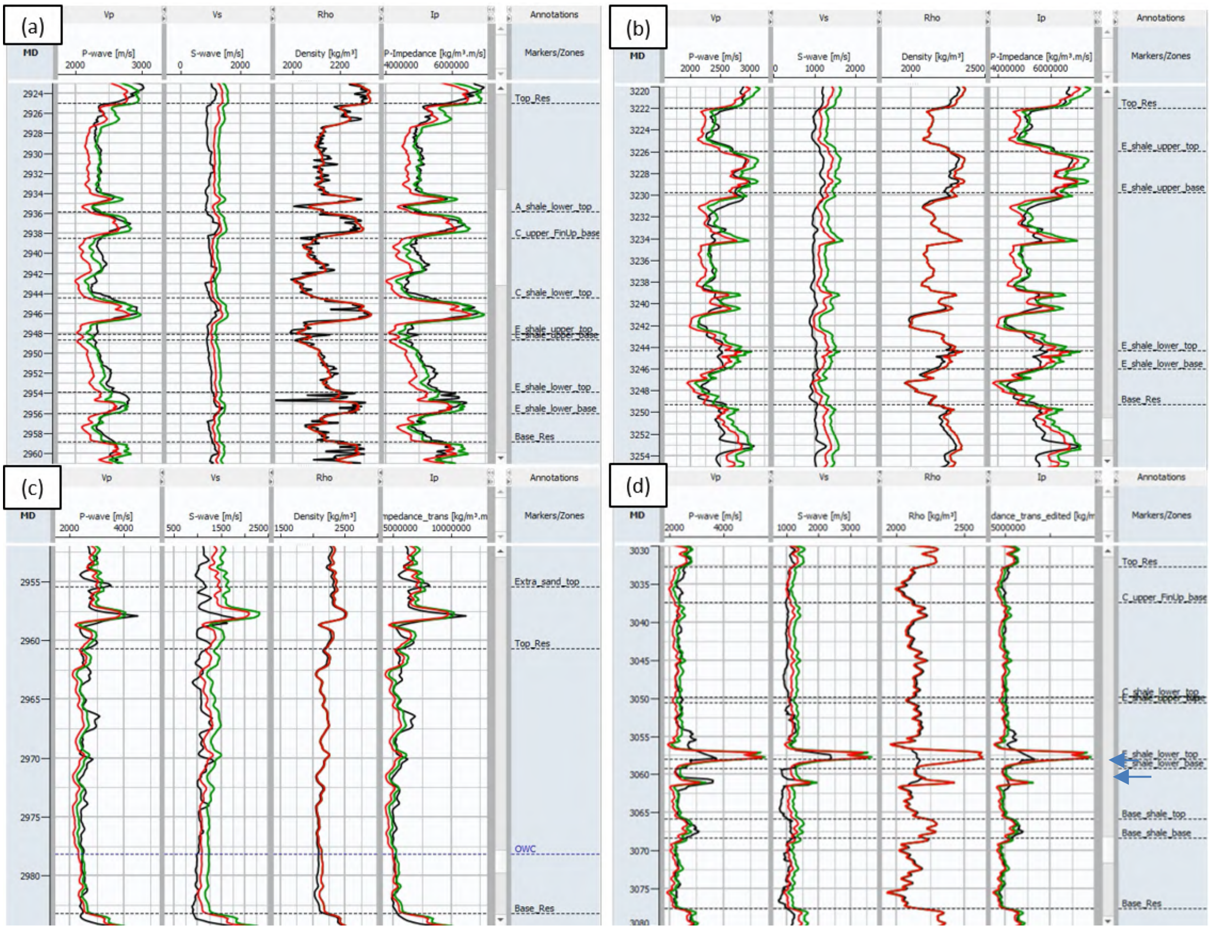

Figure 8 - Fit quality between measured (black) and modeled Vp, Vs, density and P-impedance (IP) logs for wells A1 (a), A2 (b), A3 (c) and A4 (d). The red and green curves are modeled with coordination numbers 6 and 9, respectively. The dashed black lines are the main petrophysical interpretations received from Shell.

5.4 Seismic response modeling

5.4.1 1D modeling to understand the 4D effects

The set of equations defined in the previous step is then applied to various hypothetical production scenarios in the 1D domain (well location) to understand the sensitivity of acoustic impedance changes to each of them. These, according to the initial observations from sections 4.1 and 4.2, are:

- low salinity water injection replacing oil;
- formation water replacing oil;
- gas going out of solution (initial pressure in the S field was just above bubble point and is expected to drop as production starts); and
- pore pressure increases and/or drop.

The 1D modeling illustrated in Figure 9 a and b shows the two main effects that occur throughout the production of the S field: water saturation changes from 20% (connate water saturation) to 87% (100% - 13% of residual oil) and gas saturation variations from 0% to 40%, (considering a critical gas saturation of 40%). Figure 9 a shows that an increase from 20 to 87% in water saturation (formation water replacing oil) causes an 8% increase in IP. Figure 9 b shows that a 2% increase in gas saturation represents a decrease of 6.2% in IP. This is a known effect that occurs because the gas is more compressible, where K_g dominates the resulting K_{fl} (see equation (20)).

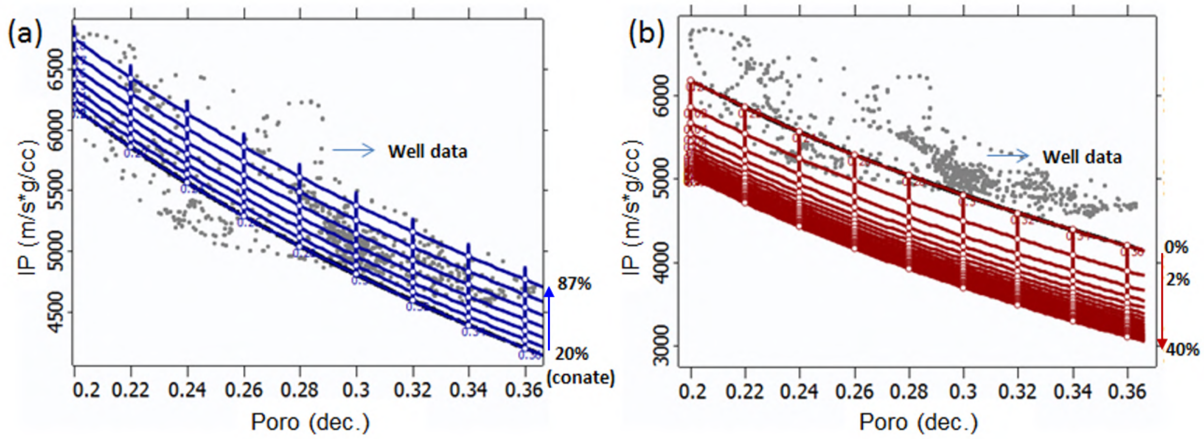

Figure 9 - 1D modeling of (a) water saturation increase and (b) gas saturation increase. No free gas is present at this well A1; therefore, the well data are calibrated to (a).

Figure 10 shows the effect of salinity decrease as a result of injected water replacing formation water (180,000 ppm to 34,000 ppm). The salinity change causes an IP decrease of 3.5%.

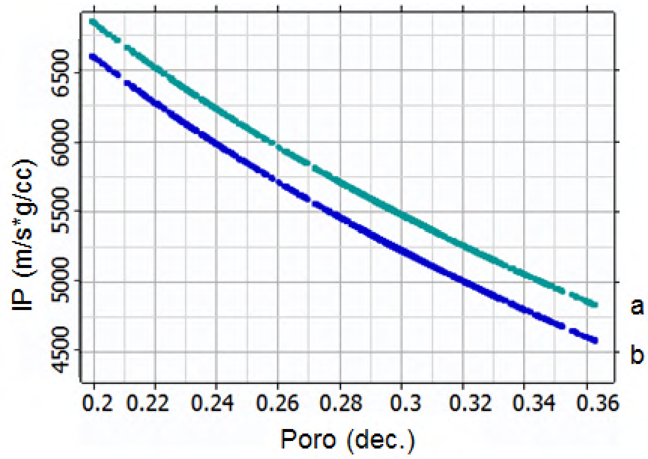

Figure 10 - 1D modeling of the salinity effect: formation water (a) being replaced by injected sea water (b). The water saturation values are kept constant.

Pressure effects are not significant for this field application, as no major pressure variations are observed (up to a 3 MPa difference). The modeling from Figure 11 shows that less than 1.6% in IP change occurs when increasing the pore pressure from 30 to 33 MPa (a to c) and 2% when decreasing to 27 MPa.

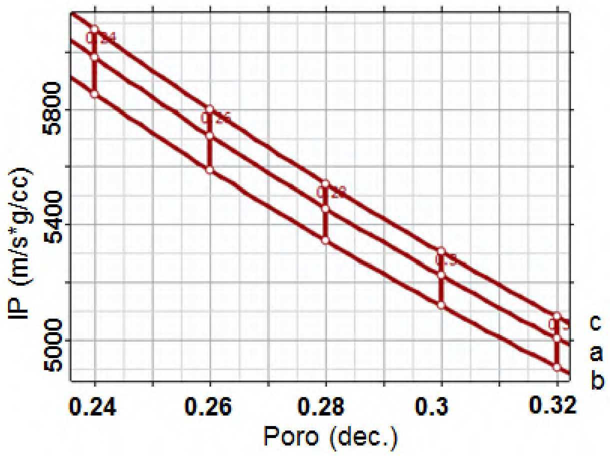

Figure 11 - 1D modeling of the pressure effect (a) 30 MPa, (b) 27 MPa and (c) 33 MPa.

The previous production scenarios are then combined to understand how their interaction affects the elastic sensitivity. A scenario where only water saturation effects occur (e.g., aquifer water invading oil zone, scenario s1 to s2 from Figure 12 a), a 12 to 16% IP increase is observed (hardening effect). However, according to salinity measurements and tracers, injected sea water with lower salinity than the formation water decreases the hardening effect to 8 to 10% in IP change (scenario s1 to s3 compared to scenario s1 to s2 from Figure 12 a). This suggests that the salinity effect, although unremarkable when considered individually as shown in the decoupled modeling, may be significant when associated with other effects, such as the water saturation increase. Additionally, combining these effects with gas going out of solution as a result of depletion below the bubble point, the polarity of the 4D signal reverses (from scenarios s1 to s4 from Figure 12 a), and a 10% increase in gas saturation softens the IP by 15% (scenarios s1 to s5). The synthetic amplitude traces from Figure 12 d, e and f show the different 4D signal polarities depending on the combination of effects. These modeled observations agree with the 4D response caused by saturation, salinity and pressure changes in the field discussed in section 5.2.

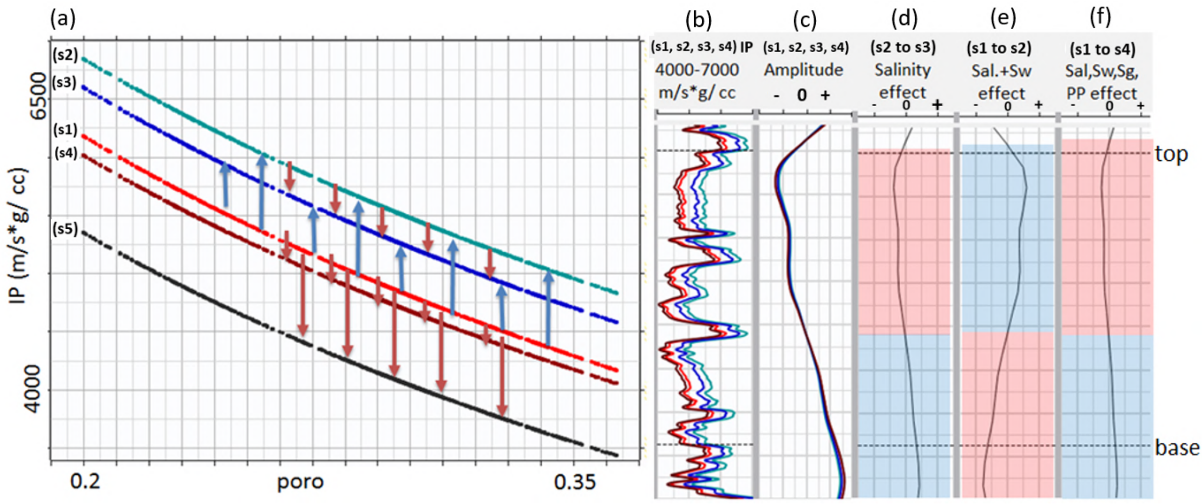

Figure 12 - 1D modeling (appraisal well A1) of the 4D predicted effects. (a): (s1) initial scenario, log saturated with oil and 20% formation connate water (salinity of 180000 ppm); (s2) fully saturated with formation water; (s3) fully saturated with injected sea water (salinity of 34000 ppm); (s4) saturated with formation water +2% increase in gas saturation and 2 MPa pore pressure decrease; and (s5) saturated with formation water +10% increase in gas saturation and 2 MPa pore pressure decrease. (b): modeled IP for s1, s2, s3 and s4. (c) Modeled synthetic traces s1, s2, s3 and s4. (d), (e) and (f) show the synthetic 4D amplitude differences (boosted 10 times in relation to c) resulting from each of the changes of scenarios: s2 to s3, s1 to s2 and s1 to s4.

5.4.2 Generating synthetic seismic data from a simulation model

After understanding the elastic changes in the 1D domain, the simulation model is forward modeled using the described PEM. This step uses MATLAB codes to extract the dynamic and static properties from each simulation model and to calculate IP values for each date as close as possible to the 4D seismic monitor acquisition date. For each seismic vintage, a 3D seismic volume is generated. An automatic Petrel workflow is setup to run the forward modeling for each seismic vintage up to the desired 4DS attribute.

Figure 13 a shows a vertical section of the modeled 4DS difference between monitor 3 and the baseline for one selected simulation model. Figure 13 b is the modeled 4DS difference at the same location with the noise added to each seismic vintage, which is roughly similar to the noise from the observed 4D section seen in Figure 13 c. We add Gaussian random noise to each trace sample to match the observed noise level. The signal-to-noise ratio is defined using root mean square (RMS) estimates from the observed 3D baseline seismic signal and noise. The synthetic seismic data show a good correlation with observed data in terms of frequency content, polarity and the main 4D physical effects, where the main differences between modeled and observed 4DS are due to insufficient simulation model calibration (example from simulation model set S3D).

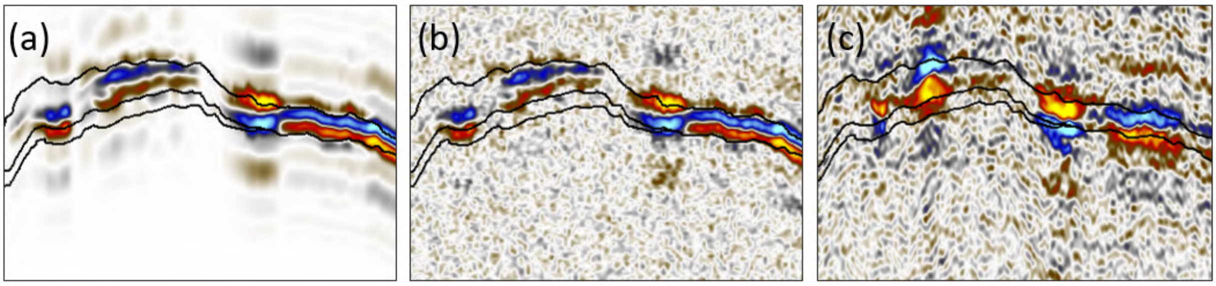

Figure 13 - 4D difference vertical seismic section examples: (a) synthetic, (b) synthetic with random spectrally shaped noise added, (c) observed.

5.5 Attribute maps and region separation

The 4D attribute map can be manually divided into well regions. Each regions' boundaries are defined to contain the observed 4D anomalies forms, which in this application case occur close to the wells. The polygons are then used to divide all the observed and synthetic 4DS attribute maps. The black dashed lines from Figure 14 show the region segmentation (region names in green) over the $dRMS_{obs}$ map between monitor 3 and baseline.

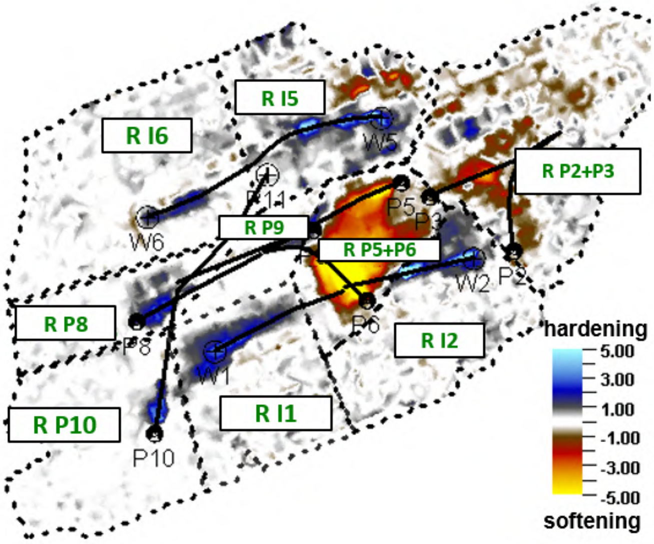

Figure 14 - $dRMS_{obs}$ extracted between reservoir top and base - monitor 3 vs. baseline. The black dashed lines are the region separation, defined according to the 4D signal shape.

5.6 Automatic comparison metrics

The field S exhibits different 4D anomalies in terms of polarity, magnitude, and shapes, and so the predicted 4DS from the sets of simulation models. The next sub-sections show the 4D maps and their anomalies clustering results obtained from different domains.

5.6.1 Feature/shape extraction in the amplitude domain

Table 2 shows the cluster initialization values for the 4D maps in the amplitude domain. The μ_{k1}, and μ_{k3} are, respectively, the minimum and maximum values of Z_{obs}. This was done to initialize the positive, zero and negative anomaly clusters apart from each other, but using statistics automatically extracted from the observed maps so that the procedure is as less dependent on manually set thresholds as possible. The cluster k_2 is initialized with a small variance (0.001) because its distribution is not expected to deviate considerably from the initialized mean 0. The other clusters have slightly larger variance (0.05) initializations.

Table 2 - Value initialization for each cluster k (amplitude and IP domain).

Cluster	μ	$\sigma 2_{obs}$
k_1	$\min(Z_{obs})$	0.05
k_2	0	0.001
k_3	$\max(Z_{obs})$	0.05

Figure 15 shows three examples of the resulting ternary maps using the proposed method (GMM) and two other conventional clustering methods (threshold and k-means). The histograms show the fitted mixture models, k-means centroid and the threshold values overlaid (Figure 15 e, j and o). The GMM method works as expected, clustering the softening anomalies, zeroes, and hardening anomalies within clusters 1, 2 and 3, respectively, even in the presence of noise, which had dubious interpretations. It also picks detailed 4D features such as the fluid front indicated by the arrows from Figure 15 i, resulting from the injected water pushing oil. The examples also suggest that threshold values are not the same across surveys, in this case, due to noise content (dashed lines in Figure 15 e, j and o). The k-means optimization method, using minimization of Euclidean distances, may push the centroids too far from initialization values and result in an empty cluster, as seen in Figure 15 m. The GMM is, therefore, a good compromise between clustering noise and picking the important 4D features. The APPENDIX A shows the clustered maps applied in all monitors, to demonstrate the clustering works for different noise levels, including the repeatability noise present in monitor 4.

Figure 16 shows the GMM clustering performance on $dRMS$ maps predicted for five random simulation models (extracted between monitor 5 and baseline), from which we can observe that the GMM successfully captured the three clusters of data in different dynamic settings. This indicates that the methodology addresses the complexity of generating clusters for very different models with various 4D amplitude ranges.

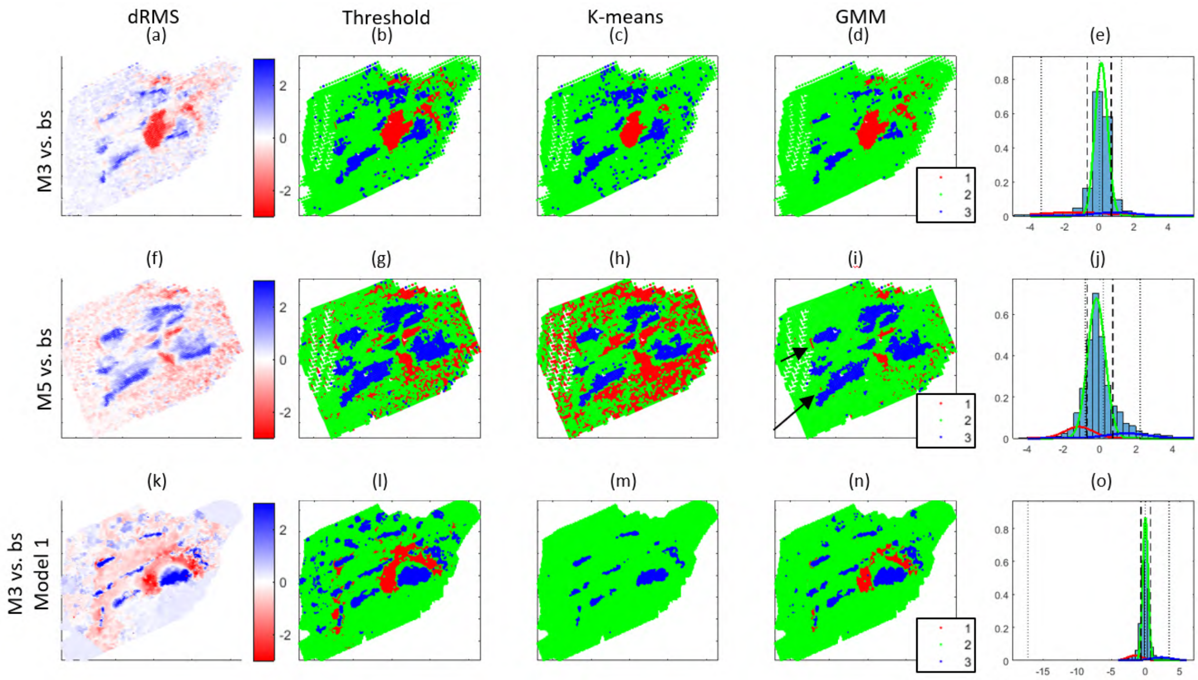

Figure 15 - $dRMS$ maps ternarized using threshold, k-means and GMM, and their corresponding histograms. (a) to (e) for observed monitor 3 vs. baseline, (f) to (j) for observed monitor 5 vs. baseline and (k) to (o) for the synthetic 4DS resulted from forward modeling of model 1 considering monitor 3 and baseline times. The histograms show the Gaussian model mixture distributions (continuous lines), the k-means centroids (dotted line) and the threshold values (dashed line) overlaid at the $dRMS$ value distributions.

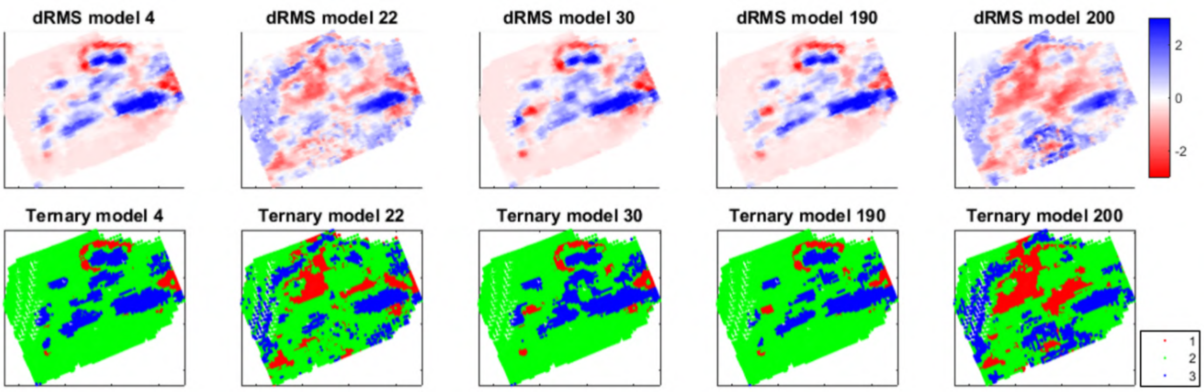

Figure 16 - $dRMS_{syn}$ maps between monitor 5 and baseline for 5 random models (top) and their corresponding ternary maps (bottom).

5.6.2 Feature/shape extraction in the IP domain

The diagnosis application in the IP domain follows the same methodology as in the amplitude domain, however, there are challenges inherent to the 4D inversion and the IP maps may not exhibit the same kind of information as the 4D amplitude attributes. For example, the observed 4D IP may be contaminated with sidelobe effects present in the amplitude data and not resolved in the 4D seismic inversion. These sidelobes are the energy with opposite polarity that occur around the main signal lobe, typically caused by the absence of low frequencies in the seismic data. The challenge is that modeled IP does not contain sidelobe effects (the IP is calculated at each cell from the model using the PEM equations). Therefore, the comparison is affected, where false mismatches may occur due to not comparing the primary observed lobes with the modeled IP. Note that this is not an issue when the comparison is performed in the amplitude domain, as the sidelobes are modeled in the forward seismic modeling.

Although the main 4D effects are detectable in the amplitude domain, once the seismic spectra broadens after inversion, the vertical resolution increases, and more energy is recovered. An average map between the reservoir top and base may not be sufficient to capture all the 4D features and sets of vertical information. Figure 17 shows two vertical cross sections: the amplitude difference and the IP ratio (RIPP) between monitor 3 and baseline, with the reservoir top, middle (dashed) and base plotted in black. Figure 17 b shows both the resolution enhancement as compared to Figure 17 a. This example indicates that RIPP maps extracted between the same reservoir interval range as the amplitude domain may result in different information. It also shows some requirement to carefully attenuate the sidelobe effects out from the RIPP maps.

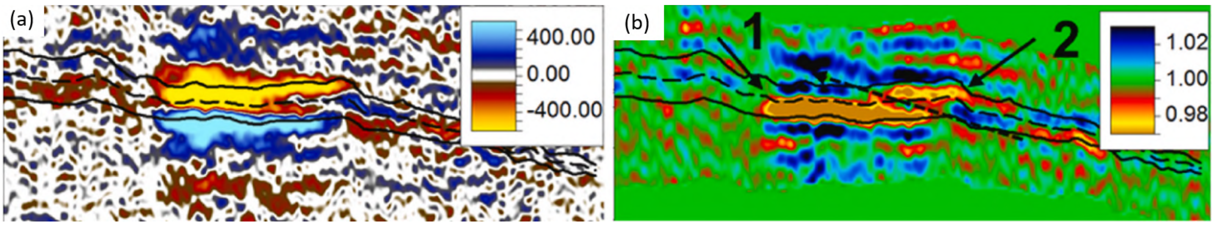

Figure 17 - Vertical cross-sections of observed 4D amplitude difference (a) and RIPP (b) between monitor 3 and baseline. The diagonal dashed line in (b) shows a channelized feature separation into regions 1 and 2 which were not as evident in the amplitude domain. Modified from ROSA; SCHIOZER; DAVOLIO (2022).

ROSA; SCHIOZER; DAVOLIO (2022) proposed one mitigation strategy to filter the sidelobes defining sidelobe polygons manually, within which the sidelobes were defined as RIPP=1 (no 4D changes). These values were applied to the RIPP average map between the top and base of the reservoir. The mapping window between top and base of the reservoir were selected in order to maintain consistency with the amplitude domain. Figure 18 shows the clustering results of the observed sidelobe-attenuated standardized RIPP map.

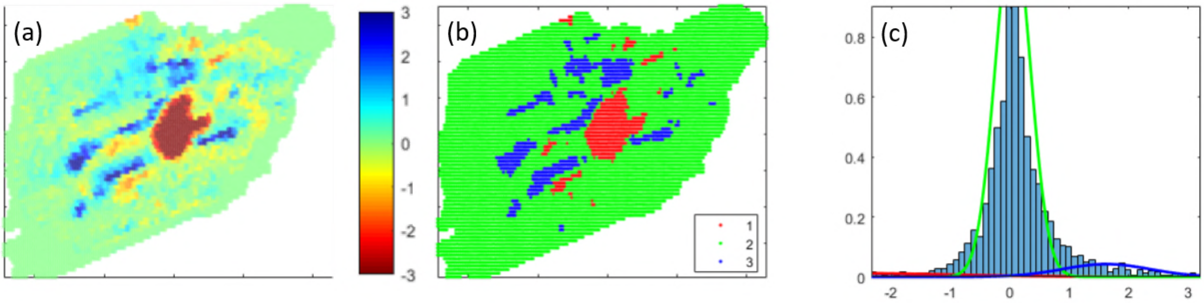

Figure 18 - Clustering results for the sidelobe attenuated RIPP map between the observed monitor 3 and baseline: (a) RIPP, (b) clustered map, and (c) Gaussian mixture models.

Another more straightforward option is to make block-by-block comparisons (volume-based comparisons instead of maps), however, downscaling and filtering the sidelobe energy in a 3D volume at the reservoir model scale is unpractical, and therefore it was not tested in this application.

5.6.3 Feature/shape extraction in the saturation/pressure domain

The cross-domain is an interesting adaptation of the workflow because it skips the PEM and the forward modeling steps. The workflow extracts saturation and pressure properties from the simulation results to be compared instantly to a given observed 4DS amplitude map.

As discussed in chapter 2, a few authors have proposed techniques to make the direct cross-domain comparisons; however, they suggest simplifications without considering the ambiguous (or destructive) aspect of the 4DS effects, which have been demonstrated to be relevant in this study. For this reason, we performed an initial assessment of which dynamic properties could be extracted from the simulation models and cross-correlated with seismic attributes with minimal inaccuracy.

Figure 19 shows crossplots for the average of the 200 maps, between the $dRMS_{syn}$ and the saturation/pressure differences measured for the monitor 3 vs. baseline in the S4D_post_WS set. Table 3 shows the correlation coefficients between each physical effect and the $dRMS_{syn}$ for the average maps, calculated using the points inside the grey rectangle areas from Figure 19. The crossplots suggest the dynamic physical effects that can be directly correlated with the $dRMS_{syn}$ are the water, oil and gas saturations differences in the points located at the quadrants Q2, Q3 and Q1 respectively. For the oil saturation difference (dSo), the points in quadrant Q3 correspond to the areas where water replaced oil (quadrant Q2 in Figure 19 a) and the water saturation increased. Therefore, we consider the crossplots from Figure 19 a and b complementary, except for the region near the red arrow in Figure 19 b, where the points are slightly shifted from 0 downwards. This is explained by the gas going out from solution effect points that show the gas saturation increase, strongly correlated with negative $dRMS_{syn}$ values in the quadrant Q1 from Figure 19 c.

As discussed in the initial modeling (section 5.4.1), the pore pressure effect is not significant in the field S. Figure 19 d shows a poor correlation between the decrease in pore pressure and $dRMS$ (correlation coefficient of -0.141), which suggests the presence of ambiguous effects, where the saturation signal is dominant. For this reason, the water and gas saturation difference (dSw and dSg) maps were selected for the cross-domain comparisons presented in this section.

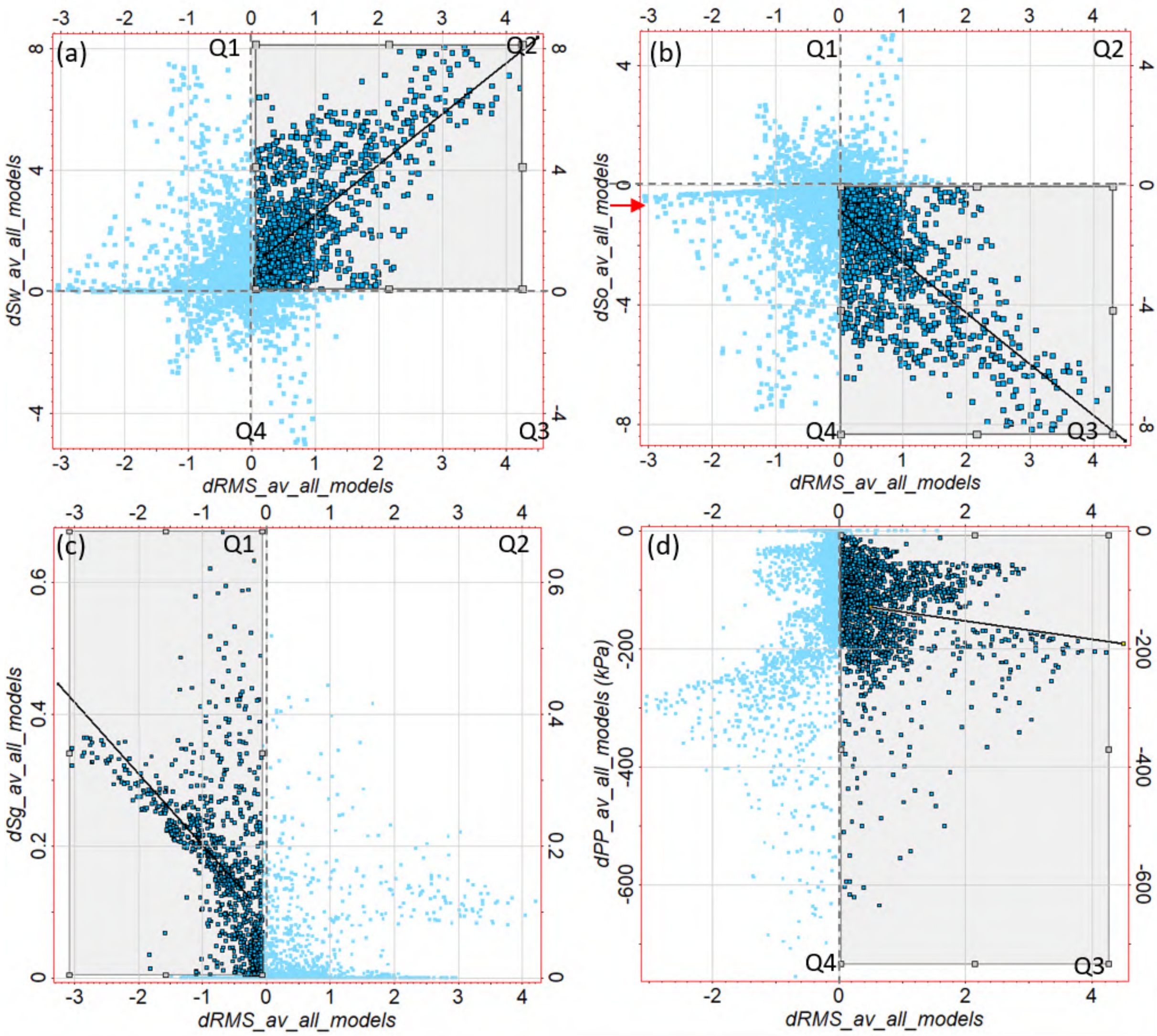

Figure 19 - Average of 200 $dRMS_{syn}$ vs. average of 200 dSw (a), dSo (b), dSg (c) and dPP (d) – the differences are between monitor 3 and base, modeled for set S4D_post_WS. The dashed lines divide the crossplots through a zero point into quadrants Q1 to Q4. The grey rectangles highlight the areas where the correlation coefficients were calculated at.

Table 3 - Correlation coefficients for the analyzed physical effects.

Physical effect	Correlation coefficient (r)
dSw	-0.1410
dSo	0.6909
dSg	-0.6979
dPP	-0.527

This analysis suggests that the hardening cluster obtained from the $dRMS_{obs}$ map can be fairly compared against the increase in water saturation cluster from the modeled dSw map. The softening cluster can be compared with the increase in gas saturation cluster from the modeled dSg map.

It is important to stress there is an inherent correlation between the $dRMS_{syn}$ and the dynamic properties because the $dRMS_{syn}$ uses a PEM, whose parameters include these dynamic properties themselves. We highlight the PEM's calibration discussed in section 4.3 is sufficient to assume this correlation is the consequence of the physical effects.

The values in Table 4 are the initial conditions for each modeled saturation difference map, which were selected based on tests, adapted to the different saturation ranges.

Table 4 - Value initialization for each cluster k (water and gas saturation domains).

Cluster	dSw		dSg	
	μ	$\sigma 2_{obs}$	**μ**	$\sigma 2_{obs}$
k_1	-0.7	0.05	-0.01	0.0005
k_2	0	0.001	0	0.00001
k_3	+0.7	0.05	+0,01	0.0005

Figure 20 shows the clustering results obtained for the dSw and dSg maps. As only their increase in saturation will be compared against the $dRMS_{obs}$, the clustering is simplified as 0 = absence of increase in saturation and 1 = increase in saturation.

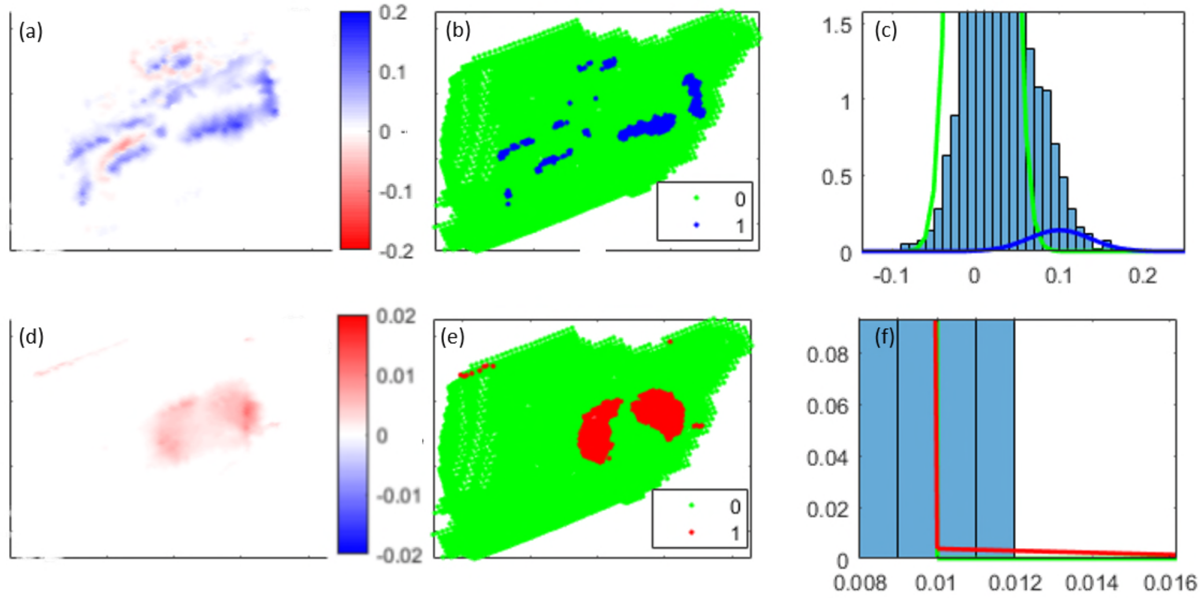

Figure 20 - Saturation difference, ternary map and Gaussian models (a) to (c): dSw and (d) to (f) dSg. The maps are an average of all layers between reservoir top and base. Examples from model 1, monitor 3 vs. base, set S4D_post_WS.

5.7 Combining the shape and magnitude metrics

This section shows the results in several reservoir management key steps. We used the monitor 3 vs. baseline comparison maps, because it displayed most variety in 4D anomalies' shape and magnitude (refer to Figure 7) to demonstrate their applicability. The sub-sections 5.7.1 to 5.7.4 present discussions in where the diagnosis was performed in the amplitude ($dRMS$) domain. Section 5.8 presents a comparison between the diagnosis obtained at different domains, where we review if the reservoir management decisions are different depending on the selected one. The sub-section 5.8.1 shows a comparison between IP and amplitude domain diagnosis, and the sub-section 5.8.2 demonstrates interesting discussions on the saturation domain and how its diagnosis compares with the previous two. Finally, the APPENDIX A shows tests performed in other monitors, with different levels of noise and repeatability.

5.7.1 Evaluating geomodeling

In the closed-loop field development and management workflow, it is common to have various iterations of geomodeling as new information is acquired and as the knowledge on the field's behavior increases, the need to generate new prior models emerges. One approach to quantify improvements within these iterations is to measure errors against observed data. Conventionally, a simulation model uses quadratic errors against well production data, which are very local measurements and do not always reflect problems from the geological model.

The 4D similarity metric complements the error evaluation due to its spatial significance. Figure 21 a and Figure 21 b show a shape and magnitude measure, respectively, for two sequential iterations of geomodeling (set S3D in blue and set S4D in black), highlighting two problematic regions: P5+P6, in which both magnitude and shape mismatch are higher than other regions, and P9, with higher shape errors. They also show that the improvement from geomodeling set S3D to set S4D is not very straightforward to quantify. For example, the I2 region improves for the shape metric but not so much for the magnitude one. The crossplots from Figure 22 highlight that the shape and magnitude metrics do not always present a good correlation, suggesting that the decisions to reject or accept a certain model would be different depending on the kind of error metric used.

Region P5+P6 is highly influenced by a strong gas anomaly, which affects the errors the most. Figure 23 and Figure 24 show the best and worst models selected by both metrics in set S4D considering only the region P5+P6. The ranks obtained from both metrics are very similar, where the same models are considered top best and top worst at both, differing by only a few positions. In fact, there is a strong correlation between both metrics in this region, which is illustrated in Figure 22 e.

The introduction of features detected on the 4DS monitor and better knowledge of vertical heterogeneities on set S4D decreased the P8, P9 and P10 shape errors. However, this is not detected by the magnitude metric from regions P8 and P10, and the crossplots from Figure 22 f and Figure 22 h suggest a poor correlation between both metrics for these two regions. The shape error also decreases significantly for region I2 between iterations from set S3D and set S4D.

Figure 25 shows the region I2 case in detail for both sets S3D and S4D, demonstrating that although the median of the magnitude errors did not change significantly, the set S4D does not have anomalously high errors models as S3D. The worst models for the shape metric (red points) and for the magnitude metric (black points) from set S3D are indicated in the set S4D, being collapsed toward the shape and magnitude error means, which occurred even without running well/seismic data assimilation. Figure 26 a and b illustrate 5 of these worst models ranked in region I2 according to the shape and magnitude metric, respectively, at set S3D and their similarity improvement in set S4D.

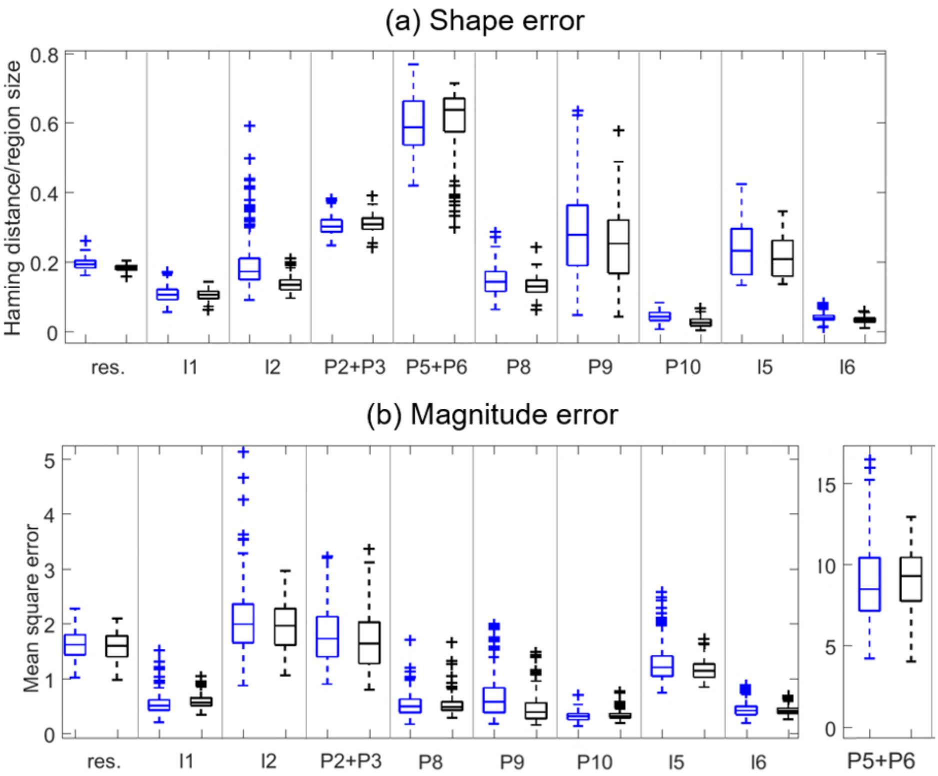

Figure 21 - (a) Shape error and (b) magnitude error for the set S3D (blue) and set S4D (black). Note the error scale difference for P5+P6 due to higher error.

Although the metrics flag some regions to address in the geomodeling iteration (from set S3D to set S4D), an actual improvement was observed only after the model calibration/data assimilation process, as shown in the next discussion (5.7.2) for the region P5+P6 case.

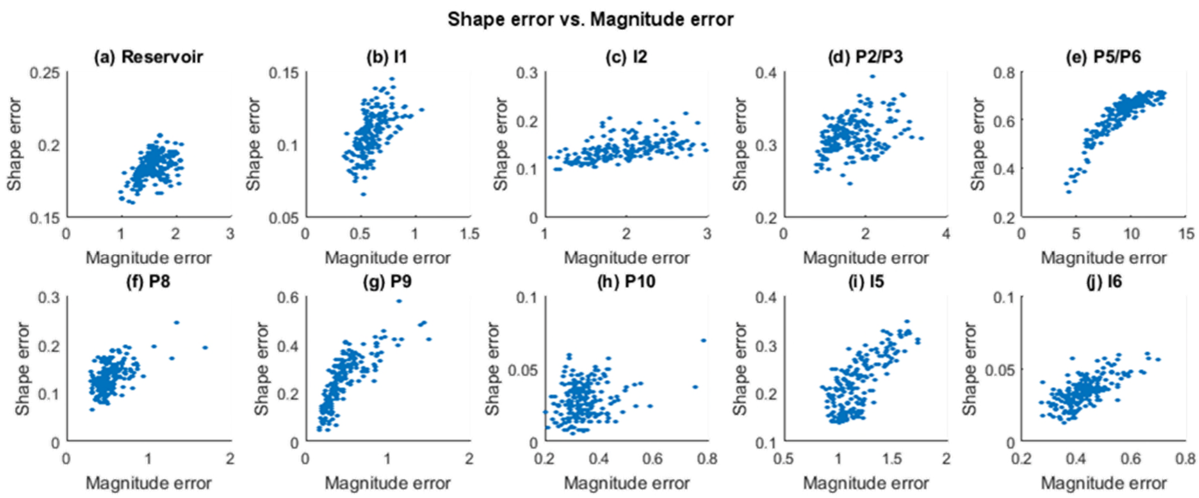

Figure 22 - Shape error vs. Magnitude error for set S4D.

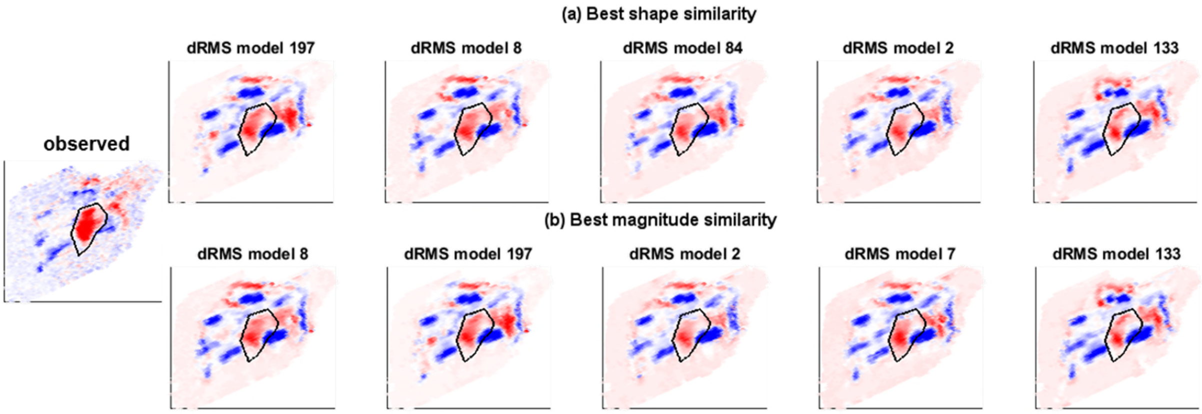

Figure 23 - Best 5 models according to (a) shape and (b) magnitude similarity with 4DS (set S4D), measured at region P5+P6 defined by the black polygon.

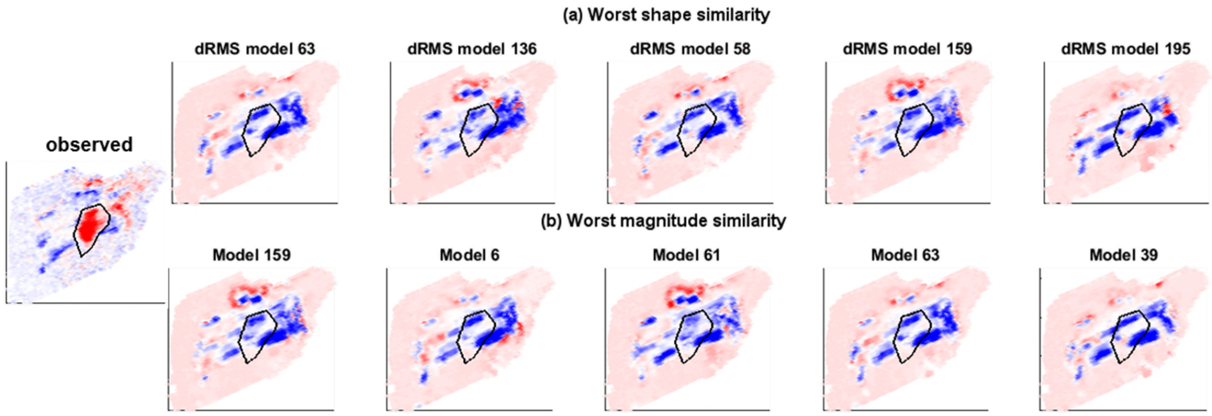

Figure 24 - Worst 5 models according to (a) shape and (b) magnitude similarity with 4DS (set S4D), measured at region P5+P6 defined by the black polygon.

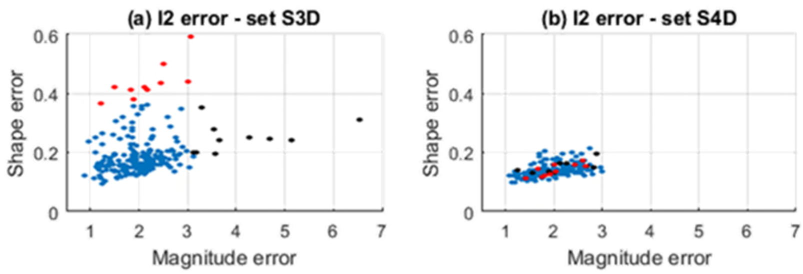

Figure 25 - Shape error vs. Magnitude error for region I2 at set S3D (a) and set S4D (b). The red and black points are the highest errors from the shape and magnitude metrics, respectively.

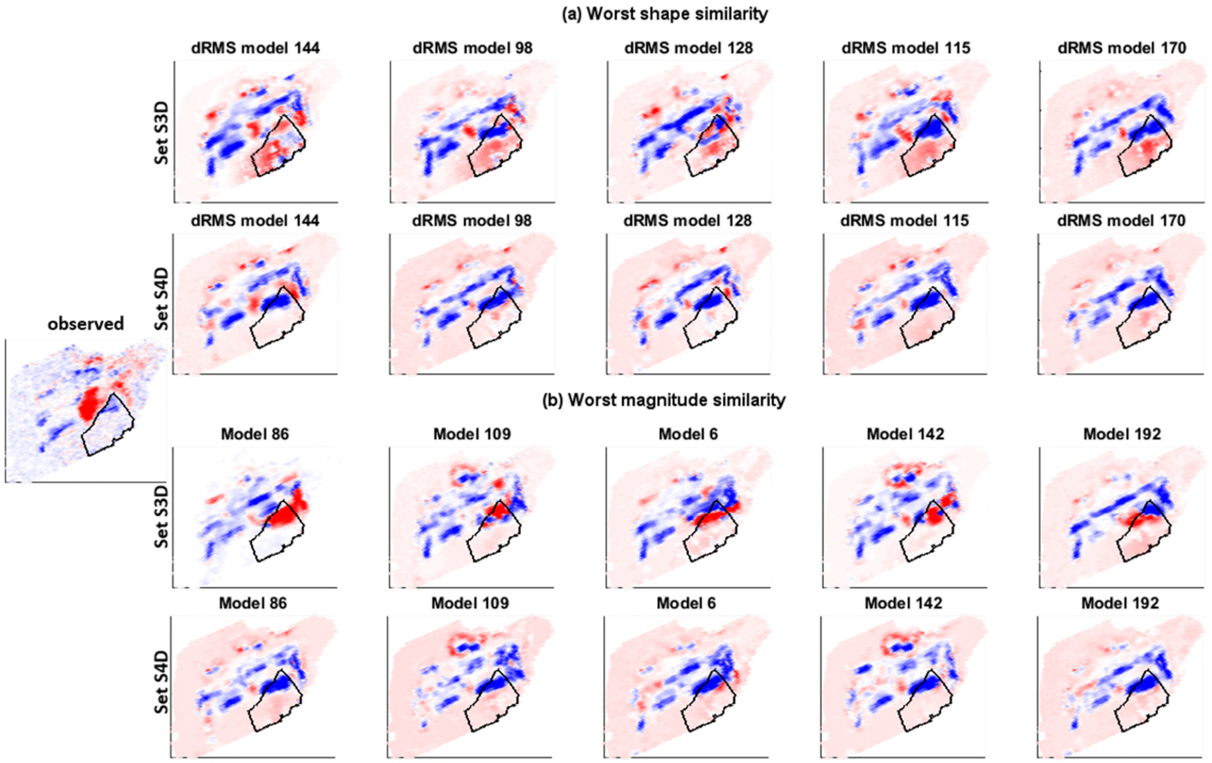

Figure 26 - Worst 5 models according to (a) shape and (b) magnitude similarity with 4DS measured at set S3D for region I2 in the black polygon. The bottom figures show their similarity increase in set S4D.

5.7.2 Evaluating data assimilation

Figure 27 shows a comparison between the set S4D from the previous section before data assimilation (blue), after data assimilation using only well data (set S4D_post_W, in black) and after assimilation with well and 4D seismic data simultaneously (set S4D_post_WS, in red). Most improvements from data assimilation are visible in the magnitude metric, as the ES-MDA technique uses the least-squares calculation on the data-mismatch objective function. In contrast, the shape errors are larger or similar after data assimilation in regions such as P2+P3, P8, P9, and I5.

Region P5+P6 presents an error decrease after data assimilation for both metrics. The data assimilation process has a significant impact on this region because its effort to adjust a certain sample depends on its error standard deviation. This region contains a strong 4D anomaly with larger standard deviation error; thus, its error level decreases toward the same error level as the other regions. This analysis suggests that an objective function balancing may improve the data assimilation impact in other regions.

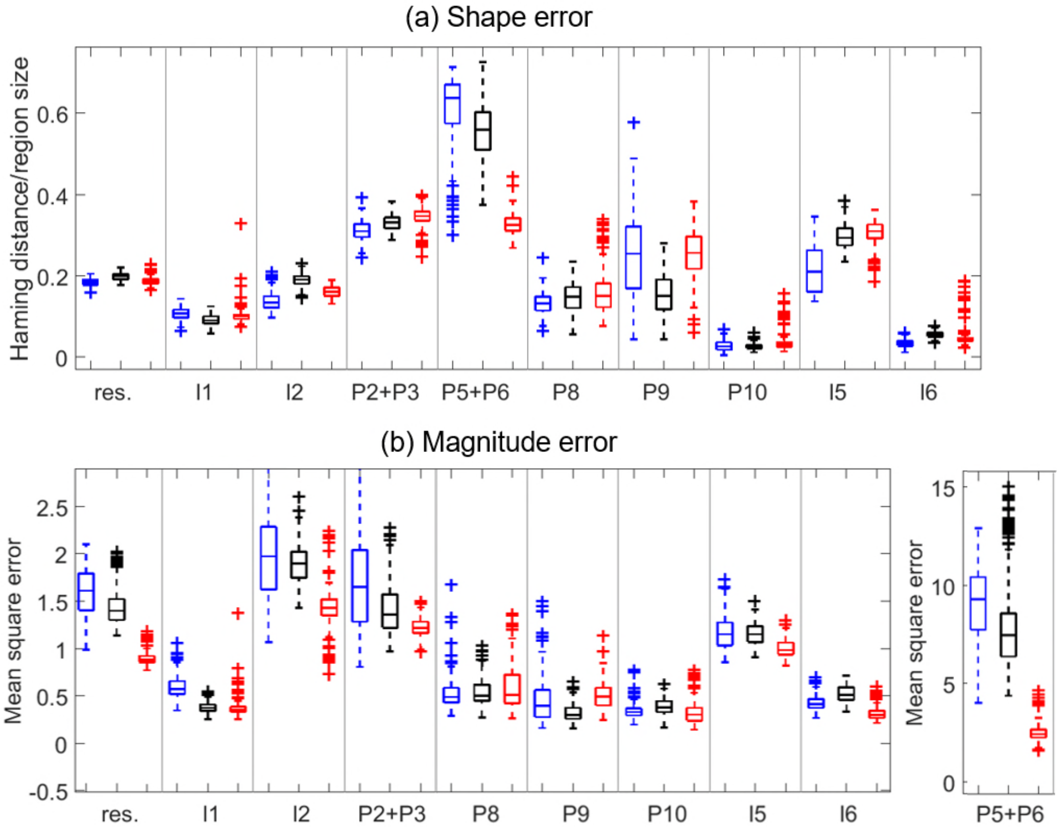

Figure 27 - (a) Shape error and (b) magnitude error for the set S4D (blue), set S4D_post_W (black), and set S4D_post_WS (red). Note the error scale difference for region P5+P6 due to higher error.

Figure 28 shows the models whose errors are closest to the median error from each of the three sets, using both the shape (Figure 28 a to c) and magnitude (Figure 28 d to f) metrics, highlighting the incremental 4DS similarity improvement as the 4DS is assimilated, as expected. The median error map analysis presented in Figure 28 also suggests that at least 50% of the models (higher error half) for the two sets S4D and S4D_post_W do not sufficiently represent the expected 4D signal at region P5+P6, enhancing the need to quantitatively assimilate the 4DS data for these models. Note that the same does not occur for all regions; for instance, the data assimilation did not perform very well for region P8 and P9 – these regions have weaker and smaller anomalies then the others and the data assimilation effort is less.

The methodology assisted us in evaluating the data assimilation results of various sets resulting from different data assimilation parameters within 2 days (i.e., steps 3.2.3 to 3.8 from the workflow).

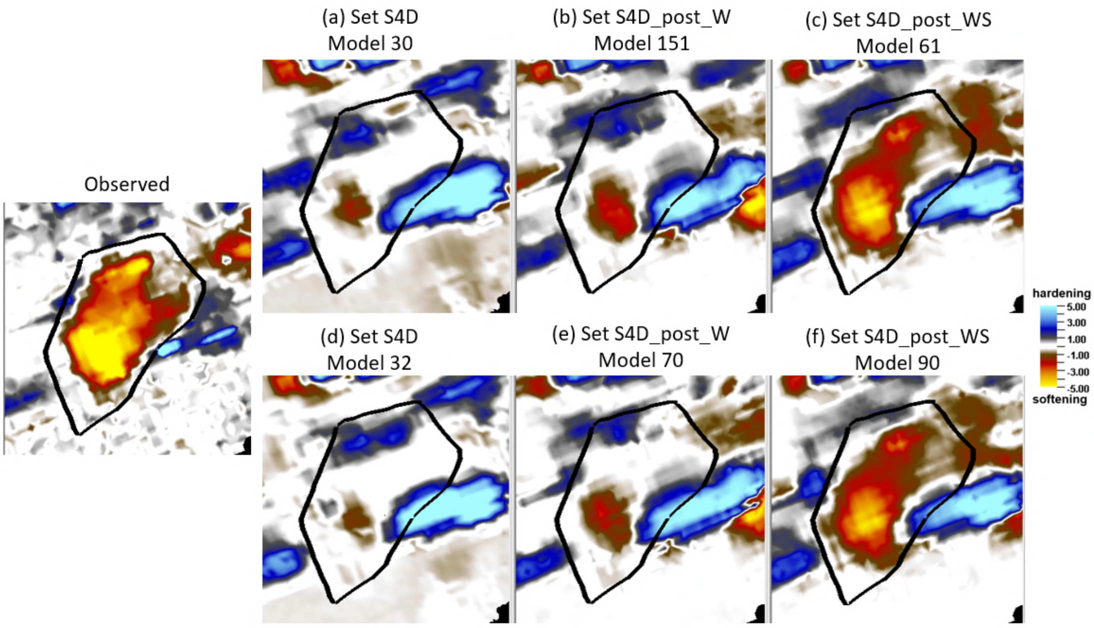

Figure 28 - Models with errors closest to the median error measured at region P5+P6 for models from set S4D, S4D_post_W, and S4D_post_WS. (a) to (c) Use the shape metric, and (d) to (f) use the magnitude metric.

5.7.3 Multi-objective filtering

The previous applications demonstrate that both magnitude and shape metrics are complementary. This section proposes to filter models using the metrics individually for each region and each metric. The crossplots from Figure 29 show that the correlation between both metrics in some cases worsens as the errors increase. This is demonstrated by the models from Figure 30 and Figure 31: the best models according to the entire reservoir error look similar for both metrics, but the worst do not. In addition, a global error given by the sum of magnitude and shape metrics may have a good overall average error for the entire reservoir, but local errors can vary depending on the region. Model 11, represented by the red cross in the crossplots from Figure 29, presents the best overall error (lowest sum of magnitude and shape errors for the entire reservoir). However, crossplots from Figure 29 b, e, f, i and j show that this model is ranked as intermediate for these regions. The green arrow 1 from Figure 32 indicates the lack of softening anomaly from injector I1 (water pushing oil) in this model, arrow 2 shows a non-existent softening anomaly in the observed data, incorrectly predicted by the model, and arrow 3 shows a major magnitude and shape mismatch for the hardening anomaly caused by the water saturation increase. Also note the anomaly from region I1 is not contained, invading part of region P9, which also affects its error.

The examples suggest that ranking and selecting models using error cutoffs considering each region and each metric separately is a better solution than summing and averaging errors, as we guarantee that all regions are simultaneously good. We propose filtering out high error models according to their statistical measures, as defined in equations (13) and (14) from section 3.8. The workflow provides lists of multiple high error models, and for a model to be considered good, it must be simultaneously not contained in any of the lists, resulting in the black square outlines from Figure 29 crossplots. Additionally, the framework proposed to evaluate 4DS misfits, as in Figure 30 and Figure 31, can maximize the models assessment for some goals, such as defining an infill drilling position.

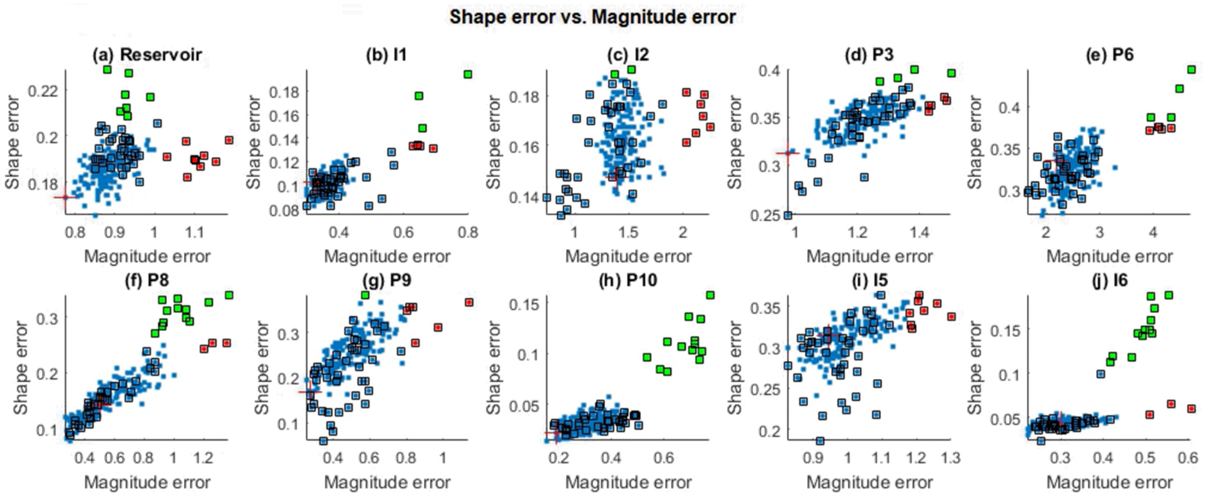

Figure 29 - Shape error vs. Magnitude error for set S4D_post_WS. The red plus sign represents model 11. The green models were filtered by the shape metric and the red, by the magnitude metric in each individual region. The black square outlines are the final outlier (high error) models, selected by the multi-objective filtering procedure using all regions and both metrics.

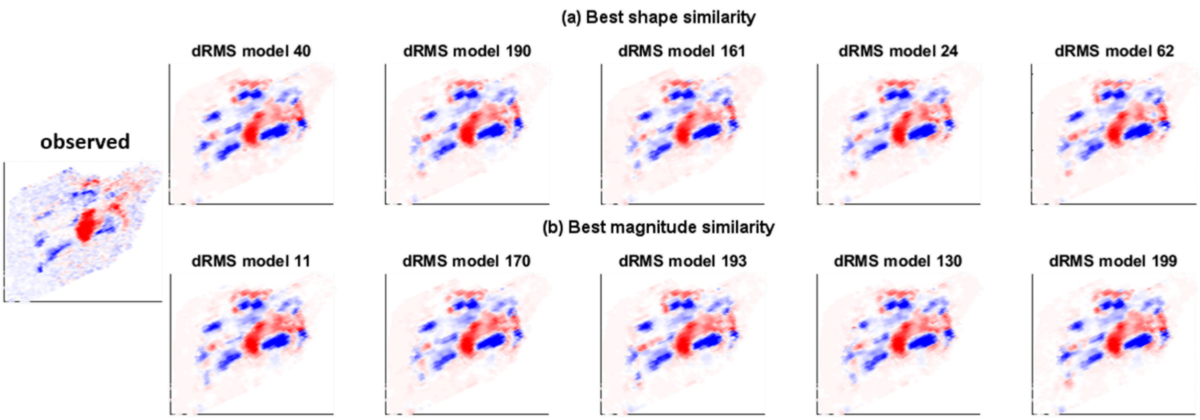

Figure 30 - Best 5 models according to (a) shape and (b) magnitude similarity with 4DS (set S4D_post_WS), measured at the entire reservoir.

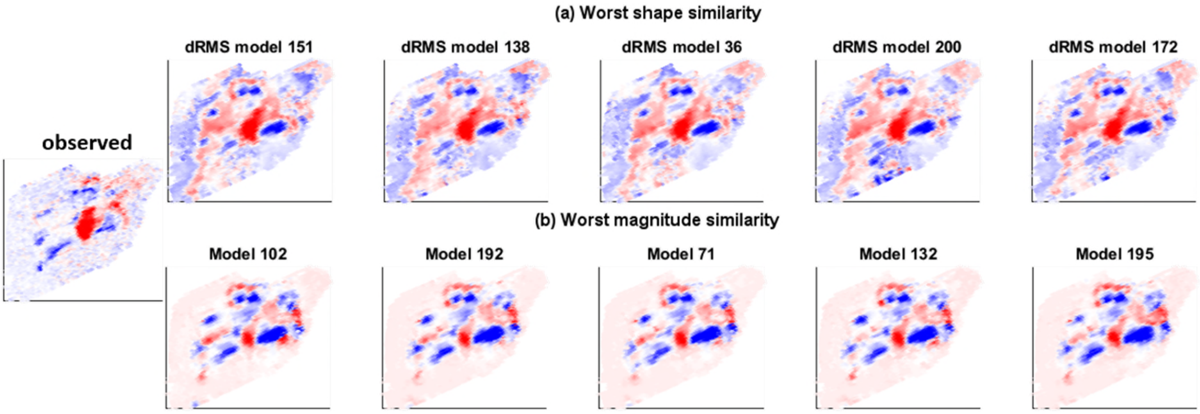

Figure 31 - Worst 5 models according to (a) shape and (b) magnitude similarity with 4DS (set S4D_post_WS), measured at the entire reservoir.

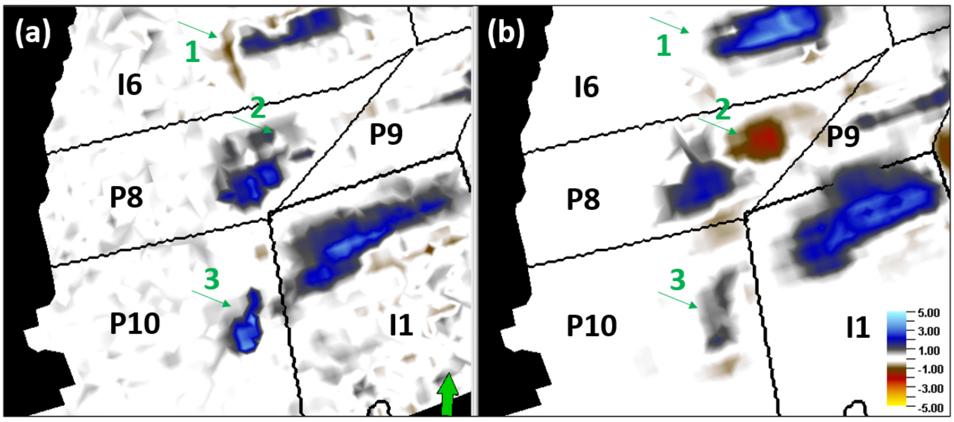

Figure 32 - Region details of (a) $dRMS_{obs}$ and (b) Model 11 $dRMS_{syn}$ at set S4D_post_WS.

5.7.4 Adding a new monitor survey

A new seismic monitor (monitor 5) was acquired, and the workflow assisted us in quickly evaluating if the simulation models were honoring the new vintage. Figure 33 a and b show the shape and magnitude error for set S4D_post_WS, and its comparison with the errors calculated from the monitor 3 vs. baseline. Although the data assimilation of set S4D_post_WS did not include monitor 5 (only monitor 3), the metrics suggest that the models were able to generally honor the subsequent seismic vintage. The problematic P5+P6 region magnitude error decreased, and its error shifts to the same level as the other regions because the gas anomaly becomes weaker, visible in the black arrow at the observed map from Figure 34. The boxplots from Figure 33 show that the highest magnitude and shape errors now occur in region P2+P3. This is explained by two reasons. The first is that the observed anomalies previously detected in previous monitors for this region diminished, while they are still somewhat predicted by the models. The second is that the modeled 4D signal from neighbor region I2 is not contained within this region, and it extrapolates toward region P2+P3 (black arrows from Figure 36).

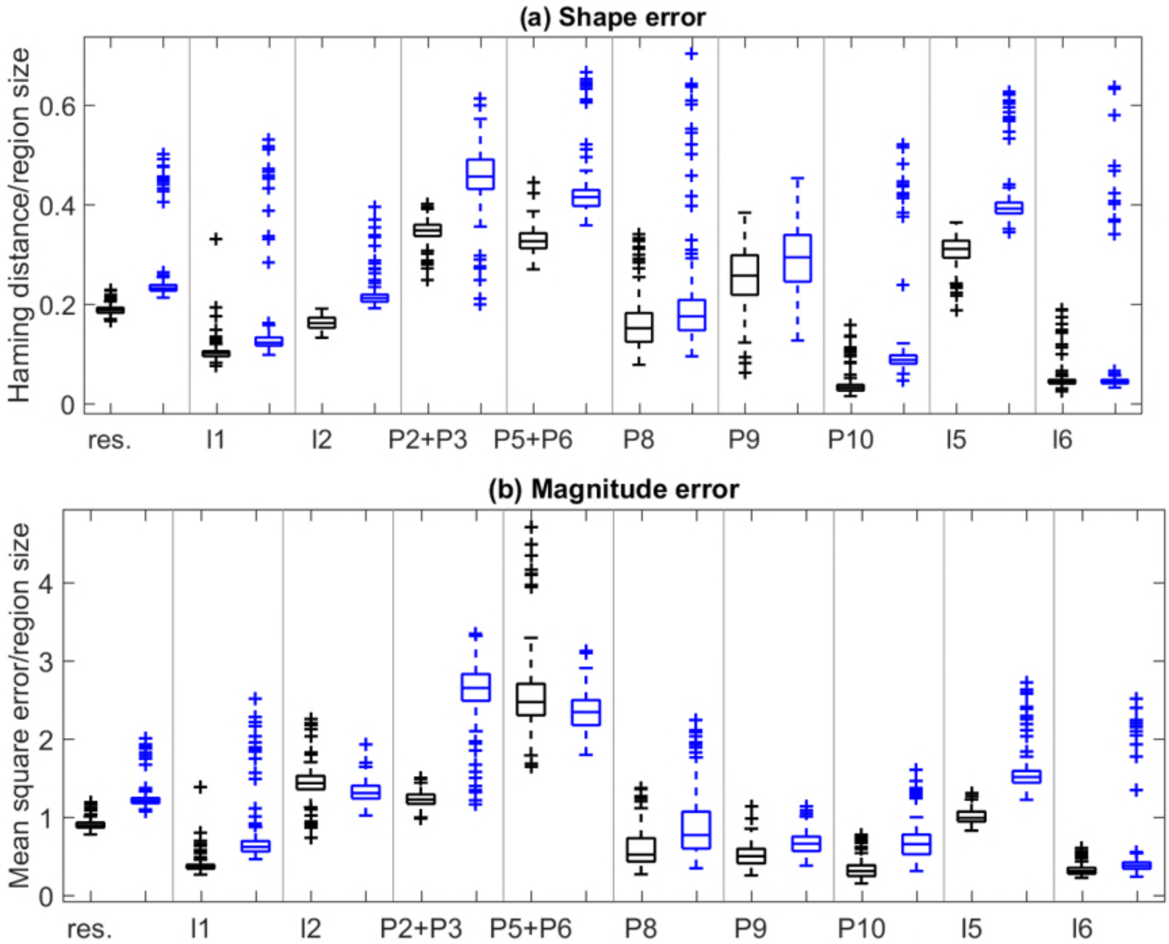

Figure 33 - (a) Shape error and (b) magnitude error for set S4D_post_WS – monitor 3 vs. baseline (black) and new monitor (monitor 5) vs. baseline (blue).

Figure 34 and Figure 35 show the best and worst models, respectively, considering the shape and magnitude metrics for set S4D_post_WS, measured at the entire reservoir. The best model examples generally honor the latest seismic monitor. Figure 37 shows the error crossplots, highlighting in red the outlier models picked for each metric/region. Figure 38 shows the high error models that were filtered out based on the monitor 3 vs. baseline similarity metrics shown in Figure 29 (black dots, 48 models), the ones filtered out based on the monitor 5 vs. baseline (red dots, 30 models), and the intersection between the ones that have been filtered out based on monitor 3 and monitor 5 metrics (green dots, 21 models). The blue models are considered to have low error. Although most high error outliers selected using monitor 5 maps had also been selected out at monitor 3, the workflow exemplifies the new seismic monitor indicated further high error models.

The subsequent monitor survey was evaluated without having to review any of the methodology parameters, reinforcing the practical and robust aspect of the workflow. In addition, this analysis supports the decision to assimilate new monitors.

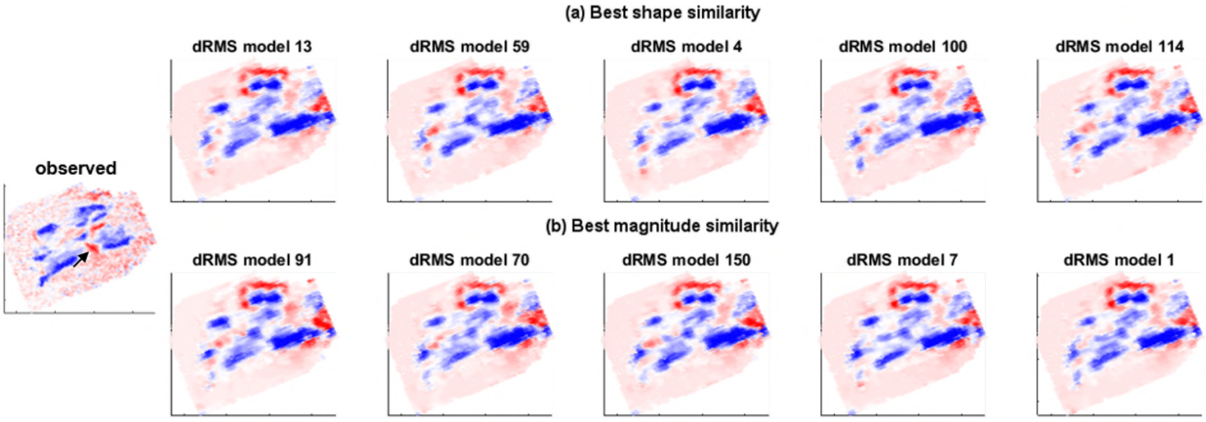

Figure 34 - Best 5 models according to (a) shape and (b) magnitude similarity with 4DS (new monitor 5) for set S4D_post_WS, measured at the entire reservoir.

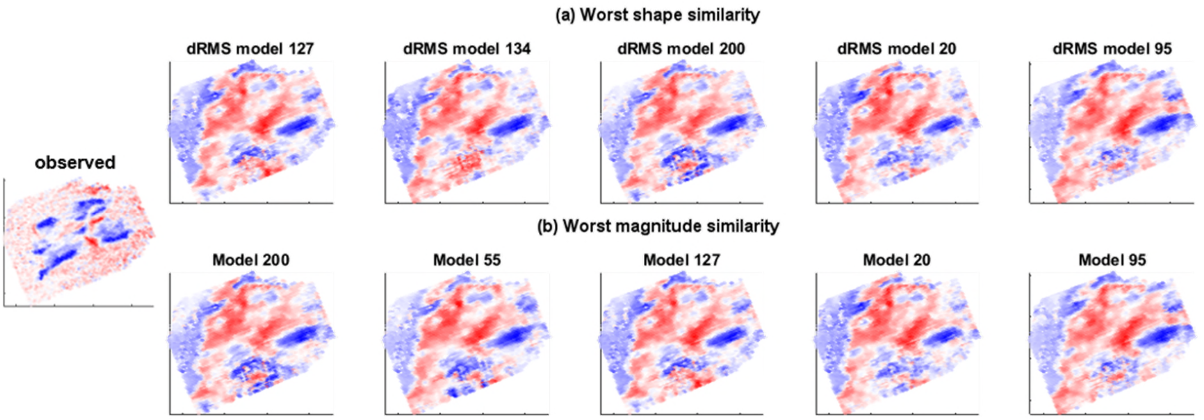

Figure 35 - Worst 5 models according to (a) shape and (b) magnitude similarity with 4DS (new monitor 5) for set S4D_post_WS, measured at the entire reservoir.

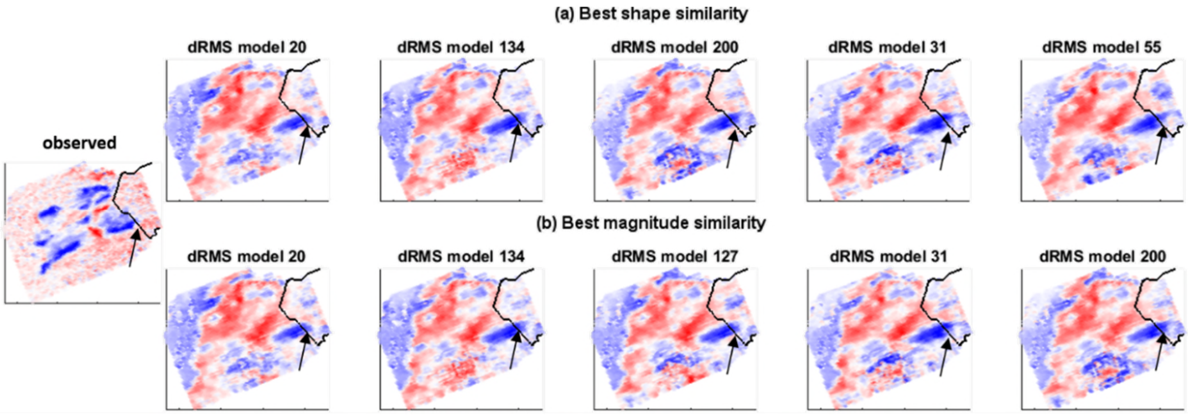

Figure 36 - Best 5 models for region P2+P3 according to (a) shape and (b) magnitude similarity with 4DS (new monitor 5) for set S4D_post_WS.

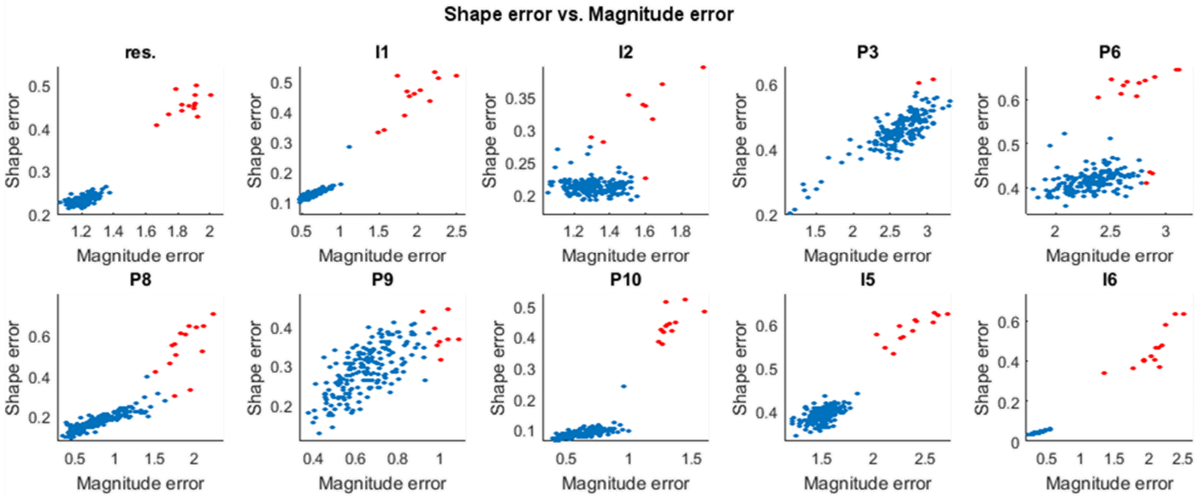

Figure 37 - Shape error vs. Magnitude error for set S4D_post_WS, measured at monitor 5 vs. baseline. The red dots are the outlier models filtered out based on each metric (total of 30 models).

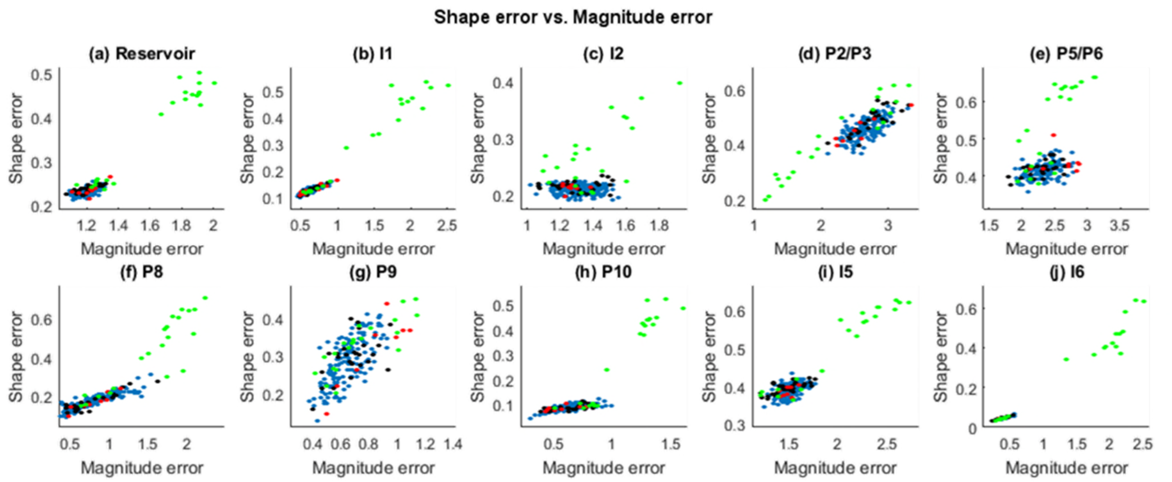

Figure 38 - Shape error vs. magnitude error for set S4D_post_WS, measured at monitor 5 vs. baseline. The black dots are the high error models filtered out based on the monitor 3 vs. baseline maps (48 models). The red dots are the models filtered out based on monitor 5 vs. baseline maps (30 models). The green dots are models filtered out based on monitor 3 intersected with the ones filtered out based on monitor 5 vs. baseline comparison (21 models).

5.8 Comparison between diagnosis performed in different domains

5.8.1 IP vs. Amplitude diagnoses

This section aims to evaluate if decisions such as simulation model ranks and model filtering are different depending on the comparison domain. Figure 39 shows the mapped anomalies are different at several locations, where the main ones are highlighted by the black arrows. This occurs because of different resolutions between both domains, causing differences in both the observed magnitude and shape metrics, as discussed in section 5.6.2.

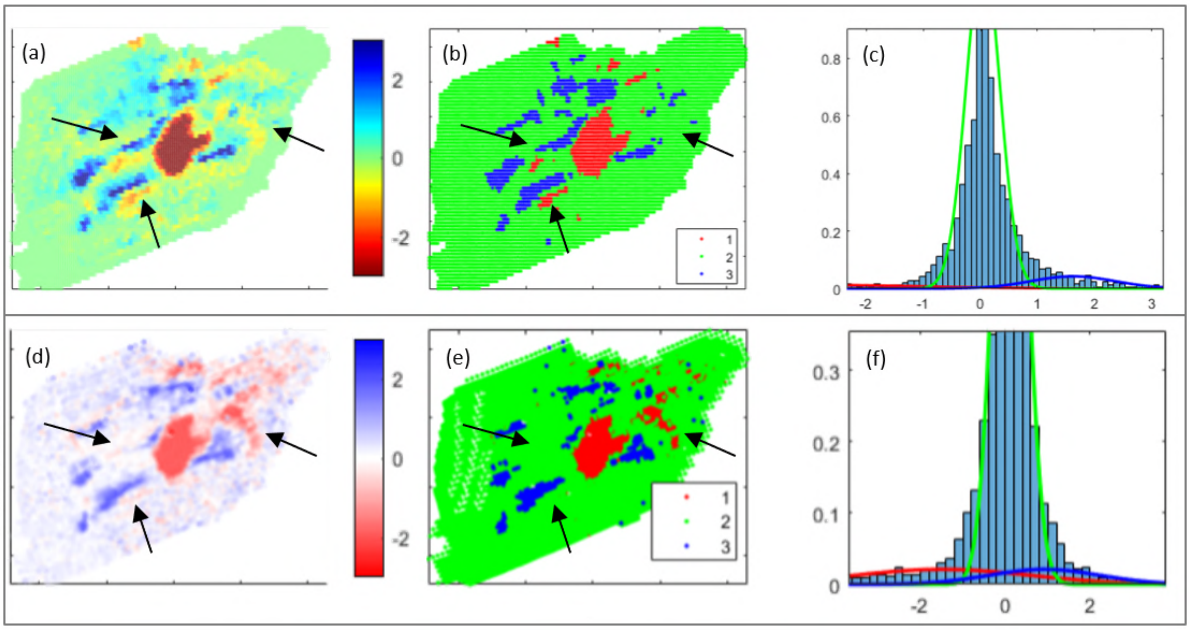

Figure 39 - Seismic attribute, ternary map, and gaussian mixtures for each cluster, for the IP domain (a to c respectively) and $dRMS$ domain (d to f respectively). Maps generated for the monitor 3 vs. baseline comparison, extracted between top and base. The black arrows highlight areas with anomalies differences between both domains.

Figure 40 a and b show a comparison of the shape and magnitude errors respectively, measured in the amplitude (blue) and IP domains (black). The boxplots show differences in errors distributions between both domains. The outliers from the IP domain are more deviated from the mean error models, as compared to the amplitude domain outliers. The mean error between both domains is generally similar, except for the I2 and P9 regions, where for the P9 region, the IP domain shows higher error models, which the causes are discussed in the next illustrations.

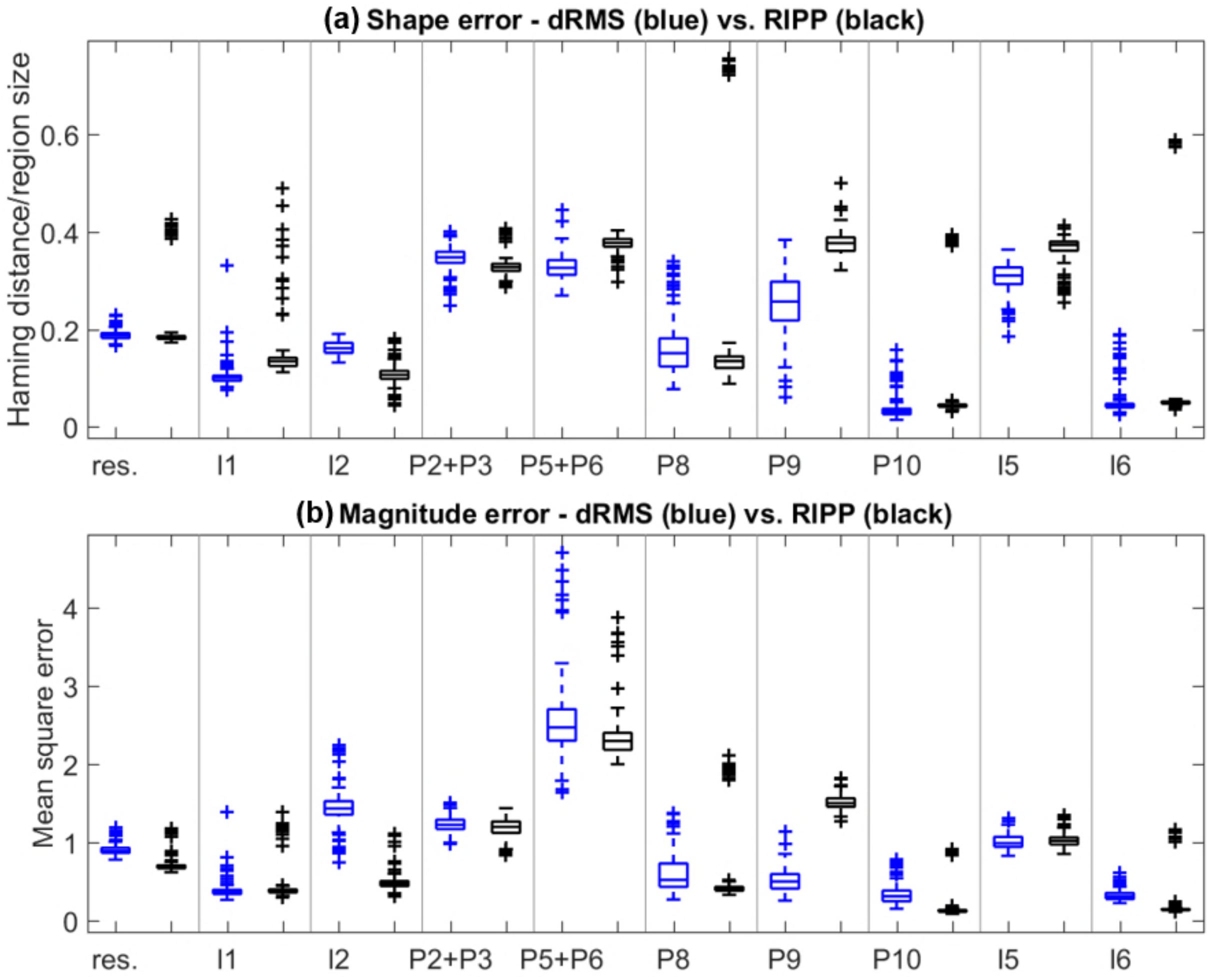

Figure 40 - (a) Shape and (b) magnitude errors measured at set S4D_post_WS in the amplitude (blue) and IP domain (black) – monitor 3 vs. baseline.

Figure 41 shows the filtered models (red points at the crossplots, indicating the bad models) from the IP domain. 26 models were filtered in total, whilst 47 models were filtered in the amplitude domain. Only models 52 and 112 were filtered in the IP domain and not in the amplitude domain, both because of high errors in the P9 region. Figure 42 shows a zoom in this region, in which we can observe an important difference in the observed 4D response in both domains (Figure 42 a as compared to c), where the hardening is stronger and bigger in the IP domain, and there is also a strong softening response sidewards contouring the hardening (interpreted as water pushing oil effect) that is not visible in the amplitude domain.

The absence of this softening caused the model 52 to be flagged as a high magnitude error. Likewise, the softening absence and the hardening shape mismatch seen in Figure 43 d, flagged the model 112 as a high shape error.

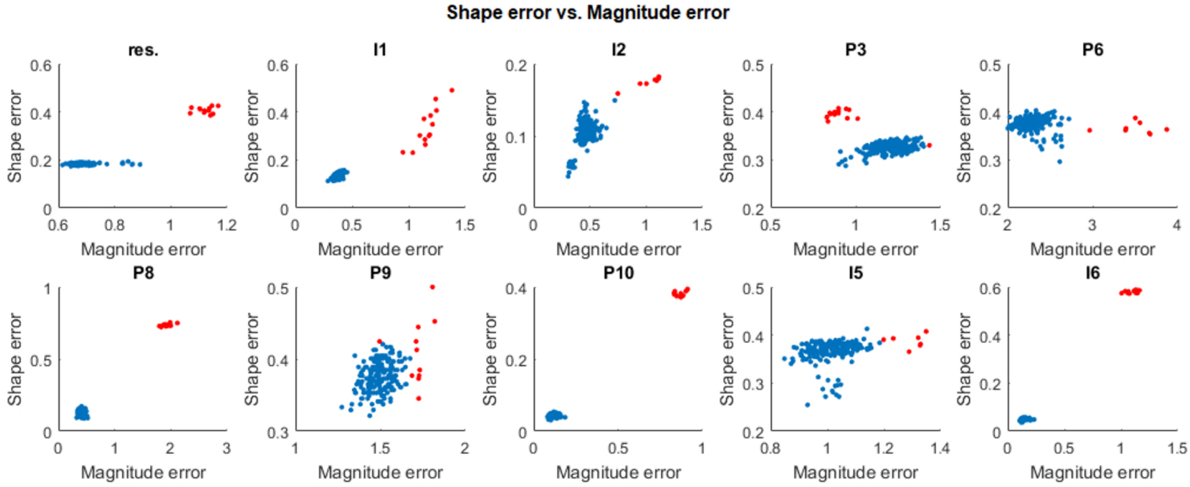

Figure 41 - Crossplots between shape and magnitude errors measured at set S4D_post_WS in the IP domain – monitor 3 vs. baseline.

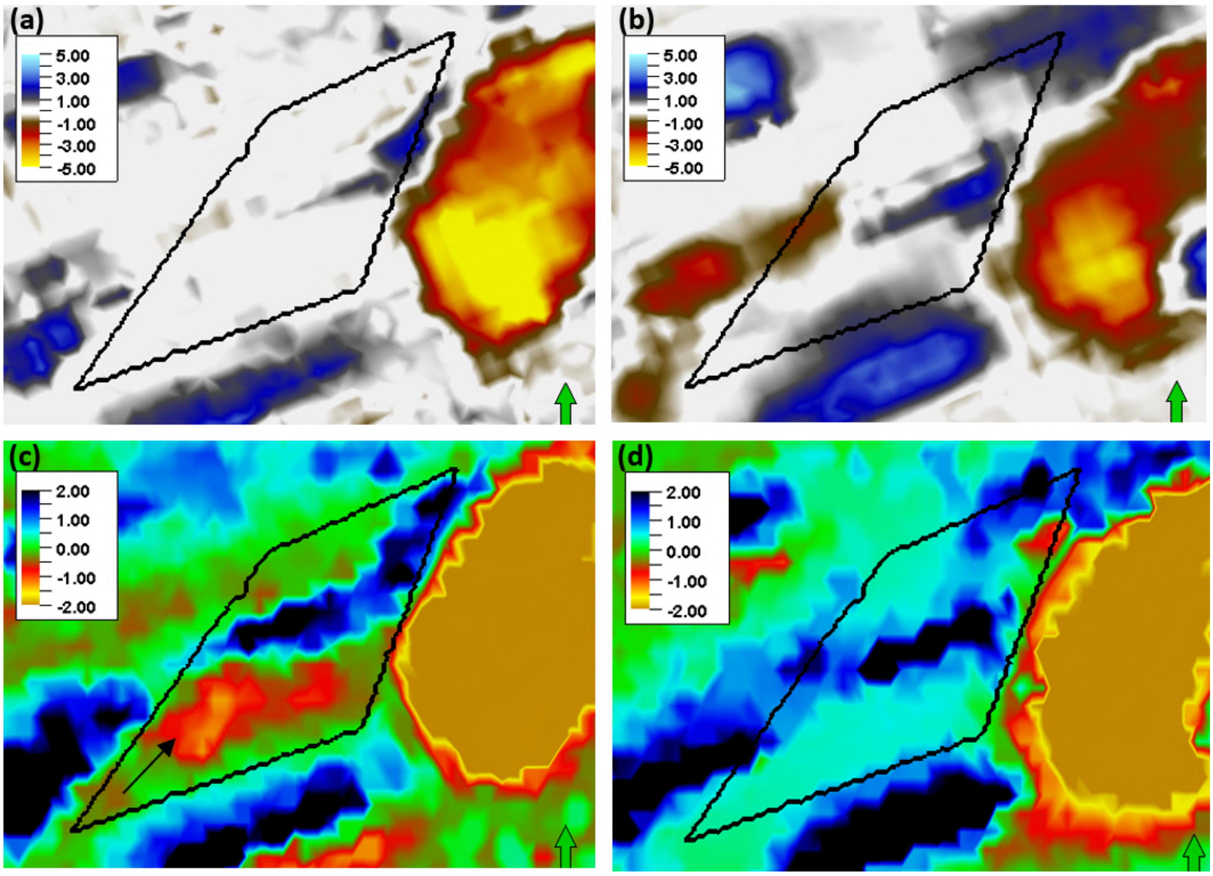

Figure 42 - (a) and (c) observed $dRMS$ and RIPP, (b) and (d) synthetic $dRMS$ and RIPP respectively – model 52, the black polygon is region P9 – monitor 3 vs. baseline.

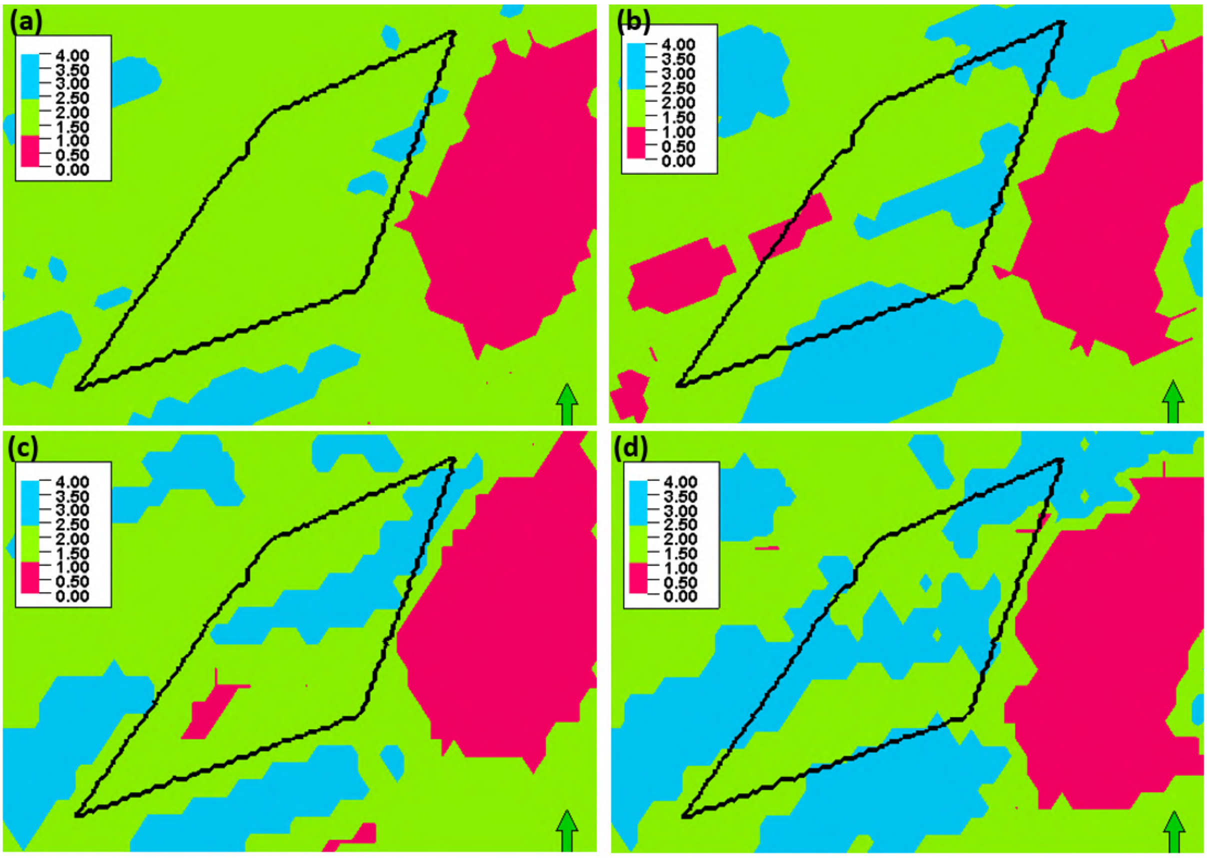

Figure 43 - Observed ternary $dRMS$ (a) and RIPP (c) maps. (b) and (d) are the clusters of the synthetic $dRMS$ and RIPP for model 112. The black polygon is region P9 – monitor 3 vs. baseline.

5.8.2 Cross-domain diagnosis

Although it does not consider all the 4D effects and their competing expression, as discussed in section 5.6.3, the cross-domain diagnosis provides a quick-look on general model errors by regions.

Figure 44 shows the 10 models with worst mismatches between dSw and $dRMS_{obs}$. The anomalies highlighted by arrows 1 and 2 stand out, where the arrow 1 shows an increase in $dRMS_{obs}$ that the models consistently do not predict. This is a hardening anomaly caused by water injection (injector well/region I6). The arrow 2, on the other hand, is in a low confidence area due to tuning and presence of competing effects. Although this is an automatic diagnosis tool, we highlight the importance of some supervision and on the initial interpretation and QC step.

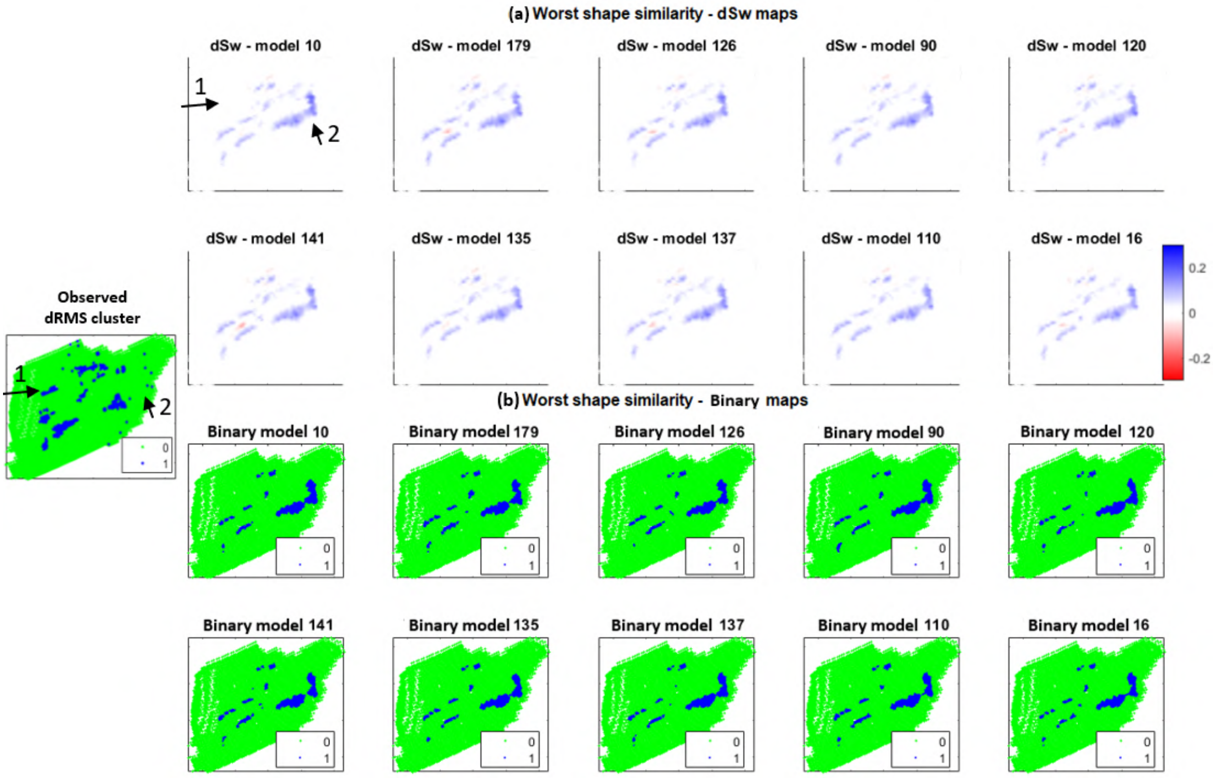

Figure 44 - Worst shape similarity between dSw and $dRMS_{obs}$ maps. (a) dSw maps and (b) their corresponding binary maps. On the left, the $dRMS_{obs}$ binary map showing the hardening cluster in blue and its absence in green as a reference. Set S4D_post_WS, differences between monitor 3 and baseline.

Figure 45 and Figure 46 show the 10 models with best and worst errors between dSg and $dRMS_{obs}$. We can note the size of the gas anomaly from region P5+P6 and P2+P3 affects the model ranking the most (regions highlighted by the black polygons), however, Figure 46 shows the worst models wrongly predicting small gas saturation changes (<1%) throughout other regions. Although these saturation changes are not contained within the presence of dSg cluster, these models are flagged as high errors because of their resulting gas anomaly larger shape. As the gas saturation increase was flagged in the initial modeling as the strongest 4D effect, affecting the data assimilation objective-function the most, this can be a useful quick check after a data assimilation run.

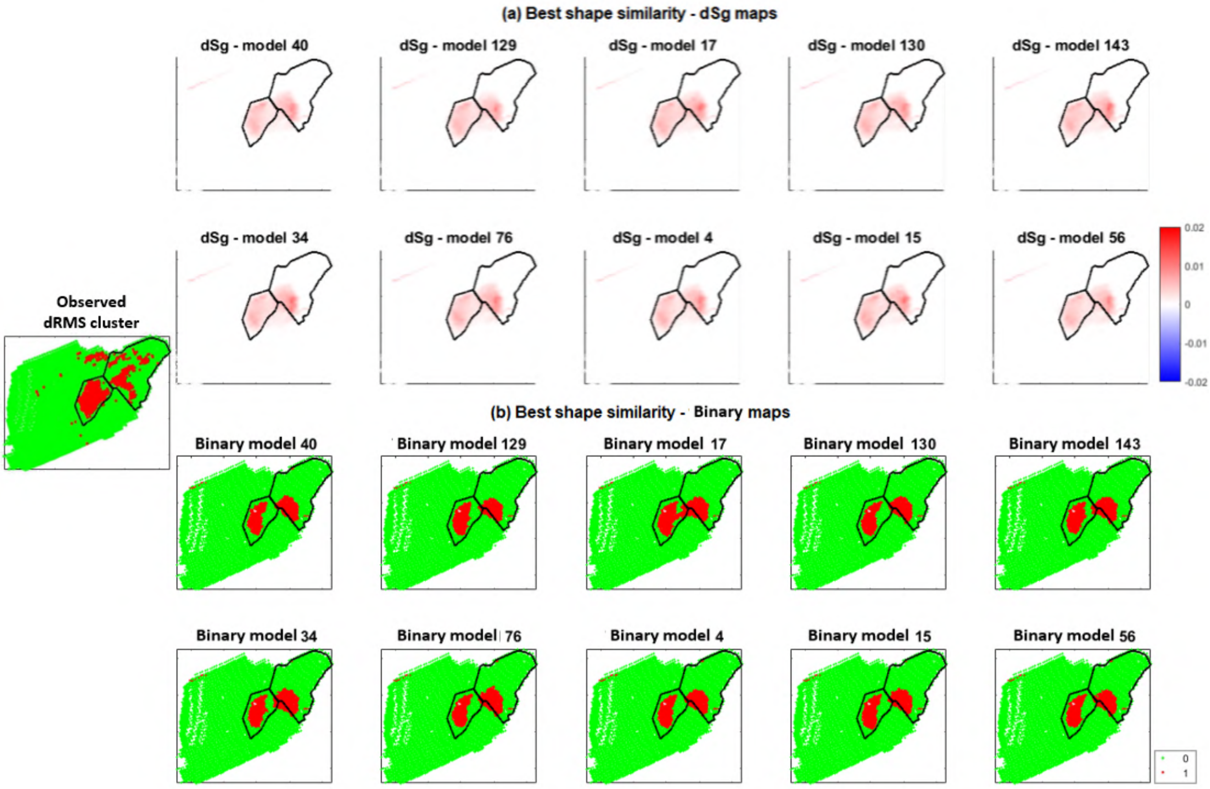

Figure 45 - Best shape similarity between dSg and $dRMS_{obs}$ maps. (a) dSg maps and (b) their corresponding binary maps. On the left, the $dRMS_{obs}$ binary map showing the softening cluster in red and its absence in green as a reference. Set S4D_post_WS, differences between monitor 3 and baseline.

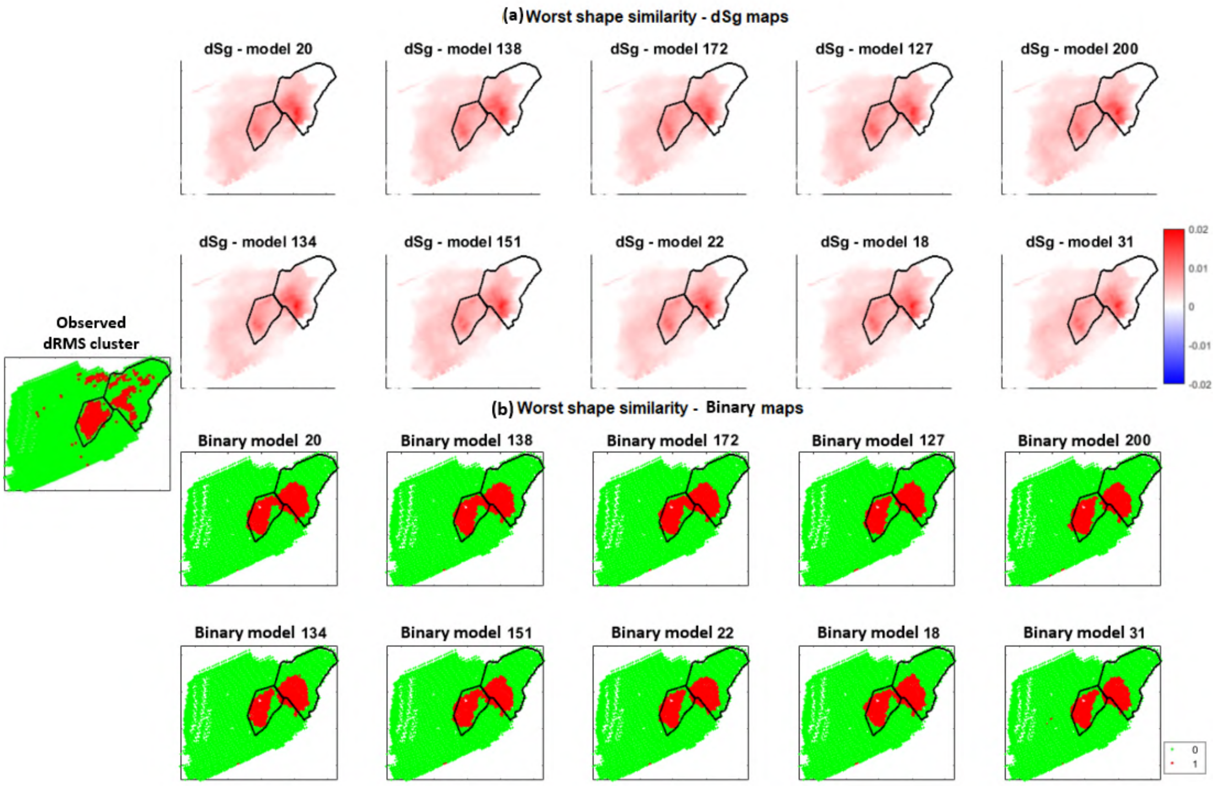

Figure 46 - Worst shape similarity between dSg and $dRMS_{obs}$ maps. (a) dSg maps and (b) their corresponding binary maps. On the left, the $dRMS_{obs}$ binary map showing the softening cluster in red and its absence in green as a reference. Set S4D_post_WS, differences between monitor 3 and baseline.

The cross-domain shape error metrics are compared with the ones obtained within the other domains in Figure 47. We can note the saturation domain has less outlier models than the other domains, except for region P5+P6.

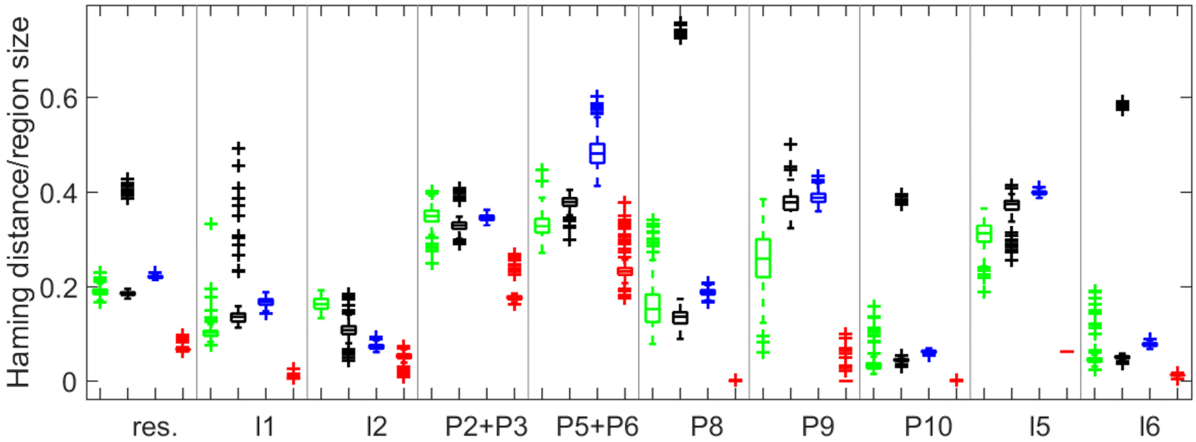

Figure 47 - Boxplots showing shape error comparisons measured in each region, for each domain: amplitude ($dRMS$) (green), RIPP (black), dSw (blue) and dSg (red). Set S4D_post_WS, differences between monitor 3 and baseline.

5.8.3 Pros and cons of each domain

Using the same multi-objective filtering methodology as for the amplitude and IP domain, but with only the shape metric for the cross-domain analysis, the high error outlier models identified from each domain are listed in Table 5. This list shows the amplitude domain identified more high-error outliers to be filtered out. The models in green highlight the models which had been filtered out in the amplitude ($dRMS$) domain, used as reference because it is the domain able to reproduce most of the effects that occur in a real seismic data, such as the frequency content, 4D competing effects, wavelet, and noise. The list reveals that all the filtered-out models identified in the dSg domain had been identified as high errors in the amplitude and the IP domain. The same did not occur in the dSw domain, which is expected because the dSw effect often competes (and loses) against opposite effects, a phenomenon that can only be replicated when performing the forward modeling.

Table 5 - Models filtered out using error metrics measured in the amplitude ($dRMS$), IP, dSw and dSg domains – set S4D_post_WS, monitor 3 vs. baseline comparison. The models highlighted in green are the models which were also filtered out in the $dRMS$ domain.

$dRMS$	RIPP	dSw	dSg
3	3	10	3
14	18	17	18
16	20	18	20
17	22	20	22
18	31	22	31
20	36	27	36
22	52	30	55
31	55	44	71
36	71	49	87
49	87	68	95
55	95	71	102
56	102	79	124
60	112	89	127
68	123	90	132
71	124	91	134
79	127	105	138
82	129	108	151
84	132	117	165
87	134	120	172
91	138	126	192
94	151	133	195
95	165	134	200
102	172	150	
109	192	159	
110	195	160	
118	200	179	
123		197	
124			
125			
127			
129			
132			
134			
137			
138			
143			
146			
151			
155			
165			
166			
172			
181			
192			
195			
198			
200			

In this context, this section aims to discuss the pros and cons of each domain and suggest recommendations for other application cases.

The analysis performed in the saturation domain shows that, in the presence of competing effects, only the wining effect can be confidently used for the diagnosis. This is a useful quick-look tool, however, is overlooks other substantial 4DS information. These results provide further support for the hypothesis that we need a PEM to perform a more comprehensive diagnosis, meaning the amplitude and the IP domains are most suitable for this task.

The amplitude domain comparison is different from the others in a number of respects. It includes more steps, but it is able to reproduce several characteristics identified within this case study, such as competing effects and the frequency content causing the wavelet (sidelobe) effect and noise. The number of steps, however, is mitigated by the automatic workflow developed as part of this thesis.

The IP domain is a very practical option because it outputs layer properties (rather than interface properties) that can be easily transferred to the model grid. This is a requirement in case the objective is to run a seismic data assimilation. However, running inversions can be time-consuming, and less viable in a seismic PRM system with lots of vintages, because it may need to be re-parametrized each time a seismic monitor is available. It may also require some additional pre- and post-processing (e.g. for enhancing low-frequency or filtering sidelobes). We stress that other inversion methods may account for the sidelobe effects, such as model based inversions and methods that take 4D time-shifts into account, however, they are more expensive and time-consuming, which may not be suitable for a quick 4DS diagnosis. One additional advantage of the IP over the amplitude domain is the vertical resolution enhancement that results in a better identification of additional features. These features may be critical to improve the reservoir models, for example, if the objective is an infill well, it is more crucial to have more precision in a certain region of interest, and increasing the seismic resolution becomes critical.

We therefore endorse the amplitude as the general diagnosis domain and the IP as a complementary domain where to make specific higher-resolution reservoir characterization. The cross-domain is a quick-access diagnosis alternative, but not recommended for more specific objectives such as history matching the models. In addition, the APPENDIX B – WELL RATES shows the well oil rate results for this set, indicating the quality of the models in terms of production matching for the ones filtered in each domain.

6 CONCLUSIONS

This work proposes a workflow to diagnose hundreds of simulations models according to their similarity with observed 4DS data. The workflow is applied in a real dataset from the Campos Basin (Brazil), with considerable 4DS signal complexity, ambiguity, and diversity in terms of shape, magnitude, and sizes.

We performed a study to define a PEM according to its calibration to well sonic and density logs. The overall match given by a Hertz-Mindlin model at the reservoir interval is good, which gives a good confidence on the fluid substitution studies and on other physical effects sensibility such as pore pressure variations. Besides, the addition of well history data and tracers improved the understanding on the 4D effects and their magnitudes. The initial interpretations were essential to divide the reservoir into regions and to define the best seismic attributes to capture the most important 4DS changes at the reservoir. As specific contributions from the thesis, we highlight the following:

- We developed an automatic tool to generate hundreds of synthetic seismic maps (forward seismic modeling) and to rapidly diagnose these large datasets according to the observed 4DS at the seismic amplitude domain, without the need to run a 4DS inversion.
- Selecting the best similarity indicator between the predicted and observed 4DS is a very complex task. The automatic tool generates hundreds of synthetic seismic maps and different shape and magnitude similarity metrics that can be adapted and applied to any 4D project.
- We defined the importance of region-by-region analysis, as global errors may mask local misfits that are important for further decision-making processes, such as an infill well. The selection of the model (or set of models) to be used for this purpose can be de-risked if one selects models with low regional misfits in the potential areas, rather than selecting the best model on average for the entire reservoir.
- The regional similarity metrics provide two pieces of information: if the 4D anomaly shape/magnitude inside each region are well matched and if they are laterally contained within these regions.
- For the shape metric, we applied a fast, reliable and unsupervised method that isolates noise from the 4D signal very well. The GMM parameters, once set, can be run successfully on other vintages and in other domains.

- We demonstrate the complementarity between the shape and the magnitude metrics. The methodology can be applied in every crucial step of a reservoir management framework:
    - to validate geological/simulation models;
    - to rank and to select the best models for production forecasting and the decision-making process;
    - to identify anomalies not predicted by the dynamic model;
    - for feedback on iterations of geomodeling; and
    - for analyzing just-acquired seismic monitors with regards to their simulated predictions.
- The outlier detection tool can be adapted for different applications. In this work, we used as a multi-objective criterion where the model must be simultaneously not contained in any outlier list to be accepted. In other applications, it can be used to discard models with high errors within certain regions (e.g. an infill well region).
- The amplitude domain is endorsed as the best diagnosis domain; however, we highlight the importance of the IP domain for higher-resolution reservoir characterization purposes, and the saturation domain for a quick-look diagnosis.

7 SUGGESTIONS FOR FUTURE WORK

We indicate the following areas as recommendations for a progression of this work:

- To address the limitation of constantly alternating between different softwares and the generation of intermediate data sets, we suggest the development of a single plugin handling different interfaces. This would expedite the whole process, optimizing the amount of generated data and efforts.
- Development of a practical methodology on combining metrics obtained from more than one monitor comparison at a time.
- Investigate the value of including elastic/AVO attributes in the workflow.
- For the saturation domain comparisons, we suggest weight adjustments for balancing the influence of different types of physical effects.
- Couple the proposed diagnosis within the data assimilation procedure.

8 REFERENCES

ALMEIDA, F.L.R., FORMENTIN, H. N., MASCHIO, C., SCHIOZER, D. J. Influence of additional objective functions on uncertainty reduction and history matching. In: EAGE CONFERENCE AND EXHIBITION, 80., 2018, Copenhagen. **Proceedings...** Copenhagen: OnePetro, 2018. Available at: https://doi.org/10.2118/190804-ms.

AMINI, H. **A pragmatic approach to simulator-to-seismic modelling for 4D seismic interpretation**. 2014. 270p. Thesis (Doctorate). Institute of Petroleum Engineering, Heriot-Watt University. Available at: https://hdl.handle.net/10399/2756.

AMINI, H., RODRIGUEZ, M., WILKINSON, D., MACBETH, C. A case study of effective metrics for history matching the 4D seismic data. In: EAGE CONFERENCE AND EXHIBITION, 81., 2019, London. **Proceedings...** Available at: https://doi.org/10.3997/2214-4609.201900948.

ASTIC, T.; HEAGY, L.J.; OLDENBURG, D.W. Petrophysically and geologically guided multi-physics inversion using a dynamic Gaussian mixture model. **Geophysical Journal International**, v.224, n.1, p.40-68, 2021. Available at: https://doi.org/10.1093/gji/ggaa378.

AVANSI, G. D.; MASCHIO, C.; SCHIOZER, D. J. Simultaneous History-Matching Approach by Use of Reservoir-Characterization and Reservoir-Simulation Studies**. SPE Reservoir Evaluation & Engineering**, [s. l.], v. 19, n. 04, p. 694–712, 2016. Available at: https://doi.org/10.2118/179740-PA

BATZLE, M.; ZHIJING, W. Seismic properties of pore fluids. **Geophysics**, v.57, n.11, p.1396-1408, 1992. Available at: https://doi.org/10.1190/1.1443207.

BUKSH, G.; FARMER, H. G.; GALARRAGA, M. A.; LYDON, M. T.; MAUTZ, W. A.; NORBERG, D. Life Of field seismic in the deepwater BC-10 phase 2 development, Brasil. In: OFFSHORE TECHNOLOGY CONFERENCE, 2015, Houston. **Offshore Technology Conference**. Houston: OnePetro, 2015. v.3, p.1792-1798. Available at: https://doi.org/10.4043/25803-ms.

CHANG, T.; CHEN, Y.; KUMAR, G.; NIETO, C.; BEAL, E. A conventional 4D and a snapshot 4D comparison in the Campos Basin. In: INTERNATIONAL CONGRESS OF THE BRAZILIAN GEOPHYSICAL SOCIETY, 16., 2019, Rio de Janeiro. **Proceedings...** Rio de Janeiro: SBGf, 2019. p.1-6. Available at: https://doi.org/10.22564/16cisbgf2019.009.

CHASSAGNE, R.; ARANHA, C. A pragmatic investigation of the objective function for subsurface data assimilation problem. **Operations Research Perspectives**, v.7, 100143, 2020. Available at: https://doi.org/10.1016/j.orp.2020.100143.

CHEN, Y.; FARMER, H. G.; LIU, Z.; LYDON, M.; WU, H. LoFS Processing for 4D Attributes at the BC10 Field – Offshore Brazil. In: EAGE WORKSHOP ON PERMANENT RESERVOIR MONITORING, 3., 2015, Oslo. **Proceedings...** Oslo: European Association of Geoscientists & Engineers, 2015. p.2014-2016. Available at: https://doi.org/10.3997/2214-4609.201411967.

CÔRTE, G.; DRAMSCH, J.; AMINI, H.; MACBETH, C. Deep neural network application for 4D seismic inversion to changes in pressure and saturation: Optimizing the use of synthetic training datasets, **Geophysical Prospecting**, v. 68, n. 7, p. 2164–2185, 2020. Available at: 10.1111/1365-2478.12982.

CRUZ, N. M.; CRUZ, J. M.; COSTA, M. M.; OLIVEIRA, L. B.; URASAKI, E.N.; BISPO, T. P.; JARDIM, M. S.; GROCHAU, M. H.; MAUL, A. **The Leading Edge**, 2021. Available at: https://doi.org/10.1190/tle40120886.1.

DAVOLIO, A. **Using reservoir simulation to constrain the estimation of dynamic properties from 4D seismic**. 2013. 122p. Thesis (Doctorate) - Mechanical Engineering Faculty and Geosciences Institute, University of Campinas, Campinas. Available at: https://www.unisim.cepetro.unicamp.br/publicacoes/Alessandra%20Davolio.pdf.

DAVOLIO, A.; SCHIOZER, D.J. Probabilistic seismic history matching using binary images. **Journal of Geophysics and Engineering**, v.15, n.1, p.261-274, 2018. Available at: https://doi.org/10.1088/1742-2140/aa99f4.

DERFOUL, R.; DA VEIGA, S.; GOUT, C.; GUYADER, C.; TILLIER, E. Image processing tools for better incorporation of 4D seismic data into reservoir models. **Journal of Computational and Applied Mathematics**, v.240, p.111-122, 2013. Available at: https://doi.org/10.1016/j.cam.2012.08.022.

DOVERA, L.; DELLA ROSSA, E. Multimodal ensemble Kalman filtering using Gaussian mixture models. **Computational Geosciences**, v.15, n.2, p.307-323, 2011. Available at: https://doi.org/10.1007/s10596-010-9205-3.

EBAID, H.; WANG, K.; SEIXAS, M.; KUMAR, G.; BREW, G.; MASCHIOTTA, T. Practical example of data integration in a PRM environment, BC-10, Brazil. In: EAGE WORKSHOP ON PRACTICAL RESERVOIR MONITORING, 1., 2017, Amsterdam. **Proceedings...** Amsterdam: European Association of Geoscientists & Engineers, 2017. p.71-76. Available at: https://doi.org/10.3997/2214-4609.201700019.

EMERICK, A.A. Analysis of the performance of ensemble-based assimilation of production and seismic data. **Journal of Petroleum Science and Engineering**, v.139, p.219-239, 2016. Available at: https://doi.org/10.1016/j.petrol.2016.01.029.

EMERICK, A.A.; DE MORAES, R.J.; RODRIGUES, J.R.P. Calculating seismic attributes within a reservoir flow simulator. In: LATIN AMERICAN & CARIBBEAN PETROLEUM ENGINEERING CONFERENCE, 2007, Buenos Aires. **Proceedings...** Buenos Aires: OnePetro, 2007. v.1, p.194-205. Available at: https://doi.org/10.2523/107001-ms.

EMERICK, A.A.; REYNOLDS, A.C. Ensemble smoother with multiple data assimilation. **Computers and Geosciences**, v.55, p.3-15, 2013. Available at: https://doi.org/10.1016/j.cageo.2012.03.011.

FAHIMUDDIN, A.; AANONSEN, S. I.; SKJERVHEIM, J.-A. Ensemble Based 4D Seismic History Matching: Integration of Different Levels and Types of Seismic Data, 2010. In: SPE EUROPEC/EAGE Annual Conference and Exhibition, 2010, Barcelona, Spain, **Proceedings...** Barcelona: SPE, 2010. Available at: https://doi.org/10.2118/131453-MS.

FJELDSTAD, T.; AVSETH, P.; OMRE, H. A one-step Bayesian inversion framework for 3D reservoir characterization based on a Gaussian mixture model: A Norwegian Sea demonstration. **Geophysics**, v.86, n.2, p.R221-R236, 2021. Available at: https://doi.org/10.1190/geo2020-0094.1.

FORMENTIN, H.N.; ALMEIDA, F.L.R.; AVANSI, G.D.; MASCHIO, C.; SCHIOZER, D.J.; CAIADO, C.; VERNON, I.; GOLDSTEIN, M. Gaining more understanding about reservoir behavior through assimilation of breakthrough time and productivity deviation in the history matching process. **Journal of Petroleum Science and Engineering**, v.173, p.1080-1096, 2019. Available at: https://doi.org/10.1016/j.petrol.2018.10.045.

GASSMANN, F. Elastic waves through a packing of spheres. **Geophysics**, v.16, n.4, p.673-685, 1951. Available at: https://doi.org/10.1190/1.1437718.

GOSSELIN, O.; AANONSEN, S. I.; AAVATSMARK, I.; COMINELLI, A.; GONARD, R.; KOLASINSKI, M.; FERDINANDI, F.; KOVACIC, L.; NEYLON, K. History Matching Using Time-lapse Seismic (HUTS). In: SPE ANNUAL TECHNICAL CONFERENCE AND EXHIBITION, 2003, Denver. **Proceedings...** Denver: OnePetro, 2003. Available at: https://doi.org/10.2118/84464-MS.

JANSEN, J. D.; BROUWER, D. R.; NÆVDAL, G.; KRUIJSDIJK, C. P. J. W. Closed-loop reservoir management. **First Break**, v.23, p.43-48, 2005.

JANSEN, J. D.; BROUWER, R.; DOUMA, S.G. Closed Loop Reservoir Management. In: SPE RESERVOIR SIMULATION SYMPOSIUM, 2009, The Woodlands. **Proceedings...** The Woodlands: OnePetro, 2009. Available at: https://doi.org/10.2118/119098-MS.

KRAGH, E.; CHRISTIE, P. Seismic repeatability, normalized rms, and predictability. **The Leading Edge**, v.21, n.7, p.640-647, 2002. Available at: https://doi.org/10.1190/1.1497316.

LEEUWENBURGH, O.; BROUWER, J.; TRANI, M. Ensemble-based conditioning of reservoir models to seismic data. **Computational Geosciences**, v.15, n.2, p.359-378, 2011. Available at: https://doi.org/10.1007/s10596-010-9209-z.

LIU, M.; GRANA, D. Time-lapse seismic history matching with an iterative ensemble smoother and deep convolutional autoencoder. **Geophysics**, v.85, n.1, p.M15-M31, 2020. Available at: https://doi.org/10.1190/geo2019-0019.1.

LORENTZEN, R.; BHAKTA, T.; GRANA, D.; LUO, X.; VALESTRAND, R.; NÆVDAL, G.; History matching of real production and seismic data in the Norne field. In: EUROPEAN CONFERENCE ON THE MATHEMATICS OF OIL RECOVERY, 16., 2018, Barcelona. **Proceedings...** Barcelona: European Association of Geoscientists & Engineers, 2018. p.1-16. Available at: https://doi.org/10.3997/2214-4609.201802231.

LUO, X.; BHAKTA, T.; JAKOBSEN, M.; NÆVDAL, G. An ensemble 4D seismic history matching framework with sparse representation based on wavelet multiresolution analysis. In: SPE BERGEN ONE DAY SEMINAR, 2016, Bergen. **Proceedings...** Bergen: OnePetro, 2016. p.985-1010. Available at: https://doi.org/10.2118/180025-ms.

LUO, X.; BHAKTA, T.; JAKOBSEN, M.; NÆVDAL, G. Efficient big data assimilation through sparse representation: A 3D benchmark case study in petroleum engineering. **PLoS ONE**, v.13, n.7, e0198586, 2018. Available at: https://doi.org/10.1371/journal.pone.0198586.

MALEKI, M.; CIRNE, M.; SCHIOZER, D.; DAVOLIO, A.; ROCHA, A. A machine-learning framework to estimate saturation changes from 4D seismic data using reservoir models, **Geophysical Prospecting**, v. 70, 2022. DOI: 10.1111/1365-2478.13249.

MALEKI, M.; DANAEI, S.; MESQUITA DA SILVA, F. B.; SCHIOZER, D.; DAVOLIO, A. Stepwise uncertainty reduction in time-lapse seismic interpretation using multi-attribute analysis. **Petroleum Geoscience**, v.27, n.3, petgeo2020-087, 2021. Available at: https://doi.org/10.1144/petgeo2020-087.

MASCHIO, C.; AVANSI, G. D.; MESQUITA DA SILVA, F. B.; SCHIOZER, D. J. Data assimilation for uncertainty reduction using different fidelity numerical models. **Journal of**

Petroleum Science and Engineering, v.209, 109851, 2022. Available at: https://doi.org/10.1016/j.petrol.2021.109851.

MAVKO, G.; MUKERJI, T.; DVORKIN, J. **The Rock Physics Handbook**. Cambridge: Cambridge University Press, 1998.

MAVKO, G.; MUKERJI, T.; DVORKIN, J. **Rock Physics Handbook: tools for seismic analysis in porous media**. 2. ed. Cambridge: Cambridge University Press, 2009. Available at: https://doi.org/http://dx.doi.org/10.1017/CBO9780511626753.

OBIDEGWU, D.; CHASSAGNE, R.; MACBETH, C. Seismic assisted history matching using binary image matching. In: EUROPEC 2015, 2015, Madrid. **Proceedings...** Madrid: OnePetro, 2015. p.1119-1140. Available at: https://doi.org/10.2118/174310-ms.

ØDEGAARD, E.; AVSETH, P. Well log and seismic data analysis using rock physics templates. **First Break**, v.22, n.10, p.37-43, 2004. Available at: https://doi.org/10.3997/1365-2397.2004017.

OLIVER, D. S.; ALFONZO, M. A. Seismic data assimilation with an imperfect model. In: EUROPEAN CONFERENCE ON THE MATHEMATICS OF OIL RECOVERY, 16., 2018, Barcelona. **Proceedings...** Barcelona: European Association of Geoscientists and Engineers, 2018. p.1-23. Available at: https://doi.org/10.3997/2214-4609.201802283.

ROGGERO, F.; DING, D. Y.; BERTHET, P.; LERAT, O.; CAP, J.; SCHREIBER, P. E. Matching of Production History and 4D Seismic Data--Application to the Girassol Field, Offshore Angola. In: SPE ANNUAL TECHNICAL CONFERENCE AND EXHIBITION, 2007, Anaheim. **Proceedings...** Anaheim: OnePetro, 2007. Available at: https://doi.org/10.2118/109929-MS.

ROLLMANN, K. **Techniques for Comparing 4D Seismic Data in Oil Reservoir Fields**. 2020. 57p. Dissertation (Master’s Degree) - Institute of Computing, University of Campinas, Campinas. Available at: https://www.unisim.cepetro.unicamp.br/publicacoes/KLAUS_ROLLMANN.pdf.

ROSA, D. R.; SCHIOZER, D. J.; DAVOLIO, A. Enhancing vertical resolution with 4D seismic inversion, **Journal of Petroleum Science and Engineering**, v. 212, n. November, 2022. DOI: 10.1016/j.petrol.2022.110291.

SANTOS, J.M.C.; SCHIOZER, D.J.; DAVOLIO, A. Multi attribute approach for quantifying competing time lapse effects and implications for similarity indicators in data assimilation. In:

SPE ANNUAL TECHNICAL CONFERENCE AND EXHIBITION, 2020. **Proceedings...** [*S. l.*]: OnePetro, 2020. Available at: https://doi.org/10.2118/201426-ms.

SANTOS, J.M.C.; ROSA, D. R.; SCHIOZER, D.J.; DAVOLIO, A. Fast diagnosis of reservoir simulation models based on 4D seismic similarity indicators. **Journal of Petroleum Science and Engineering**, v.210, 110083, 2022. Available at: https://doi.org/10.1016/j.petrol.2021.110083.

SCHIOZER, D.J.; AVANSI, G.D.; DOS SANTOS, A.A.S. Risk quantification combining geostatistical realizations and discretized Latin Hypercube. **Journal of the Brazilian Society of Mechanical Sciences and Engineering**, v.39, n.2, p.575-587, 2017. Available at: https://doi.org/10.1007/s40430-016-0576-9.

SCHIOZER, D. J.; DE SOUZA DOS SANTOS, A. A.; SANTOS, S. M. G.; HOHENDORFF FILHO, J. C. Model-based decision analysis applied to petroleum field development and management. **Oil & Gas Science and Technology**, v.74, n.46, 2019. Available at: https://doi.org/10.2516/ogst/2019019.

SEYDOUX, L.; BALESTRIERO, R.; POLI, P.; HOOP, M.; CAMPILLO, M.; BARANIUK, R. Clustering earthquake signals and background noises in continuous seismic data with unsupervised deep learning. **Nature Communications**, v.11, n.3972, p.1-12, 2020. Available at: https://doi.org/10.1038/s41467-020-17841-x.

SILVA NETO, G.M.; DAVOLIO, A.; SCHIOZER, D.J. Assimilating time-lapse seismic data in the presence of significant spatially correlated model errors. **Journal of Petroleum Science and Engineering**, v.207, p.109-127, 2021. Available at: https://doi.org/10.1016/J.PETROL.2021.109127.

SKJERVHEIM, J.A.; EVENSEN, G.; AANONSEN, S. I.; RUUD, B. O.; JOHANSEN, T. A. Incorporating 4D seismic data in reservoir simulation models using ensemble Kalman filter. **SPE Journal**, v.12, n.3, p.282-292, 2007. Available at: https://doi.org/10.2118/95789-PA.

SOARES, R.V.; LUO, X.; EVENSEN, G.; BHAKTA, T. 4D seismic history matching: Assessing the use of a dictionary learning based sparse representation method. **Journal of Petroleum Science and Engineering**, v.195, 107763, 2020. Available at: https://doi.org/10.1016/j.petrol.2020.107763.

SORIANO-VARGAS, A.; ROLLMANN, K.; ALMEIDA, F.; DAVOLIO, A.; HAMANN, B.; SCHIOZER, D. J.; ROCHA, A. A synthetic case study of measuring the misfit between 4D seismic data and numerical reservoir simulation models through the Momenta Tree. **Computers and Geosciences**, v.145, 104617, 2020. Available at: https://doi.org/10.1016/j.cageo.2020.104617.

SOUZA, R.; LUMLEY, D.; SHRAGGE, J.; DAVOLIO, A.; SCHIOZER, D. J. Analysis of time-lapse seismic and production data for reservoir model classification and assessment. **Journal of Geophysics and Engineering**, v.15, n.4, p.1561-1587, 2018. Available at: https://doi.org/10.1088/1742-2140/aab287.

STAMMEIJER, J.G.F.; HATCHELL, P.J. Standards in 4D feasibility and interpretation. **Leading Edge**, v.33, n.2, p.134-140, 2014. Available at: https://doi.org/10.1190/tle33020134.1.

TILLIER, E.; DA VEIGA, S.; DERFOUL, R. Appropriate formulation of the objective function for the history matching of seismic attributes. **Computers and Geosciences**, v.51, p.64-73, 2013. Available at: https://doi.org/10.1016/j.cageo.2012.07.031.

TRANI, M.; WOJNAR, K.; MONCORGE, A.; PHILIPPE, B. Ensemble-based assisted history matching using 4d seismic fluid front parameterization. SPE Middle East Oil and Gas Show and Conference, MEOS, **Proceedings...** [s. l.], v. 2017-March, n. 1, p. 640–652, 2017. Available at: https://doi.org/10.2118/183901-ms.

WALLET, B.C.; HARDISTY, R. Unsupervised seismic facies using Gaussian mixture models. **Interpretation**, v.7, n.3, p.93-111, 2019. Available at: https://doi.org/10.1190/int-2018-0119.1.

WANG, K.; DUNN, S.; WARD, J.; HATCHELL, P. Direct measurement of water velocity and tidal variations for improved 4D repeatability in marine seismic acquisition. **First Break**, v.33, n.5, p.73-79, 2015. Available at: https://library.seg.org/doi/10.1190/segam2012-0806.1.

XUE, Y.; ARAUJO, M.; WANG, K.; LOPEZ, J.; KUMAR, G.; BREW, G. Machine learning to reduce cycle time for time-lapse seismic data assimilation into reservoir management, 81st EAGE Conference and Exhibition 2019, n. June 2019, p. 2–6, 2019. **Proceedings...** Available at: https://doi.org/10.3997/2214-4609.201901217.

WINTER, W.R.; JAHNERT, R.J.; FRANÇA, A.B. Bacia de Campos. **Boletim de Geociências da Petrobrás**, v.15, n.2, p.511-529, 2007.

ZHANG, Y.; LEEUWENBURGH, O. Image-oriented distance parameterization for ensemble-based seismic history matching. **Computational Geosciences**, v.21, n.4, p.713-731, 2017. Available at: https://doi.org/10.1007/s10596-017-9652-1.

ZHAO, Y.; LI, G.; REYNOLDS, A.C. Characterization of the measurement error in time-lapse seismic data and production data with an EM algorithm. **Oil & Gas Science and Technology**, v.62, n.2, p.181-193, 2007. Available at: https://doi.org/10.2516/ogst:2007016.

APPENDIX A – OTHER MONITORS' COMPARISONS

The thesis shows the applications and discussions on monitors 3 and monitor 5. This appendix shows the workflow results on the other different monitors to demonstrate their applicability on different noise and signal magnitudes.

Figure 48 a, d, g, j and m show the $dRMS_{obs}$ for monitors 1 to 5 respectively for comparison. The second and third columns in Figure 48 exhibit, respectively, the shape metric ternary map and their Gaussian fits on their $dRMS_{obs}$distribution. We note the monitors 2 and 3 show similar overall 4D anomalies distribution.

The monitor 1, being acquired just a few months after the baseline, has a lower 4D signal magnitude. In this case, the shape metric may be affected because of the narrow and symmetric $dRMS$ distribution observed in Figure 48 c, where the hardening (positive) anomalies are very subtle. Figure 49 shows the best models selected from set S4D (before 4DS data assimilation) using the shape metric. Their match is poor as compared to the $dRMS_{obs}$, where all the models predict stronger and larger 4D responses than observed, even for the top ranked examples. The diagnosis suggests this set of models does not honor the early simulated time-steps, especially in the central area (gas anomaly). The examples also demonstrate the workflow runs as expected, where subtle 4D anomalies are clustered as 4D hardening and softening.

Figure 50 a and b show, respectively, the best and worst models selected from set S4D for monitor 1 using the magnitude metric. We also note a general mismatch with $dRMS_{obs}$ for this monitor even for the top ranked models. In addition, the top ranked models for the magnitude and the shape metric display a different overall response, especially in the central region, except for the model 24. In fact, the top ranked models from the magnitude metric do have low shape error values as well, but they have not been ranked at the top for the shape metric because they are larger and mispositioned as compared to the observed map.

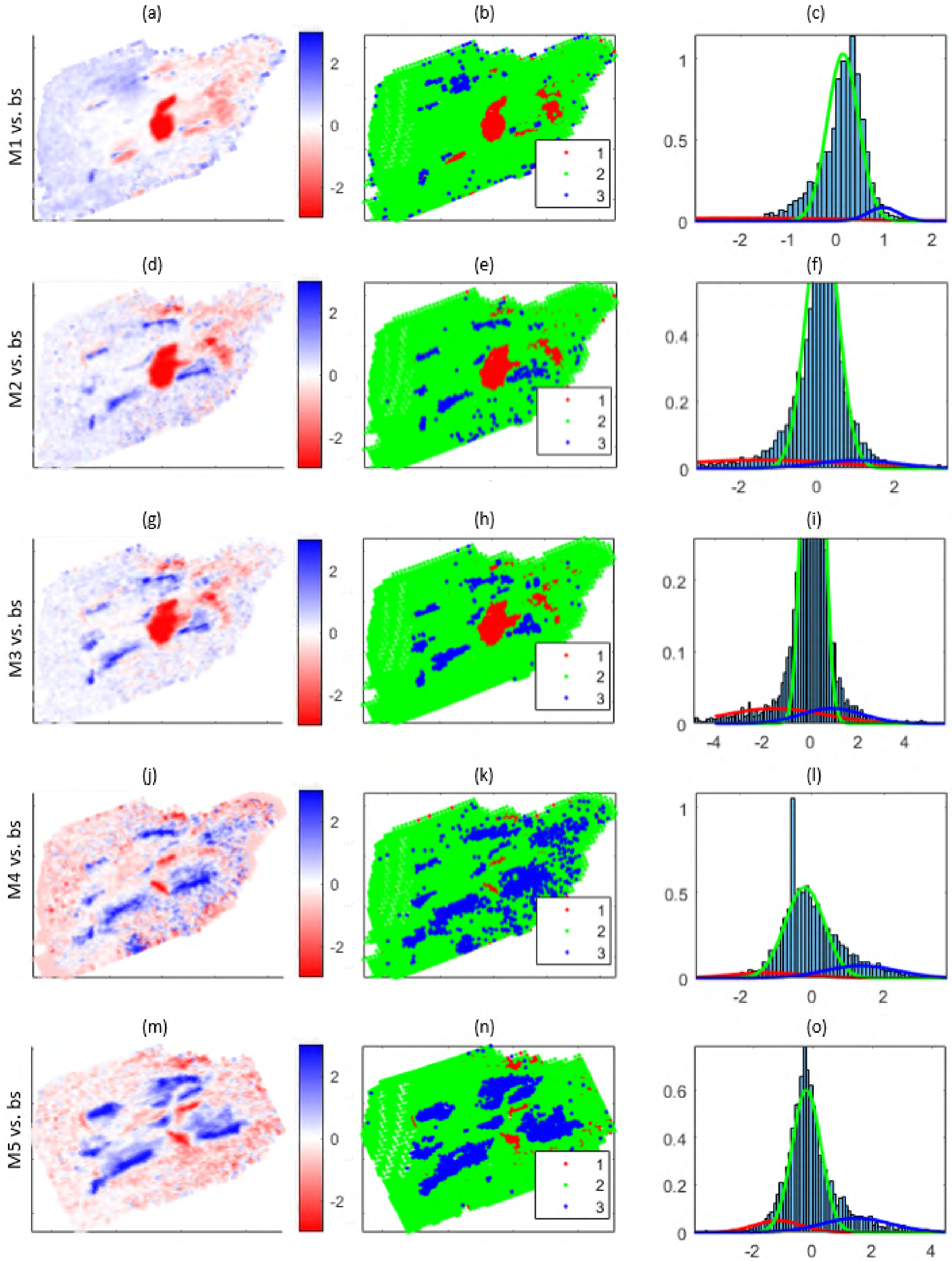

Figure 48 - Workflow application on other monitors – (a) to (c) monitor 1 vs. base, (d) to (f) monitor 2 vs. base, (g) to (i) monitor 3 vs. base, (j) to (l) monitor 4 vs. baseline and (m) to (o) monitor 5 vs. baseline. The first column shows the $dRMS_{obs}$, the second shows their ternarized maps, and the third shows their $dRMS$ distribution in the histogram with their resulting Gaussian models.

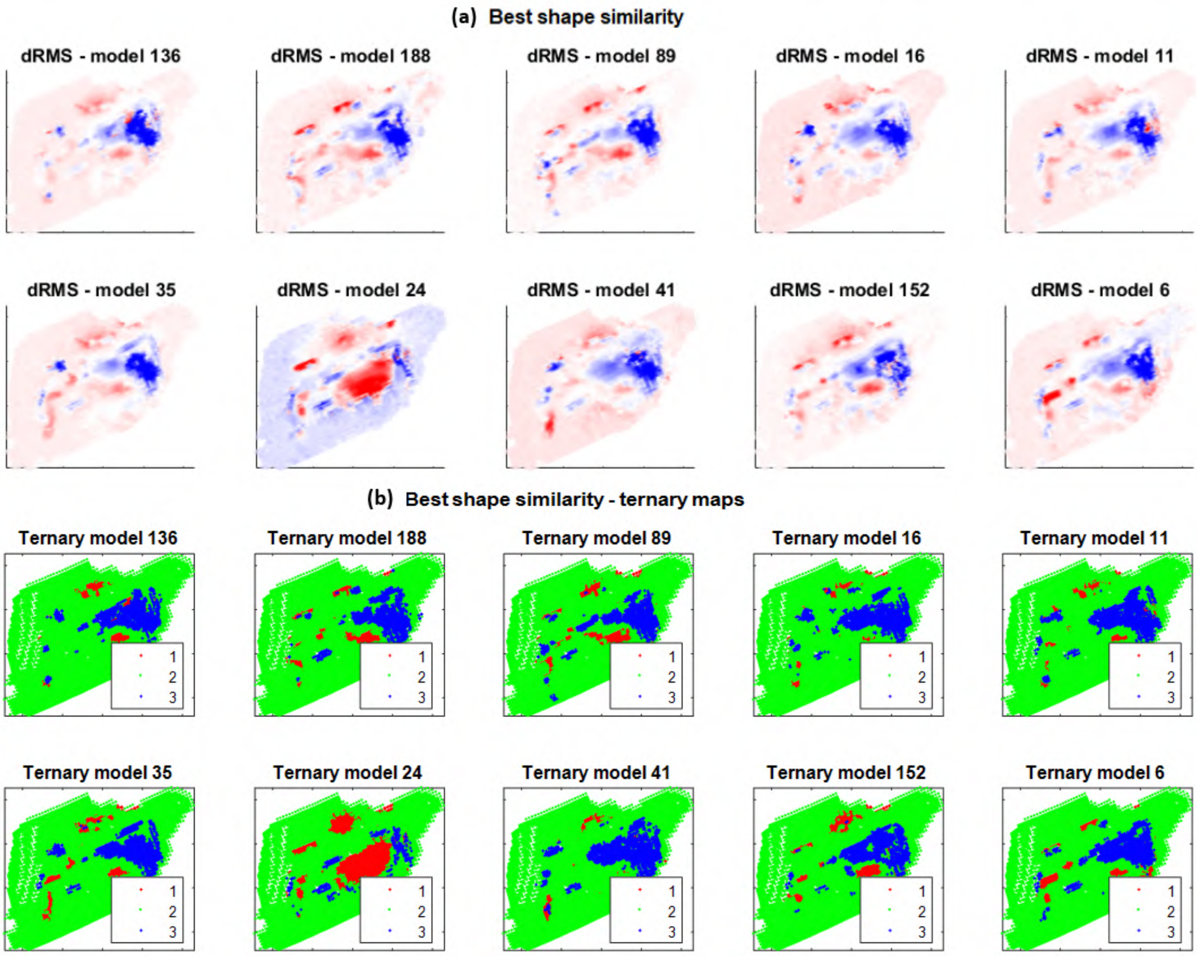

Figure 49 - Best models from set S4D, selected using the shape metric at the full reservoir: monitor 1 vs. baseline $dRMS$ maps (a) and their respective ternary maps (b).

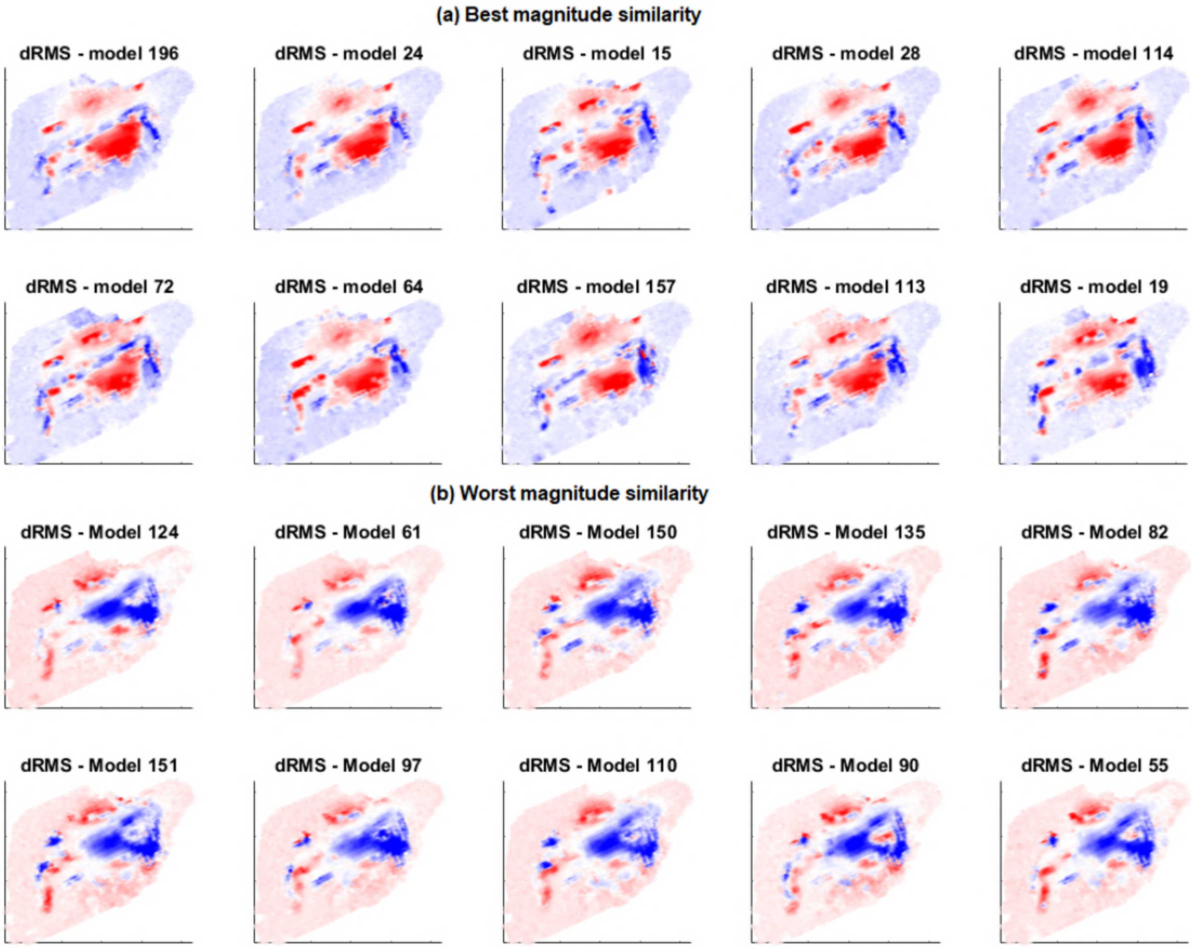

Figure 50 - Best (a) and worst (b) models from set S4D, selected using the magnitude metric at the full reservoir: monitor 1 vs. baseline $dRMS$ maps.

As discussed in section 5.1, monitor 4 has lower repeatability due to its different acquisition configuration, which imprints in the 4D attributes. These differences may affect both comparison metrics. The magnitude metric may perform comparisons between undesired noise from the observed maps and signal (or absence of signal) from the modeled maps. As the noise is not consistent throughout the entire survey, it cannot be reproduced to the models, and specific regions may be more affected. The regional diagnosis is, therefore, especially important for this matter. The shape metric may be affected by clustering high intensity noise into a signal cluster. The results from Figure 48 k and l, however, show their cluster found a reasonable compromise between clustering noise and signal. The overall diagnosis on the south and northeast regions, however, must be looked at carefully and used in a more qualitatively manner. As the survey was an “opportunity monitor”, it was not expected to be quantitatively assimilated in the reservoir models the same way as the other monitors regardless. Figure 51 show the magnitude metric works as expected even with the noise presence. Figure 52 shows worst ranked models by the shape metric which, similarly to what occurred to the monitor 1, ranked different models than the magnitude metric (Figure 51 b), corroborating the metrics complementarity.

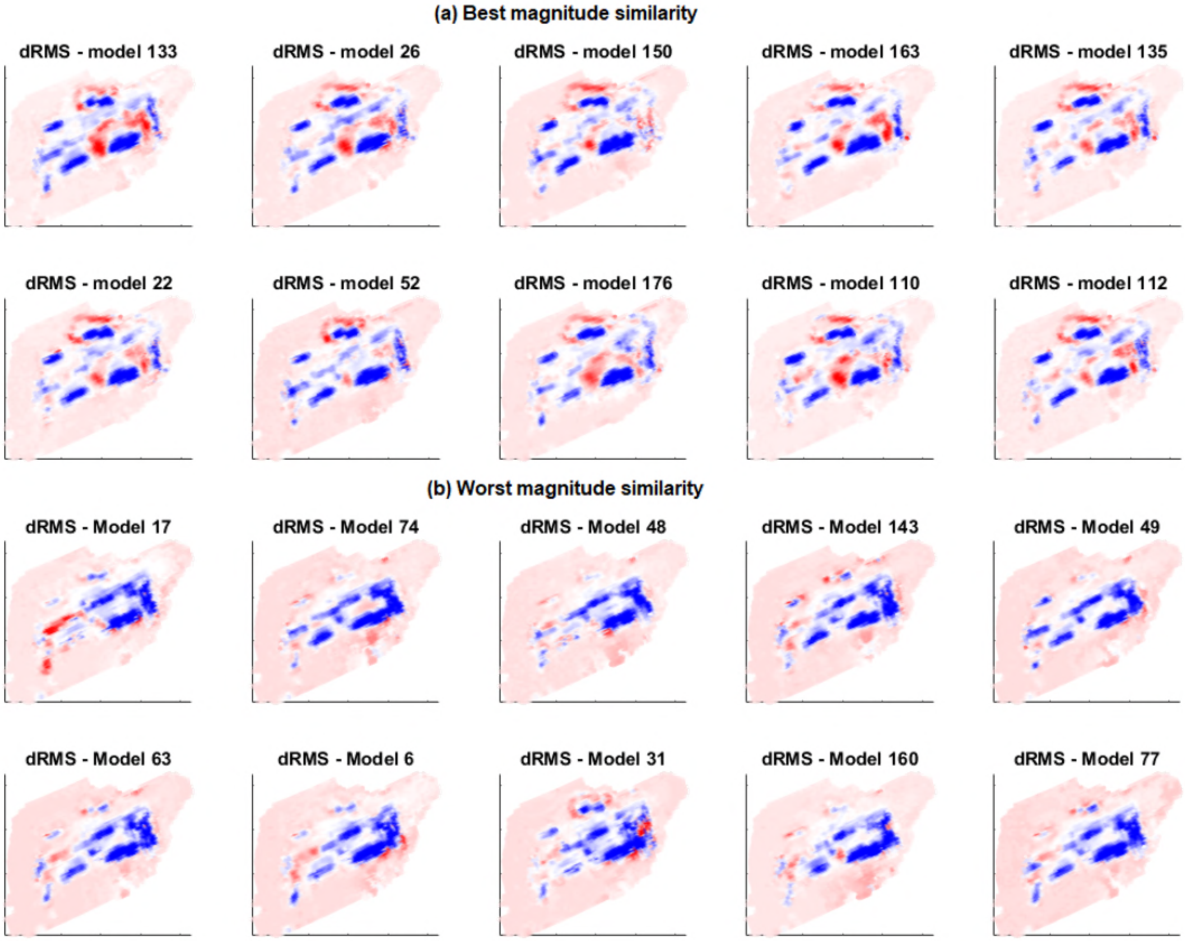

Figure 51 - Best (a) and worst (b) models from set S4D, selected using the magnitude metric at the full reservoir: monitor 4 vs. baseline $dRMS$ maps.

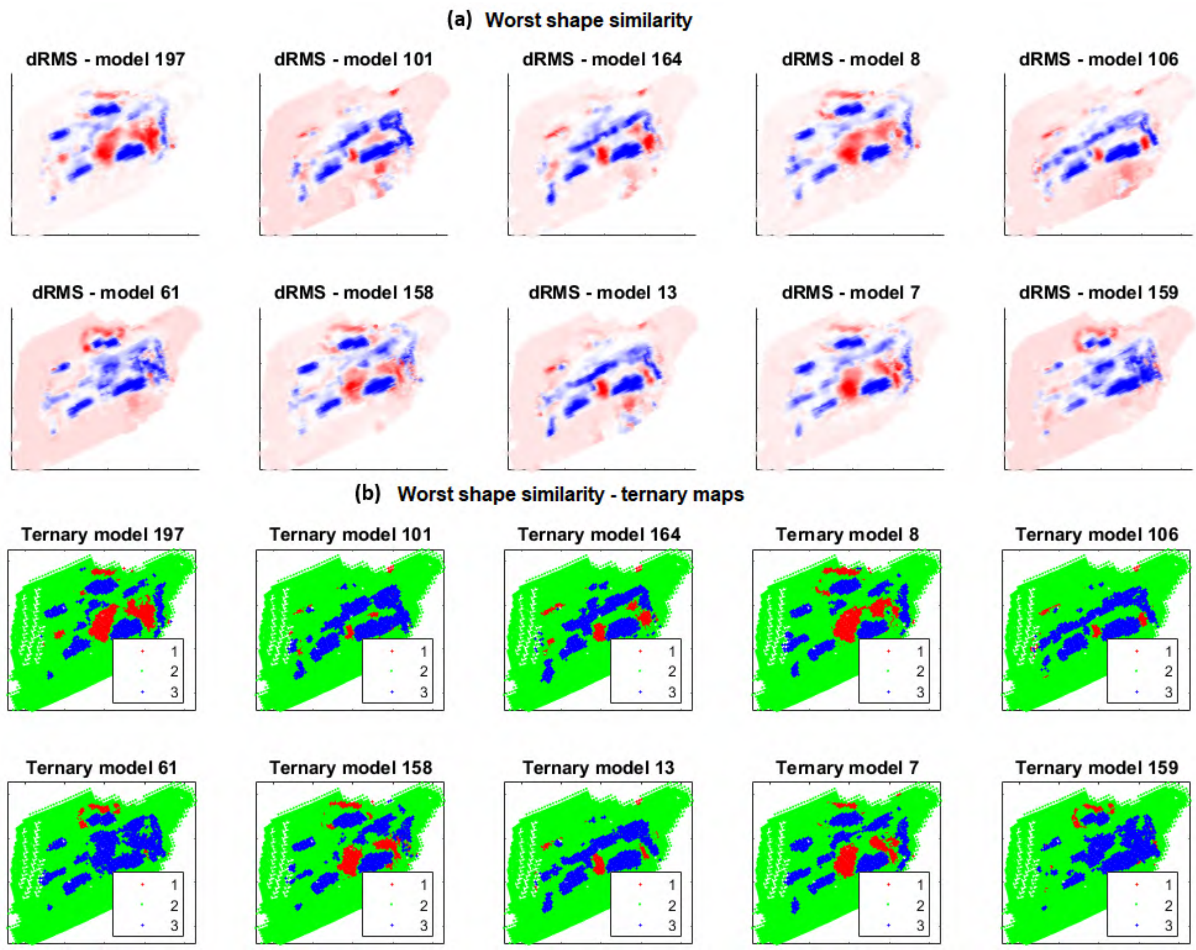

Figure 52 - Worst $dRMS$ (a) and ternary maps (b) - models from set S4D, selected using the shape metric at the full reservoir, monitor 4 vs. baseline.

Figure 53 and Figure 54 show the magnitude and shape errors measured in each region, comparing all monitors before (set S4D in blue) and after (set S4D_post_WS in black) data assimilation. Monitor 3 was used for assimilation, and therefore its error decrease after assimilation is more consistent throughout the regions, as compared to the other monitors. Regardless, the posterior exhibits lower errors in most monitors, with few exceptions such as regions P8, P9 and I5 from monitor 1 and P5 from monitor 4. The behavior of monitor 2 errors is very similar to monitor 3, which is expected due to their 4D signal similarities. As observed in the previous examples from Figure 49, the models do not honor the observed dynamic behavior at monitor 1, where in most regions presents the largest errors, for both metrics, even after data assimilation. We also highlight the errors measured at monitor 4 are in the same order as the other monitors, even though this survey was not recommended for quantitative purposes due to poorer repeatability/higher noise, suggesting the noise has low impact in the diagnosis.

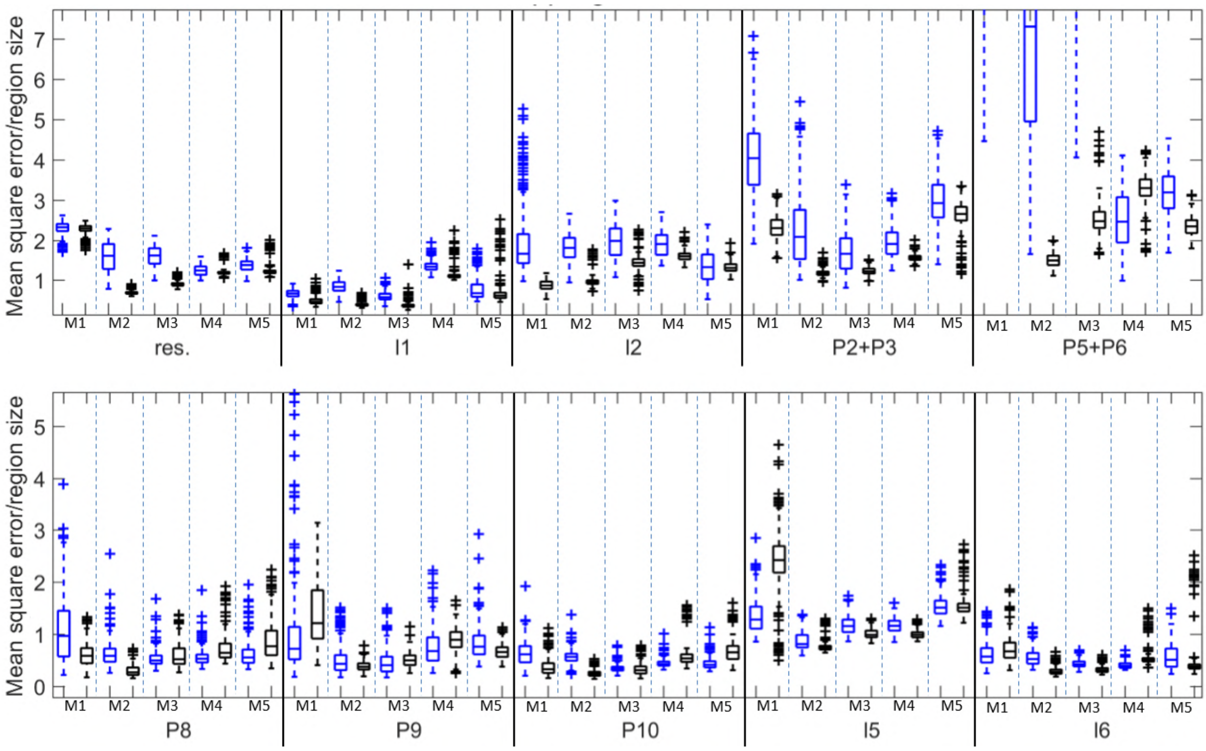

Figure 53 - Magnitude error by region - Set S4D (blue) and set S4D_post_WS (black) measured for all monitors.

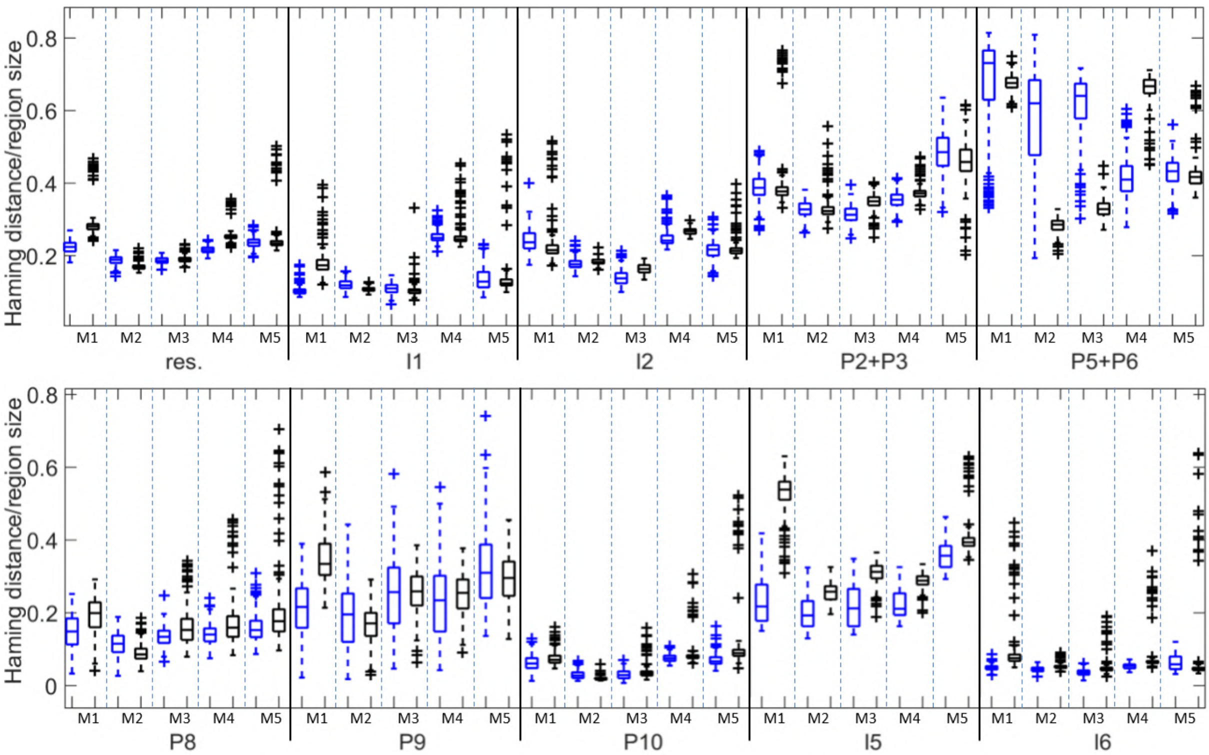

Figure 54 - Shape error by region - Set S4D (blue) and set S4D_post_WS (black) measured for all monitors.

APPENDIX B – WELL RATES

This appendix shows a discussion about the quality of excluded models from the 4DS analysis in terms of well production data match.

Figure 55 shows the producer wells' oil rates for the set S4D_post_WS (solid lines) with their historical production data (black dots). As this is a set after data assimilation, we can note the models' behavior are predominantly collapsed towards the historical data, indicating an overall good history match. The period around the 4DS monitors 2, 3 and 4 presents most variability, particularly at the wells P3 and P6. In these higher variability regions, we can note several outliers (high error) models selected by the 4DS metrics in the amplitude domain (green solid lines) and by all the domains simultaneously (pink lines) which are also deviated from the history. Regarding the models in blue, as they have been excluded using error metrics from dSw maps that presented most errors in the P2 and P10 regions, their production rate mismatch is more visible in these two wells.

Figure 56 and Figure 57 show the wells P3 and P6 respectively, with the models excluded using each domain in separate graphs. We can note in both wells the models excluded using the amplitude domain present most deviation from the historical points (green lines from Figure 56 a and Figure 57 a). For the other domains, however, the correlation between the high error models identified in the 4DS domains and the well domain is not clear. These results demonstrate high error models identified using the 4DS metrics that would not be detected using the conventionally used well historical data, which further demonstrates the complementariness of the proposed 4DS metrics for further decision making.

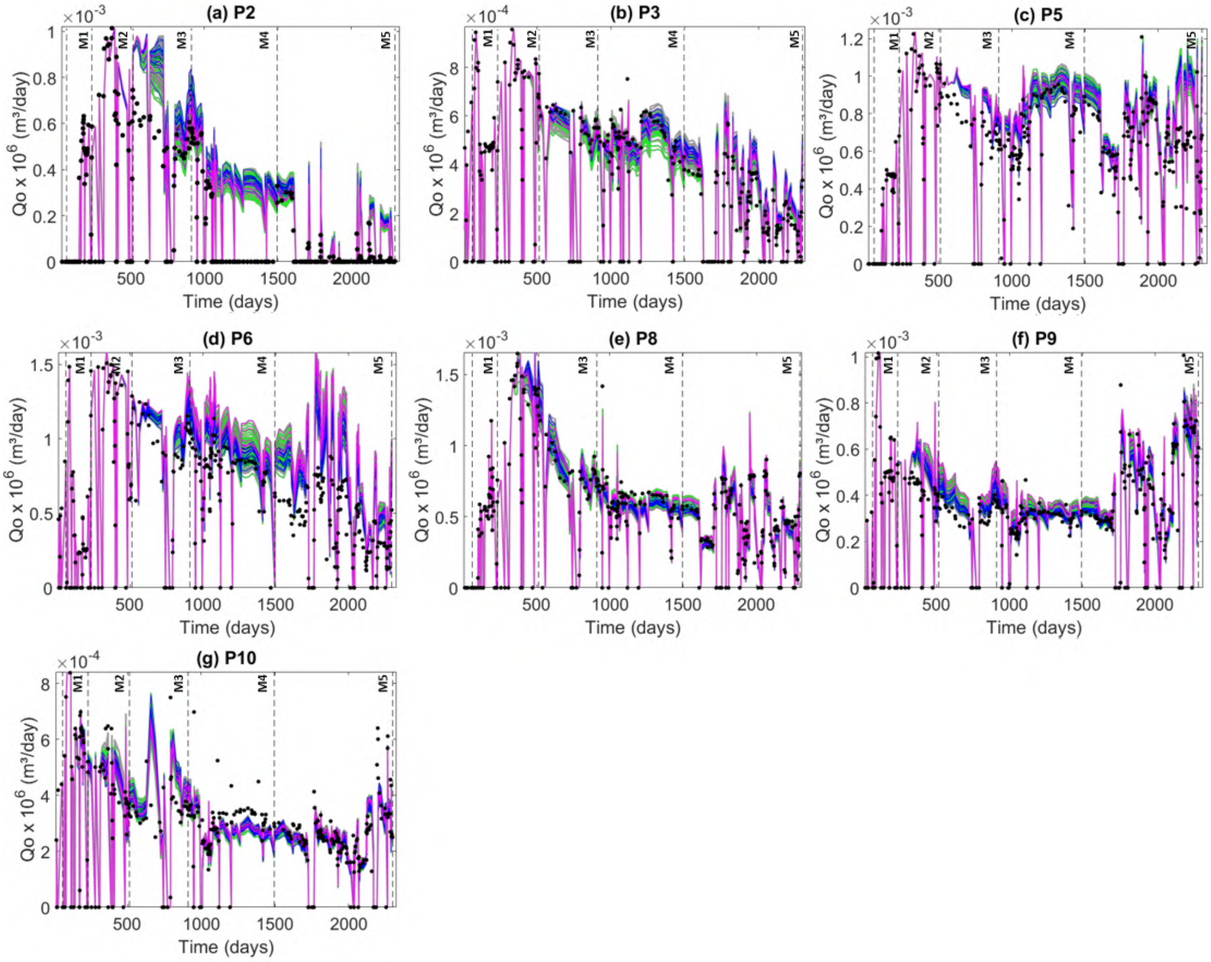

Figure 55 - Oil rates for each well: historic (black dots) and simulated (solid lines). The models highlighted in green are the ones excluded at the amplitude domain, in black, at the IP domain, in blue, at the dSw domain and magenta, using all domains simultaneously. The grey lines are the remaining (good) models. The dashed lines indicate the 4DS monitor dates.

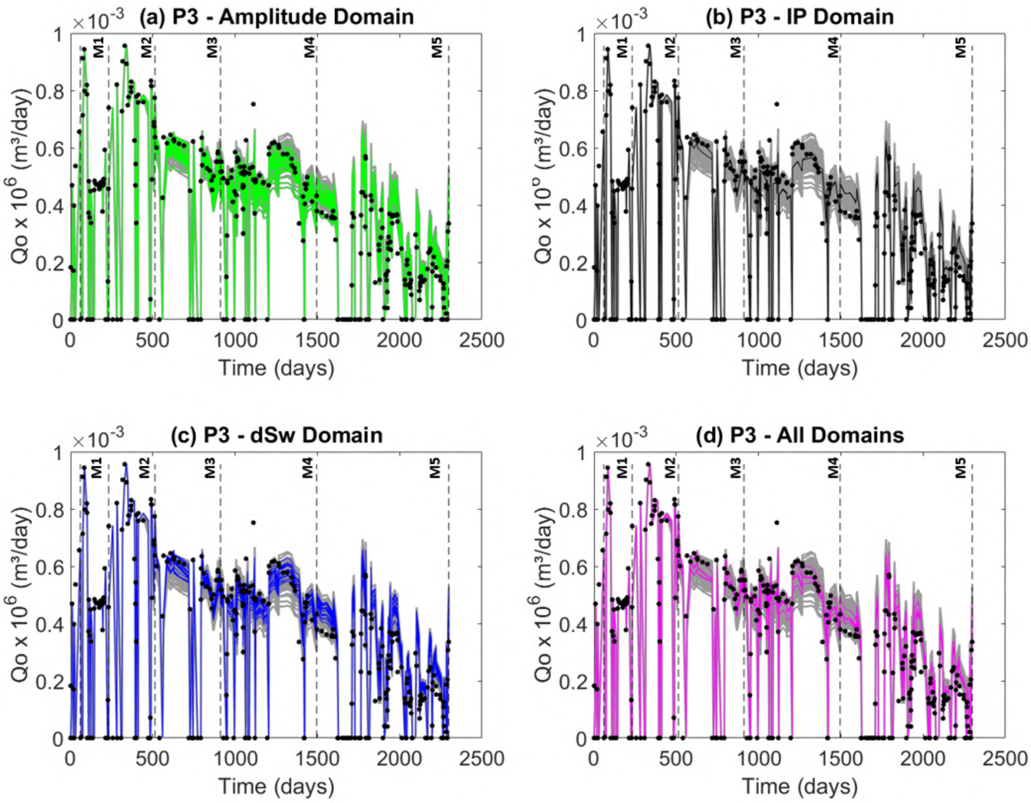

Figure 56 - Oil rates for well P3: historic (black dots) and simulated (solid lines). The graphs highlight separately the models excluded at the amplitude domain (a, in green), at the IP domain (b, in black), at the dSw domain (c, in blue) and using all domains simultaneously (d, in pink). The grey lines are the remaining (good) models. The dashed lines indicate the 4DS monitor dates.

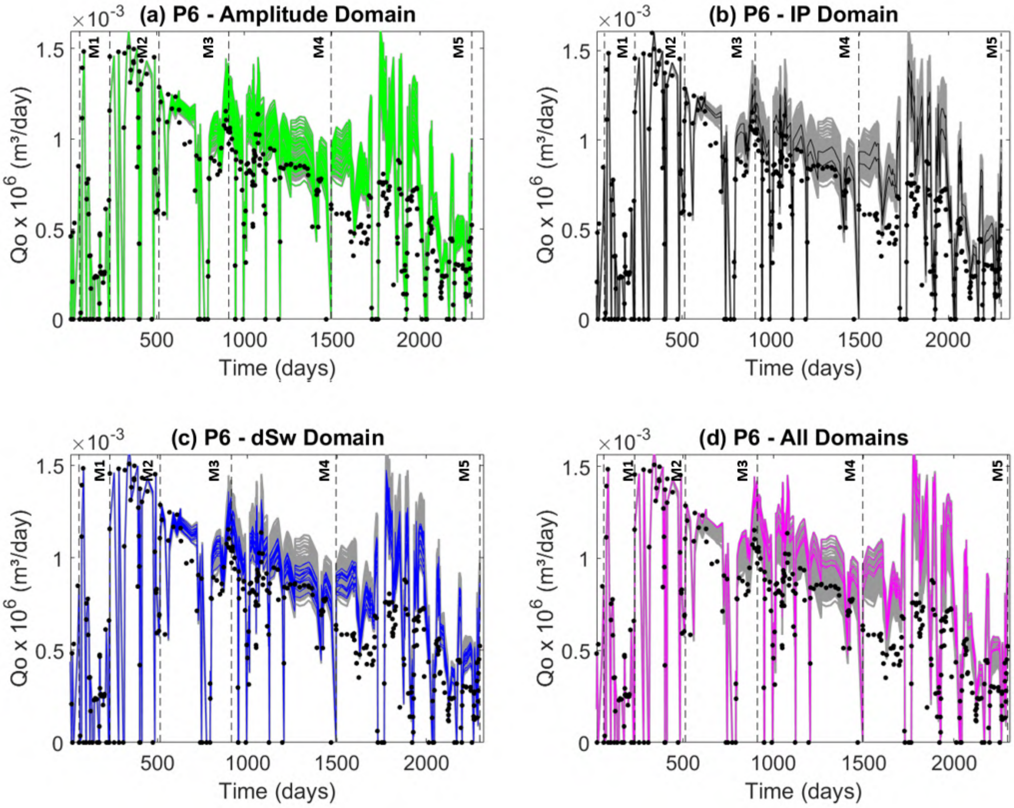

Figure 57 - Oil rates for well P10: historic (black dots) and simulated (solid lines). The graphs highlight separately the models excluded at the amplitude domain (a, in green), at the IP domain (b, in black), at the dSw domain (c, in blue) and using all domains simultaneously (d, in pink). The grey lines are the remaining (good) models. The dashed lines indicate the 4DS monitor dates.

APPENDIX C – ARTICLE 1

Society of Petroleum Engineers

SPE-201426-MS

Multi Attribute Approach for Quantifying Competing Time Lapse Effects and Implications for Similarity Indicators in Data Assimilation

Juliana Maia Carvalho Santos, Denis José Schiozer, and Alessandra Davolio, UNICAMP University of Campinas

This paper was prepared for presentation at the SPE Annual Technical Conference & Exhibition originally scheduled to be held in Denver, Colorado, USA, 5 – 7 October 2020. Due to COVID-19 the physical event was postponed until 26 – 29 October 2020 and was changed to a virtual event. The official proceedings were published online on 21 October 2020.

Abstract

This study aims to reduce uncertainties related to non-uniqueness in the interpretation of competing 4D effects and their impact to the interpretations and data assimilation into reservoir models. The study is based on synthetic and observed 4D seismic data, tracers, laboratory measurements, production and geophysical well log data. The methodology involves: (1) building and calibrating a petro-elastic model; (2) forward modeling of each separate physical effect such as saturation, pressure, salinity and noise; (3) combining the effects according to simulated production scenarios; and (4) correlating the modeled with observed 4D seismic data. We generate synthetic logs and seismic traces to quantify the time-lapse observations and to analyze how the combination of effects may affect the seismic character.

This work demonstrates a major impact of competing 4D effects in the number and types of true possible interpretations. Yet, estimating their influence on the magnitude and polarity of 4D signal is still achievable. We show application examples from a Brazilian turbidite reservoir, in a setting where a combination of 4D effects occur simultaneously and the confidence level on the 4D interpretations is high due to good quality and frequent seismic data from a permanent reservoir monitoring system.

In the example presented, a scenario where only water saturation effects occurs (e.g. aquifer water invading oil zone), 12 to 16% P-impedance (IP) increase (hardening effect) is expected. However, according to salinity measurements and tracers, injected sea water with lower salinity than the formation water decreases the hardening effect towards 8 to 10% in IP change. Having identified the impact of salinity changes in the 4D effects, an approach to include such changes in the petro-elastic model is proposed to generate 4D attributes that reproduce this interaction of effects. The outcome is a better match between modeled and observed 4D attributes, as compared to modeled attributes from a conventional petro-elastic model that considers salinity as constant. Additionally, combining these effects with gas going out from solution due to depletion below bubble point, the IP decreases significantly, reversing the polarity of 4D signal, and a 10% increase in gas saturation produces a softening effect (15% IP decrease).

Competing 4D seismic effects are often mentioned but rarely quantified, and their resultant non-uniqueness impacts on similarity indicators used in data assimilation processes. As these similarity indicators are generally based on comparisons between observed and modeled seismic, the methodology

presented results in an improved confidence on the workflows. Additionally, the methodology proposed is straightforward and adequate to reduce uncertainty related to 4D seismic interpretations.

Introduction

Among the main steps to interpret 4D seismic data are the forward modeling of synthetic seismic response and linking the results with the field's expected production scenarios. The observations are then assimilated in processes to update reservoir models. One of the challenges in assimilating repeat seismic data to update reservoir models are the uncertainty associated with the non-unique combinations of physical effects and the number of true possible 4D signal they may result to.

With the increasing use of permanent reservoir monitoring, processing and interpreting large volumes and different types of frequently acquired data with a fast turnaround became crucial (Hatchell et al. 2013; Lopez et al. 2017). Machine learning approaches aim to predict physical changes using seismic attributes in general rely on simplifications such as unique physical effects with approximately linear relationships with seismic data (e.g. Xue et al. 2019). This is especially problematic in the presence of gas, where its signal overcomes the other signals in many cases. Besides, many automated data assimilation workflows rely on similarity metrics calculated between observed and synthetic seismic data (e.g. Stephen et al., 2014; Obidegwu et al., 2017) where the optimization procedures may disregard the link between physical effects and magnitude or shape of 4D signals.

The competing effects are often mentioned but it lacks examples where they are actually quantified (e.g. Berthereau et al., 2019) and tied to observed data. This study aims to quantify and minimize uncertainties from competing 4D effects and to advance the discussion regarding their impact in data assimilation into reservoir models. We demonstrate that when more sophisticated approaches to decouple these competing effects, such as the use of prestack simultaneous 3D and 4D inversions (e.g. Nasser et al., 2017) are not available, or when a quick 4D interpretation is required for decision making, one can adapt a traditional 4D interpretation method to rock physics understanding and quantify these effects in a procedure that calibrates the modeled effects to observed data.

Objective

The objective of this paper is to (1) present a methodology to quantify competing 4D effects; and (2) discuss their impact on interpretations, modeling and their resultant similarity indicators used in data assimilation.

Methodology

The methodology comprehends five steps:

Step 1: Petro-elastic modeling (PEM)

The petro-elastic model is a set of equations that describe the link between reservoir rock and fluid properties and elastic properties. Many theoretical and empirical methods are available for defining these relations. In this step, we define the best method according to their calibration to measured sonic and density well logs.

Step 2: Scenarios evaluation

The PEM calibrated at the previous step is used to generate elastic attributes in 1D domain using available sonic logs acquired before production started and in 3D domain at the simulation model scale for each time-step, using saturation, effective porosity and pore pressure values. The time-steps are defined as close as possible to the seismic acquisition dates.

The 1D analysis is done to understand elastic changes under various individual and combined production scenarios, e.g. variations in pressure, gas and water saturation. The aim of the 3D analysis is to evaluate elastic changes under scenarios interactions, using reservoir conditions for a range of production scenarios with the addition of simulated data (Sw, Sg, So, P) at the selected time-steps.

Step 3: Synthetic seismic generation

The previous analysis diagnosed the need for the PEM to account for brine salinity changes. Therefore the injected sea water salinity is introduced at a radius of 350m from the water injectors (defined according to simulated average injection front), and the formation water salinity is maintained at the other locations. The elastic properties obtained from this PEM are then converted into reflectivity values and convolved with a statistical wavelet extracted in a window around the reservoir depth to generate seismic amplitudes for each scenario and each combination of scenarios in 1D, 3D and 4D domains.

Step 4: Noise generation

Synthetic seismic data has to mimic the observed data in order to make fair comparisons. The synthetic noise is therefore generated and added to the synthetic data to reproduce possible problems related to each vintage acquisition and to repeatability between vintages. The random noise is defined according to the signal-to-noise ratio observed in the actual seismic data.

Step 5: Multi-attribute analysis and comparison with observed seismic data

Compare the observed seismic differences (1D logs, vertical sections and attribute maps) to the synthetic traces to tie the analysis of changes that have occurred in the reservoir. Attribute maps are generated following procedures from Stammeijer & Hatchell (2014) for both synthetic and observed seismic data. Similarity between observed signal and each synthetic set of combined effects is evaluated and interpreted according to other attributes available such as tracers and production data.

Field details

The tests are performed in a setting where a combination of effects is occurring simultaneously, and we are confident enough with the 4D interpretations due to good overall NRMS and seismic acquisition in a PRM setting. The S field is a deepwater unconsolidated turbidite sand from Campos Basin with high porosity and permeability. Production in S field started in September of year 0, and a conventional base seismic survey was acquired two months later. A full field ocean bottom life of field seismic system (LoFS) was installed to monitor water flood, overburden integrity, and the movement of injected and produced fluids through the field on a flexible acquisition schedule (Farmer et al., 2013, Galarraga et al. 2015). The monitor 1 was acquired in June of year 1 (3 months after water injection started), monitor 2 in February of year 2 and monitor 3 in March of year 3.

Initial reservoir pressure is just 100 psi above bubble point and is expected to be maintained by injection, and therefore pressure effect in 4D seismic is predicted to be minor. The 4D effects expected in the field are mainly related to water saturation increase, from water injection and formation water and gas breakout. The reservoir thickness is around 42 m and therefore tuning effects are present.

Seismic modeling

Petro-elastic model

A Hertz-Mindlin contact model is used to estimate the dry bulk and shear modulus (*kdry, μdry*) of the rock and their dependency with effective pressure (Mavko et al., 1998). Batzle & Wang (Batzle & Wang, 1992) equations are used to define the bulk modulus for each fluid (*koil*, *kgas*, *kwater*) and Wood's equation to define the bulk module for fluid mixture (*kfluid*). Finally, Gassmann's equations (Gassmann, 1951) are used to state the final saturated bulk modulus (*ksat*) using the saturation estimates from the well logs. The predicted data by the petro-elastic model are compared against the measured sonic logs: P-wave velocity (*Vp*), S-wave velocity (*Vs*) and density (ρ) to verify the fit quality (Figure 1).

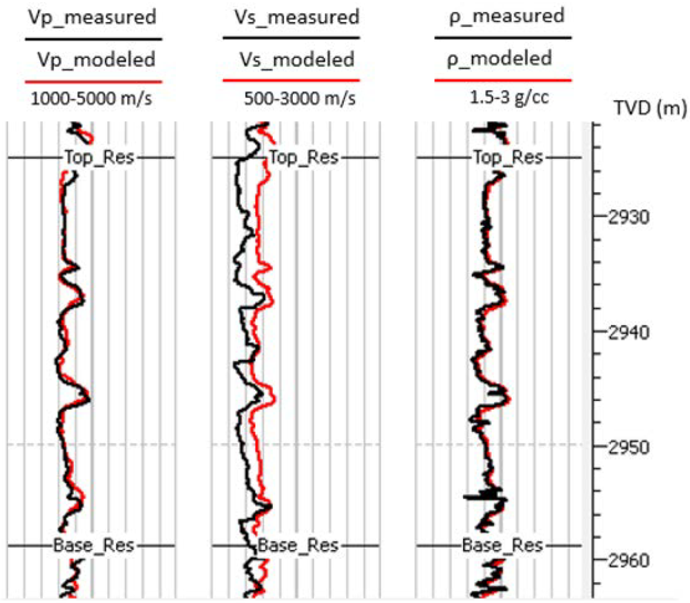

Figure 1—Fit quality between measured (black) and modeled (red) well log.

Scenarios evaluation - decoupled modeling

The set of equations defined at the previous step is then applied to various hypothetical production scenarios in the 1D domain (well location) to understand the elastic sensitivity to each of them.

Saturation effects. The 1D modeling illustrated in Figures 2a and 2b shows the two main effects that occur throughout production of S field: water saturation changes from 20 to 87% and gas saturation variations from 0% to 40%, considering a critical gas saturation, connate water and residual oil saturation as 40%, 20% and 13%, respectively. Figure 2a shows that an increase from 20 to 87% in water saturation (formation water replacing oil) causes an 8% increase in IP. Figure 2b shows that a 2% increase in gas saturation represents a decrease of 6.2% in IP.

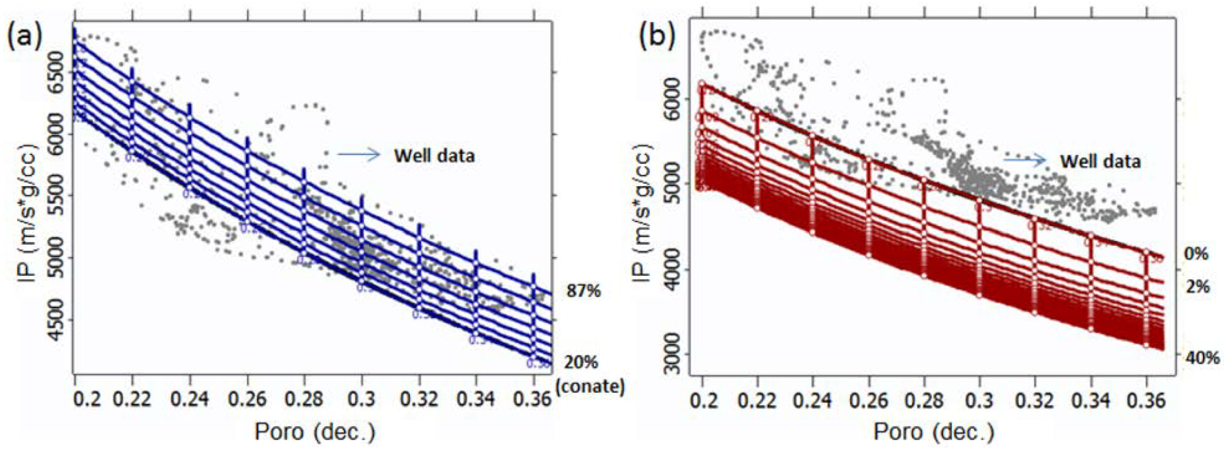

Figure 2—1D modeling of (a) water saturation increase and (b) gas saturation increase.
No free gas is present at this well and therefore the well data is calibrated to (a).

Salinity effect. Figure 3 shows the effect of salinity decrease as a result of injected water replacing formation water (180,000 ppm to 34,000 ppm). The salinity change causes an IP decrease of 3.5%.

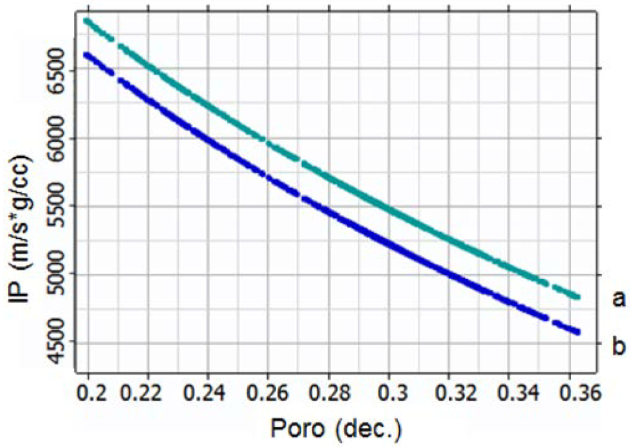

Figure 3—1D modeling of salinity effect (a) formation water being replaced by (b) injected sea water.

Pressure effect. Pressure effects are not significant for this field application as no major pressure variations are observed (up to 3MPa difference). The modeling from Figure 4 shows that less than 1.6% in IP change occurs when increasing the pore pressure from 30 to 33 MPa (a to c) and 2% when decreasing to 27 MPa.

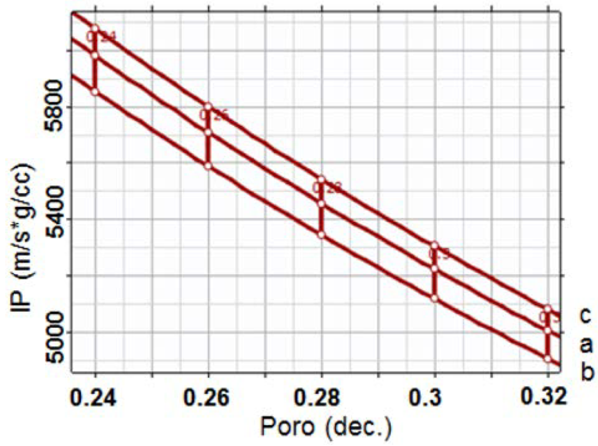

Figure 4—1D modeling of pressure effect (a) 30 MPa, (b) 27 MPa and (c) 33 MPa.

Scenarios evaluation - integrated modeling

The previous production scenarios are then combined to understand how their interaction affects the elastic sensitivity. A scenario where only water saturation effects occurs (e.g. aquifer water invading oil zone, scenario "a" to "b" from Figure 5), 12 to 16% IP increase is observed (hardening effect). However, according to salinity measurements and tracers, injected sea water with lower salinity than the formation water decreases the hardening effect to 8 to 10% in IP change (scenario c from Figure 5). This suggests that the salinity effect, although unremarkable when considered individually, as shown in the decoupled modeling, may be significant when associated with other effects, such as the water saturation increase. Additionally, combining these effects with gas going out from solution as a result of depletion below bubble point, the polarity of 4D signal reverses (scenarios d and e from Figure 5), and a 10% increase in gas saturation softens the IP by 15%. The synthetic traces from Figure 5c, d and e show that polarity of the signal may change depending on the combination of effects.

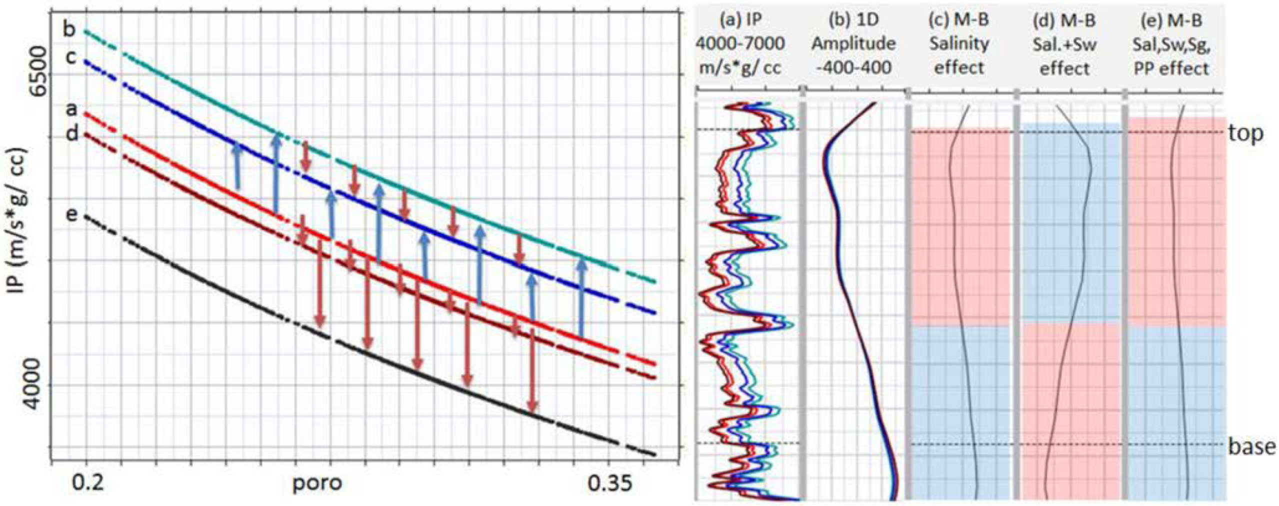

Figure 5—1D modeling (appraisal well A1) of the 4D expected effects. Left: (a) initial scenario, log saturated with oil and 20% of Formation connate water (salinity of 180000 ppm); (b) Fully saturated with Formation water; (c) Fully saturated with injected sea water (salinity of 34000 ppm); (d) Saturated with Formation water +2% increase in gas saturation and 2MPa pore pressure decrease; and (e) Saturated with Formation water +10% increase in gas saturation and 2MPa pore pressure decrease. Right: (a) modeled IP and (b) modeled synthetic traces for a, b, c and d scenarios. (c), (d) and (e) show the synthetic 4D differences (boosted 10 times in relation to b) caused by each of the effects respectively: salinity only, salinity + water replacing oil and salinity + water replacing oil + gas going out of solution and pore pressure decrease.

Amplitude generation and noise effect. After understanding the elastic changes occurring in 1D domain, a dynamic reservoir model with acceptable match with production data is selected and forward-modeled using the described petro-elastic model. Figure 6a shows a vertical section of the modeled 4D seismic difference between Monitor 3 (acquired in year 3) and baseline (acquired in year 0) for the selected simulation model. Figure 6b is the modeled 4D difference at the same location with the noise added to each seismic vintage, which is roughly similar to the noise from the observed 4D section seen in Figure 6c. The noise is spectrally shaped, that is, the frequency spectrum is flatten according to a supplied noise wavelet which improves the random spatial distribution of the noise. Figure 6b reproduces the noise from Figure 6c well without harming the signal seen in Figure 6a.

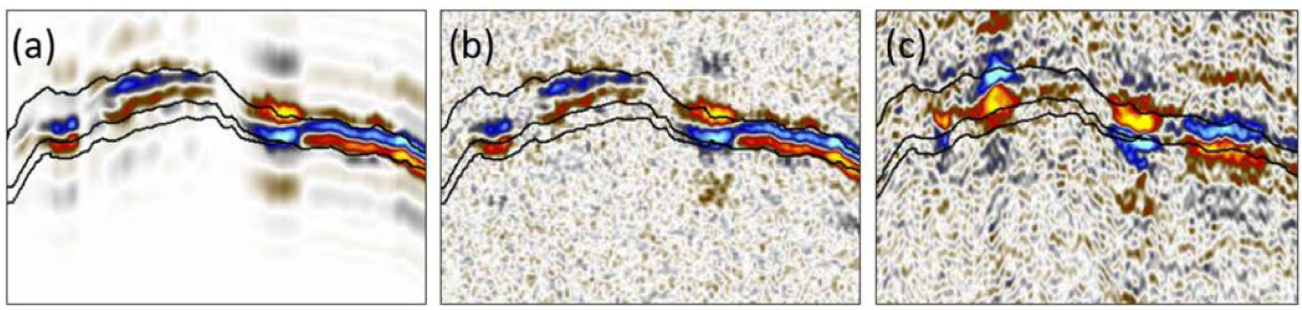

Figure 6—4D difference vertical seismic section examples: (a) synthetic, (b) synthetic with random spectrally shaped noise added, (c) observed.

Comparison with observed seismic data. Figure 7a shows the observed dRMS amplitude extracted between top and base of the reservoir from monitor 3 and baseline surveys. The producer well P2 was open in February of year 1, and the injector I2 was open two months after P2. P2 started producing water in November of year 1. The water produced by this well is interpreted to be injected water, according to salinity measures from the graph in Figure 8, and therefore the salinity changes effect would be detected after seismic monitor 2.

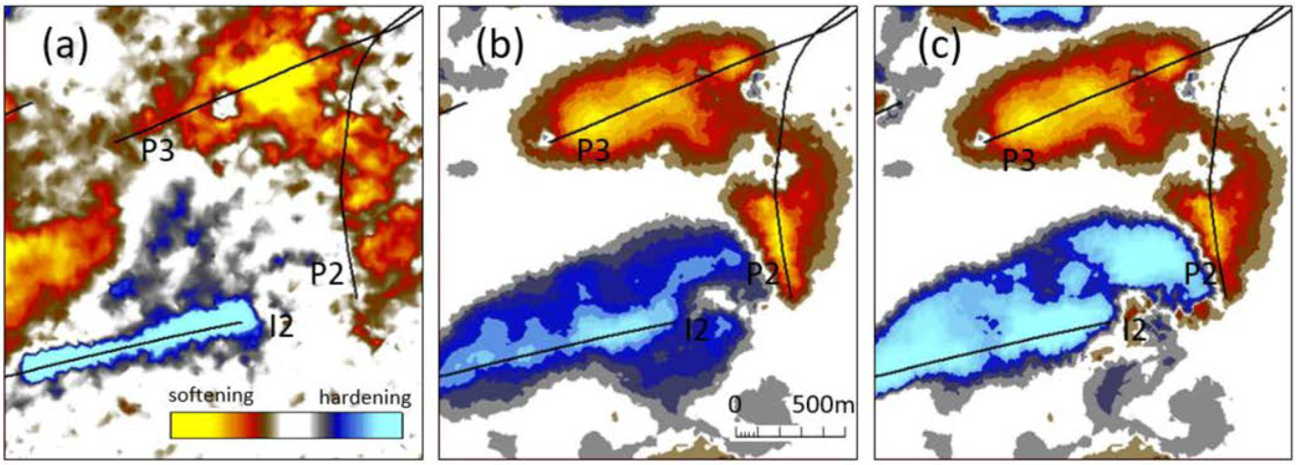

Figure 7—dRMS maps (top to base) between monitor 3 and base of (a) observed seismic, (b) simulated with salinity changes, (c) simulated without salinity changes.

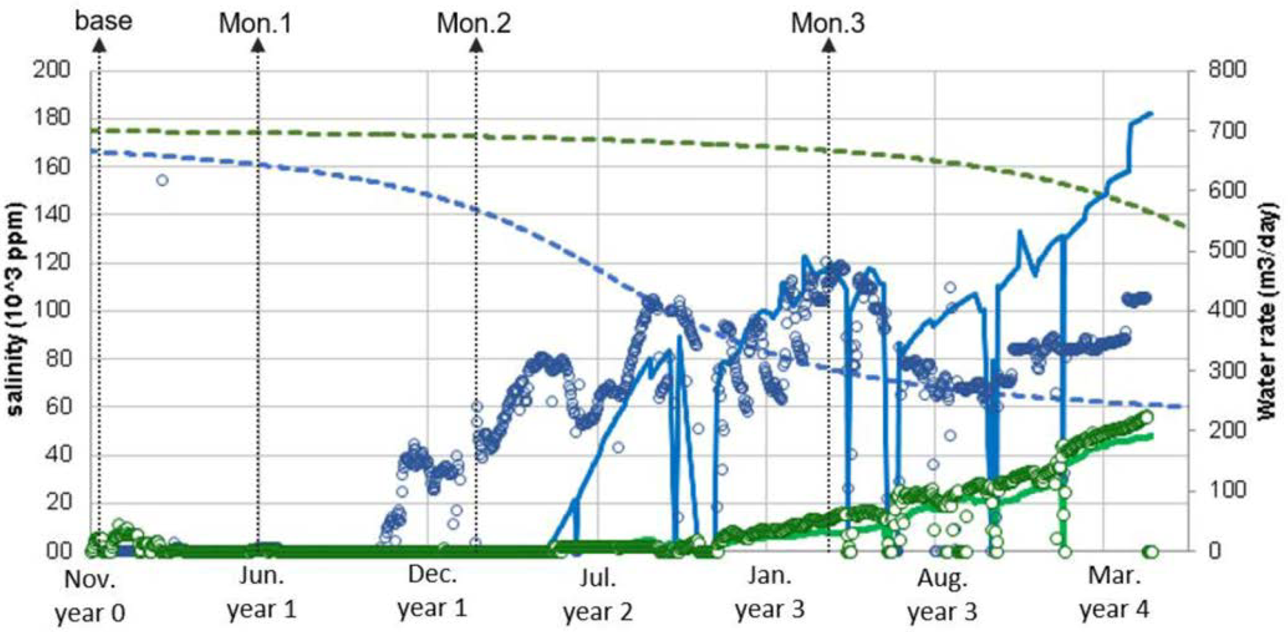

Figure 8—Estimated salinity per well (dashed lines), simulated water production rates (solid lines) and historical water production rates (circles) for production well P3 (green) and P2 (blue). The arrows indicate base and monitors seismic acquisition dates.

The previous 1D integrated modeling suggested that the salinity changes affect the hardening magnitude from the water saturation increase effect. Therefore, we performed a comparison between a "conventional" approach (using constant formation water salinity), and a new approach using salinity variations according to water injector distance. The new approach introduces sea water salinity at the PEM in a radius of 350m from the injectors and formation water salinity at the other locations, resulting in different total pore fluid bulk modulus and density and consequently, different 4D seismic magnitude for the two cases. The radius is defined based on an average of simulated water fronts, however, we highlight that this is a simple solution to consider water with different salinities as including brine mixture in reservoir simulation is a complex task, especially in this case where a black-oil simulator is used. In the context of handling large datasets resulting from frequently acquired data and hundreds of simulation scenarios, using a compositional simulator just for this purpose may not be the optimal solution. Figures 7b and 7c show the synthetic dRMS obtained from both with and without salinity variations respectively.

The salinity effect decreases the magnitude of the seismic hardening around the injector W2 by 50%, and increases the softening from P2 by 8% in the amplitude domain. Therefore, the synthetic attribute from Figure 7b presents greater similarity with observed data in terms of 4D signal magnitude. The injected water from I2 reaches producer P2 in the end of year 1, however, the effect of gas going out from solution, due to depletion below bubble point, overcomes the other effects and the polarity of the 4D signal reverses. This softening slightly stronger when combined with the salinity effect (Figure 7b as compared to Figure 7c). The constant salinity PEM results in overestimated hardening effect from water saturation and slightly underestimated softening due to its combination with gas effect. Whereas the shape of the anomalies does not match perfectly with observed seismic, due to imperfect simulation model calibration (i.e. softening anomaly at the left of P3 in Figure 7a not visible in Figure 7b and c), one can note that the combination of physical effects modifies the magnitude of similarity indicators between observed and synthetic datasets significantly.

Conclusions

This work presents a methodology to identify, quantify and address non-uniqueness resulting from competing 4D effects showing how we can monitor such changes. The combination of 4D effects, confirmed by several seismic attributes, such as IP, amplitude and dRMS, both in log (1D) and field (3D) scales, may change 4D signal polarity and magnitude significantly. The absolute IP decreases between 3.5 to 4.5% when only brine substitution (from formation water to injected water) is considered. When both the brine salinity change and the water saturation increase are taken into account, the absolute change in IP increases between 8 to 10%, whilst the IP increases 12 to 16% when only water saturation increase occurs. Additionally, having identified such interaction with salinity changes impacts on the 4D effects, an approach to include these changes in the PEM is implemented; resulting in a better match between modeled and observed 4D attributes, as compared to modeled attributes from a conventional approach that considers constant salinity. The proposed methodology is a simplified solution, considering that a more sophisticated compositional simulation to model the brine mixture may be unreasonable just for this purpose. Besides, it does not account for water fronts that may advance away from injectors. Regardless, we suggest further work to improve the salinity variation regions.

The contribution of this work is an improved confidence on interpretations. This study validates uncertainties in the competing 4D effects and their impact to the interpretations and data assimilation into reservoir models. Confirmed by simulated scenarios, understanding the combination of physical effects is crucial to get the right magnitude in similarity indicators between observed and synthetic datasets used in data assimilation procedures. Despite of the problem complexity, the forward modeling methodology proposed is straightforward and adequate to reduce uncertainty related to 4D seismic interpretations.

Acknowledgements

This work was carried out in association with the ongoing project registered under ANP number 20372-9 as ″Desenvolvimento de integração entre simulação de reservatórios e sísmica 4D - Fase 2″ (UNICAMP/Shell Brazil/ANP) funded by Shell Brasil Petróleo Ltda. under the ANP R&D levy as "Compromisso de Investimentos com Pesquisa e Desenvolvimento". The authors are grateful for the support of the Center of Petroleum Studies (CEPETRO-UNICAMP/Brazil), the Department of Energy (DE-FEM-UNICAMP/Brazil), the Research Group in Reservoir Simulation and Management (UNISIM-UNICAMP/Brazil) and Energi Simulation. In addition, special thanks to Schlumberger, CGG and CMG for software licenses. We also thank Felipe Mesquita, Frances Abbots, Jorge Lopez and Felipe Vilela for technical discussions.

References

Batzle, M., & Wang, Z., 1992. Seismic properties of pore fluids. *Geophysics*, **57**(11), 1396–1408.

Berthereau, G., Sanchez, R. and Emang, M., 2019. Successful Time Lapse Seismic Pilot on Al Shaheen field (Offshore Qatar): Analysis and Practical Applications in Reservoir Monitoring. In *IOR 2019–20th European Symposium on Improved Oil Recovery*.

Ebaid, H., Wang, K., Seixas, M., Kumar, G., Brew, G. and Mashiotta, T., 2017. Practical example of data integration in a PRM environment, BC-10, Brazil. *First Break*, **35**(2), pp.71–76.

Farmer, H. G., Buksh, G., Schostak, B. W., & Norberg, P., 2013. Pushing the Limits-4D Life of Field Seismic at BC-10 Brazil. In *Second EAGE Workshop on Permanent Reservoir Monitoring 2013–Current and Future Trends*.

Galarraga, M., Wang*, K., & Farmer, H., 2015. Results of 4D monitoring from the deepwater BC-10 life of field seismic (LoFS) in Brazil. In *SEG Technical Program Expanded Abstracts 2015* (pp. 5348–5352). Society of Exploration Geophysicists.

Gassmann, F., 1951. Elastic waves through a packing of spheres: *Geophysics*, **16**, no. 4, 673–685.

Hatchell, P. J., Wang, K., Lopez, J. L., Stammeijer, J. G. F., & Davidson, M., 2013. Instantaneous 4D seismic (i4D) for water injection monitoring. In *75th EAGE Conference & Exhibition incorporating SPE EUROPEC 2013*.

Lopez, J. L.; Cox, B.E.; Hatchell P.J.; Wang, K., 2017. Technology Options for Low-Cost On-Demand Seismic Monitoring in Deepwater Brazil. 15th International Congress of the Brazilian Geophysical Society, Rio de Janeiro, Brazil, 31 July to 3 August, 2017.

Mavko, G., T. Mukerji, and J. Dvorkin, 1998. The Rock Physics Handbook: Tools for Seismic Analysis of Porous Media, first edn., Cambridge University Press.

Narongsirikul, S., 2019, April. Ekofisk Time-Lapse Seismic Monitoring of Injection in Shale. In *Sixth EAGE Shale Workshop*.

Obidegwu, D., Chassagne, R. and MacBeth, C., 2017. Seismic assisted history matching using binary maps. *Journal of Natural Gas Science and Engineering*, **42**, pp.69–84.

Stammeijer, J. G. F., & Hatchell, P. J., 2014. Standards in 4D feasibility and interpretation. *The Leading Edge*, **33**(2), 134–140.

Stephen, K.D. and Kazemi, A., 2015. Improved normalization of time-lapse seismic data using normalized root mean square repeatability data to improve automatic production and seismic history matching in the Nelson field. *Geophysical Prospecting*, **62**(5), pp.1009–1027.

Xue, Y., Araujo, M., Lopez, J., Wang, K. and Kumar, G., 2019. Machine learning to reduce cycle time for time-lapse seismic data assimilation into reservoir management. *Interpretation*, **7**(3), pp.SE123–SE130.

APPENDIX D – ARTICLE 2

Journal of Petroleum Science and Engineering 210 (2022) 110083

Contents lists available at ScienceDirect

Journal of Petroleum Science and Engineering

journal homepage: www.elsevier.com/locate/petrol

Fast diagnosis of reservoir simulation models based on 4D seismic similarity indicators

Juliana Maia Carvalho dos Santos[a,b,*], Daiane Rossi Rosa[a], Denis José Schiozer[a], Alessandra Davolio[a]

[a] University of Campinas, UNICAMP, Brazil

[b] PGS Suporte Logístico e Serviços Ltda. Brazil (PGS)

ARTICLE INFO

Keywords:
4D seismic
Reservoir Monitoring
Data assimilation
Reservoir simulation

ABSTRACT

In the last ten years, 4D seismic (4DS) data acquisition is evolving to permanent reservoir monitoring (PRM) systems where sensors are installed at the ocean-bottom, collecting seismic data according to the project's monitoring demand. Simultaneously, reservoir management workflows evolved to include uncertainties, where multiple reservoir models may be considered. Model-based approaches for developing and managing a field rely on error minimizations between modelled and measured data, traditionally from well production data, and eventually adapted to 4DS data. This study presents a fast, robust and unsupervised workflow to provide a comprehensive diagnosis of multiple reservoir simulation models using similarity indicators with observed 4DS. The methodology comprises a seismic forward modelling to convert hundreds of models from the reservoir engineering domain to the seismic domain. The diagnosis includes a novel region-by-region approach to compare the predicted synthetic seismic response with the observed 4DS anomalies using ternary maps generated from Gaussian mixture models (GMM), in addition to a magnitude metric. The methodology is tested in an ultra-deep turbidite field from the Campos basin in Brazil with a PRM system that captured various 4DS anomalies of different polarity, magnitude, shapes and sizes over several production and injection years. The contributions of this work are demonstrated in four applications: (1) feedback on various iterations of geomodelling, (2) feedback on well and seismic data assimilation, (3) quick evaluation of a new seismic monitor, and (4) ranking models for further decision-making studies. The workflow advantages are proved along the model-based reservoir management outline. For application (1), we successfully flagged which 4DS anomalies were being honored in the simulation models and quantified the impact of introducing features interpreted from seismic monitors in the geomodelling. For application (2), we quantified simulation model improvements provided by data assimilation. For application (3), we rapidly evaluated the quality of the seismic monitor against the existing simulation models as soon as the new seismic acquisition and processing was complete, validating the requirement to re-visit the simulation models. Finally, the workflow was crucial to select best models, out of hundreds, for the decision-making process, in application (4).

1. Introduction

The main stages of the decision analysis process in the model-based reservoir development and management based on the closed-loop concept rely on error measures between modelled and measured data. Schiozer et al. (2019) presented a comprehensive methodology establishing 12 steps for model updating and production optimization under uncertainty, where building and calibrating models, data assimilation, selecting representative scenarios, and risk assessment are supported by the errors measured from well production data, and are increasingly being supplemented from 4D seismic (4DS).

Finding a practical framework for integrating 4DS on decision analysis remains a big challenge in the reservoir management area. The amount of data to analyze and include in the loop increases substantially as the project evolves, and as new technologies, such as permanent monitoring systems, are implemented. Another challenge in these workflows are the analysts' subjectivity to evaluate, interpret and incorporate 4DS in the simulation models. This may vary according to

* Corresponding author. University of Campinas, UNICAMP, Brazil.
E-mail address: juliana.maia@cepetro.unicamp.br (J. Maia Carvalho dos Santos).

https://doi.org/10.1016/j.petrol.2021.110083
Received 27 September 2021; Received in revised form 16 December 2021; Accepted 25 December 2021
Available online 28 December 2021

experience, background, and availability of complementary data such as production rates and geological information. Ultimately, we need a quick way to give feedback on simulation model ensembles, and to assess 4DS monitors as soon as they are made available for guiding critical decisions.

Being an interdisciplinary task, this integration is complex, yet, data assimilation workflows unraveled the potential to quantitatively incorporate this data into the simulation models. An example of a powerful tool to perform data assimilation is the Ensemble Smoother with Multiple Data Assimilation (ES-MDA) proposed by Emerick and Reynolds (2013), which aims to modify uncertain properties from the models to match with observations (well and 4DS data), as they become available (Oliver and Alfonzo, 2018). However, one assumption for a successful application of this type of method is to have a good prior ensemble, with well-mapped prior uncertainties. A framework to diagnose the prior ensembles becomes an important step to be performed before running data assimilation. For well data, it is common to use quadratic errors measured from assimilated and observed data series, such as the NQDS (Normalized Quadratic Deviation with Sign) used in several works (e.g. Avansi and Schiozer, 2015; La Rosa Almeida et al., 2018; Formentin et al., 2019) to have a complete view of all objective functions in a concise plot. When it comes to 4DS data this comparison is not straightforward as we need to compare maps and not time series.

Furthermore, these misfits' measures may be affected by biases towards outliers or may generate global error values that mask significant local misfits, which emphasize the importance of evaluating the reservoir region by region. The first focus of this study is, therefore, to present a workflow to measure similarity indicators between observed seismic monitor and reservoir simulation models, providing both a global and a local misfit metric.

The methods published so far for providing these misfits are successful but cannot address all aspects of the problem at the same time. The most typically used least-square based errors do not account for shape errors between both responses, likewise, shape-based methods disregard problems related to misfit in magnitude of the 4D signal. Chassagne and Aranha (2020) made a comprehensive review on magnitude-based measures in the data assimilation context and discussed the Least Square metric is as able to capture important information as other more sophisticated metrics.

Regarding the shape metrics, several authors proposed approaches to represent the 4DS information by converting their attributes into binary images, and measure errors considering pixel by pixel misfits. In many cases, they involve domain conversions between the various branches of knowledge which requires performing seismic modeling and/or seismic inversion. The best domains in which to incorporate the seismic at remain uncertain, however the most common domain is seismic impedance, which requires to run a petro-elastic modeling for each simulation model in the ensemble and the execution of a 4D seismic inversion to convert observed seismic amplitudes into impedance changes. Oliver et al. (2021) made a comprehensive review on the limitations and advantages on the domain choice, uncovering the 4DS history matching challenges, particularly on the modeling of seismic data. Tillier et al. (2013) effectively proposed a formulation with binary image analysis based on Hausdorff distance between observed and simulated P-impedances changes and demonstrated it with a deterministic history matching case. Luo et al. (2016), on the other hand, adopted amplitude vs. angle (AVA) domain comparisons in a 2D case, where the AVA attributes were computed from the reflection coefficients calculated by a petro-elastic model, introducing a wavelet-based sparse representation. The authors then successfully extended their work to a 3D case in Luo et al. (2018) and later, in Luo et al. (2021), applied these attributes to demonstrate their methodology on handling model errors from seismic forward modeling from a machine-learning perspective. Soares et al. (2020) also adopted the AVA domain and selected the main features of the 4DS attributes using a Dictionary learning method. Souza et al. (2018) likewise selected the full petro-elastic and forward modeling approach to consider all characteristics of the seismic method: such as the influence from overburden, underburden, wavelet, and, most importantly, the combinations of dynamic effects. Our methodology follows their work, because the amplitude domain is the one immediately available once acquisition and processing finishes, and to avoid running seismic inversions.

On the other hand, several authors successfully used direct cross-domain comparisons between responses from simulator and different seismic attributes, avoiding the additional petro-elastic modeling step. Obidegwu et al. (2015) applied threshold values to provide binary observed amplitude and simulated gas saturation 4D difference maps and used the hamming distance to calculate their misfit. Trani et al. (2017) used k-means clustering to binarize time-lapse relative change of P-wave velocity and simulated dynamic properties, and measured the misfit between them according to distances to 4D anomaly front. Davolio and Schiozer (2018) also worked with k-means clustered amplitude and saturation maps, applying the misfit function proposed by Tillier et al. (2013). Zhang and Leeuwenburgh (2017) adapted the Hausdorff distance to measure dissimilarity at fluid fronts. The binary approaches present two main limitations: the 4DS attributes are compared to one single dynamic property change, and they only account for existence and absence of 4D signal, disregarding its polarity.

Some authors proposed interesting data-driven solutions to provide misfits between 4DS and simulation models, such as the momenta tree method (Soriano-Vargas et al., 2020) and the deep learning using models trained by 4D experts, using convolutional neural networks (Rollmann, 2020), which have been tested in synthetic cases and look promising on real cases.

Assembling the shape of the 4DS attributes into clusters may be challenging, because they rely either on threshold values for 4DS signal definition, filtering (e.g. Derfoul et al., 2013), or clustering algorithms, and their execution are not always straightforward, especially in a 4D project. The threshold approach may be unpractical because cutoff values may have to be reviewed depending on the seismic monitor. The seismic monitors ideally should be acquired and processed the same way but in practice this is not always possible. Repeatability and noise level may vary amongst vintages depending on the seismic acquisition conditions (e.g. different sources or acquisition parameters, seismic interference, and sea conditions). Moreover, the intensity of the 4D signal changes throughout the monitor surveys. Also, if hundreds of simulation models outputs need to be compared with 4DS data, a fixed cutoff probably will not be enough to cluster the data. Regarding the clustering algorithms, the most applied in previous works is the k-means. However, its convergence assumes spherical clusters and equal probabilities for each cluster. Therefore, it may also not work for all kinds of seismic attribute values distributions, because centroids can be dragged by outliers not assuring the definition of the expected number of clusters.

To generate ternary maps clustering hardening, softening and absence of 4D anomalies this work proposes the segmentations into Gaussian mixture models (GMM). The GMM is an unsupervised learning technique, where data is unlabeled and the program fits gaussians for the input data. The expectation-maximization (E-M) algorithm then estimates and optimizes the models based on their maximum likelihood that a certain observation belongs to each gaussian. Limited seismic applications are reported for the technique: clustering earthquake signals (Seydoux et al., 2020), as inversion prior models (Astic et al., 2021; Fjeldstad et al., 2021), seismic facies analysis (Wallet and Hardisty, 2019) and data assimilation schemes (Dovera and della Rossa, 2011). Regarding specific 4DS integration applications, Zhao et al. (2007) presented a modification of the E-M algorithm, applied to measure errors from 4DS and production data. Amini et al. (2019) compared several objective functions to history match three models, including errors from binarized maps using GMM, initialized using the manually defined thresholds. With this parameterization, they concluded, however, the GMM was not able to capture differences between the models as well as the threshold methods.

We cluster a selected 4DS attribute into three segments (ternary maps) with automatic initializations based on the attributes' statistical distribution. The ternarization using this method performs very well, given the inherent gaussian distribution of the 4D attributes. This method can also provide soft (the likelihood of a point to belong to a certain cluster) and hard clustering (whether the point belongs or not to a certain cluster) and it works very well in the presence of noise. The shape similarity is then measured using the hamming distance between observed and predicted ternary maps, modified to consider the size of each analysis region.

This work presents a robust approach to provide similarity indicators between hundreds of simulation models and 4DS that simplifies our data into ternarized maps with the GMM and to use them complementarily to a magnitude error measure. Therefore, the metric comprehends three shapes (negative, positive and 4D absence shape) and a magnitude factor, both globally and region-by-region.

To validate our workflow, this paper presents four applications in a model-based reservoir management loop from a deep-water Brazilian clastic field with great variety of 4D responses related to shape, polarities, and magnitudes: (1) feedback on geomodelling, (2) feedback on data assimilation, (3) quick evaluation of a new seismic monitor, (4) filtering models for further optimization studies. The methodology was extensively used to quickly access the quality of reservoir models, providing both general quality overviews and specific problems within regions.

2. Gaussian mixture models (GMM) and the expectation-maximization (EM) algorithm

The GMM labels input data considering posterior probability distributions. The models are fitted to data according to given or random initial conditions: the mean μ, the variance σ and, optionally, the mixing proportions π for each cluster k. The program estimates the probability $p(x)$ that a sample occurs at a certain location x, of the component densities p_k, given their parametric initial conditions.

$$\boldsymbol{p}(\boldsymbol{x}) = \sum_{k=1}^{K} \boldsymbol{\pi}_k\, \boldsymbol{p}_k\left(\boldsymbol{x} \middle| \boldsymbol{\mu}_{k,} \boldsymbol{\sigma}_k\right) \tag{1}$$

where

$$0 < \pi_k < 1 \text{ and } \sum_{k=1}^{K} \pi_k = 1 \tag{2}$$

The EM algorithm then fits GMM's to data optimizing a maximum likelihood function. The E-step provides a soft clustering, that is, it computes the posterior probability E that a component i belongs to cluster k.

$$E_{i,k} = \frac{p(x = x_i | \mu = \mu_i\ ,\ \sigma = \sigma_i)}{\sum_{i=1}^{k} p(x = x_i | \mu = \mu_i,\ \sigma = \sigma_i)} \tag{3}$$

The M-step estimates the distribution of each cluster based on the latest assignment.

$$\mu_i\ \sigma_{i,} = \frac{\sum_i E_{i,k} x_i}{\sum_i E_{i,k}} \tag{4}$$

3. Methodology

The methodology comprises the following steps:

1. **Preparation of observed 4D data.** As the intention is to fast-track results to guide critical decisions, we generate 4D difference of the root mean square (dRMS) amplitude maps produced between key reservoir intervals, as the amplitude domain is the most readily available once the seismic acquisition and processing finish. For acoustically soft reservoirs, the dRMS is described by Stammeijer and Hatchell (2014) as follows:

$$dRMS_{obs} = \mathrm{RMS}_{obs}(Baseline) - \mathrm{RMS}_{obs}(Monitor) \tag{5}$$

However, the workflow can be adapted to any domain, or any map or seismic volume. The maps are then standardized to avoid distance-based problems in the clustering algorithm, and to compare units in similar scales. The observed dRMS standardized Z_{obs} value is given by:

$$Z_{obs} = \frac{\mathrm{dRMS}_{obs} - \mu_{obs}}{\sigma_{obs}} \tag{6}$$

Where μ_{obs} and σ_{obs} are the mean and standard deviation of the entire $dRMS_{obs}$ map.

2. **Region segmentation according to observed 4DS anomalies boundaries.** The regions must collectively cover the entire map. This step must be carried out in conjunction with the 4DS interpretation, locations of wells and each region must account for presence and absence of 4D signal.
3. **Forward modeling.** Static and dynamic properties such as porosity, net-to-gross ratio, fluid saturations, and pore pressure are extracted from reservoir models and are converted into the seismic domain using a Petro-elastic model. This step generates seismic attributes such as density, P and S-wave velocity. The P-impedances (product between the P-wave velocity and density) are then calculated for each grid cell from the simulation model, and then transferred to a seismic regular grid spaced as close as possible to the model grid. The P-impedances are converted to seismic reflectivity at normal incidence and then convolved with a wavelet extracted from the observed 3D baseline seismic, at the reservoir interval. We chose to work in the time domain because it is a requirement for the convolution process. We add Gaussian random noise to each trace sample to match the observed noise level (Santos et al., 2020). The signal to noise ratio is defined using root mean square (RMS) estimates from the observed 3D baseline seismic signal and noise.

Generate $dRMS_{syn}$ maps at the same interval as step 1, and standardize according to:

$$Z_{syn} = \frac{\mathrm{dRMS}_{syn} - \mu_{syn}}{\sigma_{syn}} \tag{7}$$

where μ_{syn} and σ_{syn} are the mean and standard deviation of the entire $dRMS_{syn}$ map.

The processes from this step are streamlined in an automatic Petrel workflow that generates the synthetic 4DS attribute maps.

4. **Run GMM and EM to cluster observed and predicted maps.** For a 4DS attribute, we consider three clusters: (k_1) representing the negative polarity (softening) anomalies, (k_2) the zeroes (absence of 4D anomalies), and (k_3) the positive (hardening) anomalies. We assume the repeatability noise level is low enough to be fitted in the same gaussian k_2, the random noise already has a normal distribution around zero inherently. We provided same initial conditions for both observed and predicted data, based on statistics of the normalized 4DS attribute (minimum observed dRMS for μ_{k1}, 0 for μ_{k2}, and maximum observed dRMS for μ_{k3}).
5. **Comparison between observed vs. synthetic seismic data.**
   a) Shape evaluation: entire reservoir and region error calculation. The observed and predicted ternary maps are compared through a shape metric SM calculated by the Hamming distance between the observed pixel o and predicted pixel p from the ternary maps, divided by n_r, i.e., the size n of each region r (or number of pixels inside each region), given by:

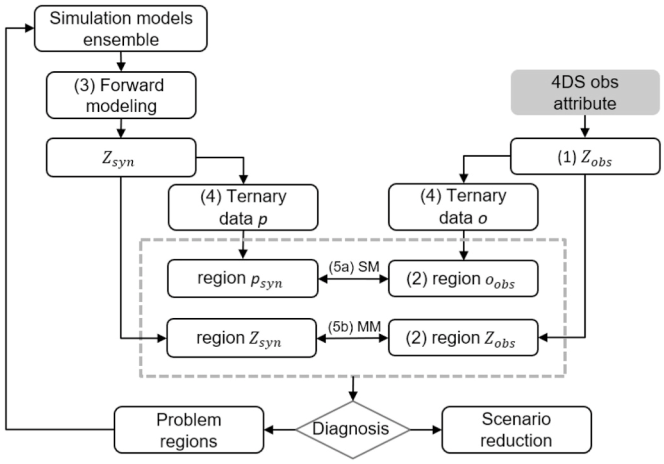

Fig. 1. Methodology workflow.

$$SM[o,p] = \frac{\sum_{i=0}^{i} \delta_i(o,p)}{n_r} \tag{8}$$

where

$$\delta_i(o,p) = \begin{cases} 1 \text{ if } o_i \neq p_i \\ 0 \text{ if } o_i = p_i \end{cases} \tag{9}$$

b) Magnitude evaluation: entire reservoir and region error calculation. The magnitude metric *MM* is given by the mean square error between Z_{obs} and Z_{syn}.

$$MM[Z_{obs}, Z_{syn}] = \frac{\sum_{i=1}^{nr} (Z_{obs} - Z_{syn})^2}{n_r} \tag{10}$$

Fig. 1 summarizes the methodology steps. Note that it can be an iterative workflow depending on the application, for example, when problematic regions are flagged, or if the simulated models are not minimally matching the 4DS observations. Besides, when new seismic monitors or new data are acquired, the workflow can be used to verify their impact on 4D similarity. If the objective is to reduce the number of models, we propose an outlier detection method based on each metric, for each region *r*:

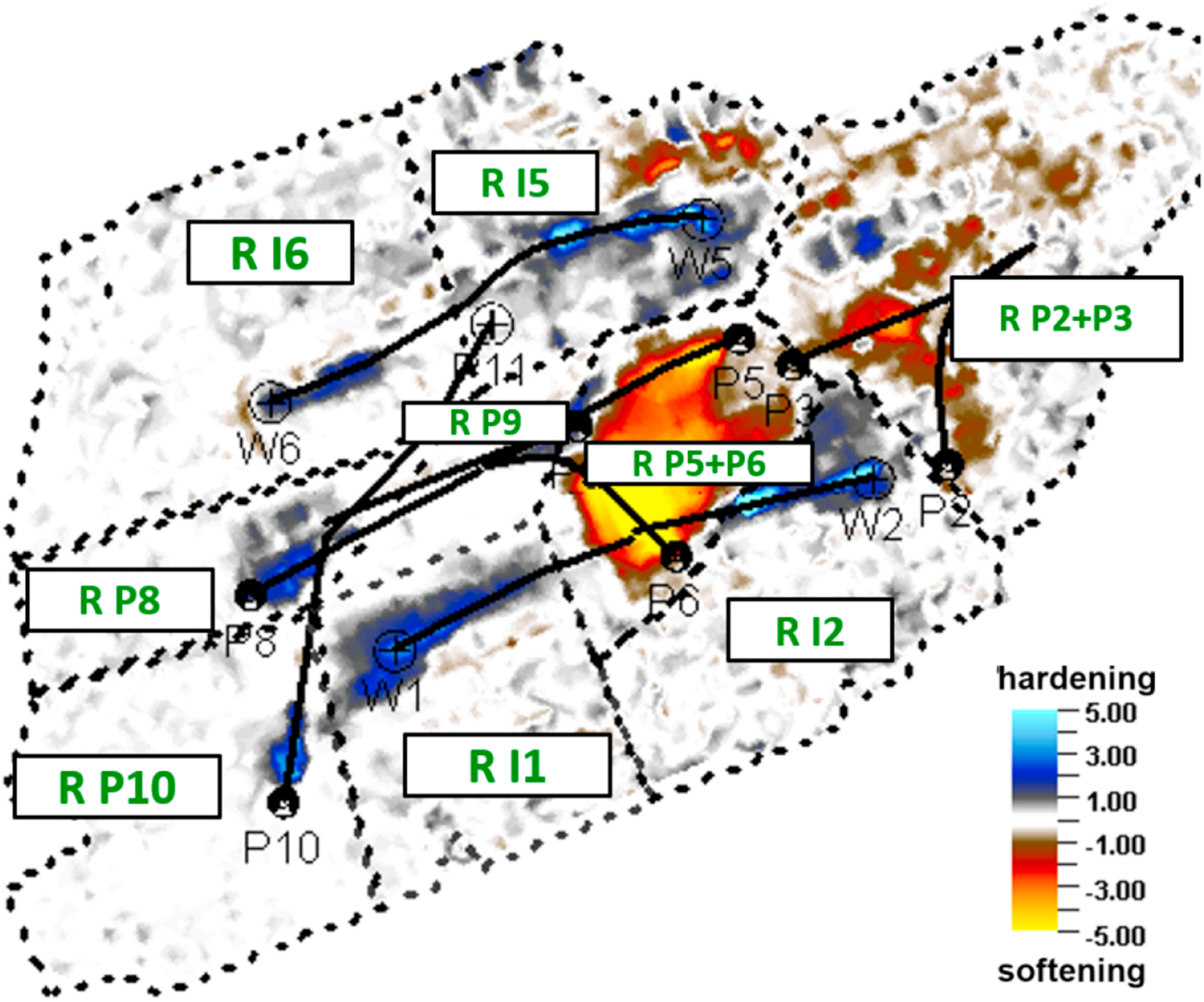

Fig. 2. dRMS extracted between reservoir top and base - monitor 3 (year 3) vs. baseline. The black dashed lines are the regions separation, defined according to the 4D signal shape.

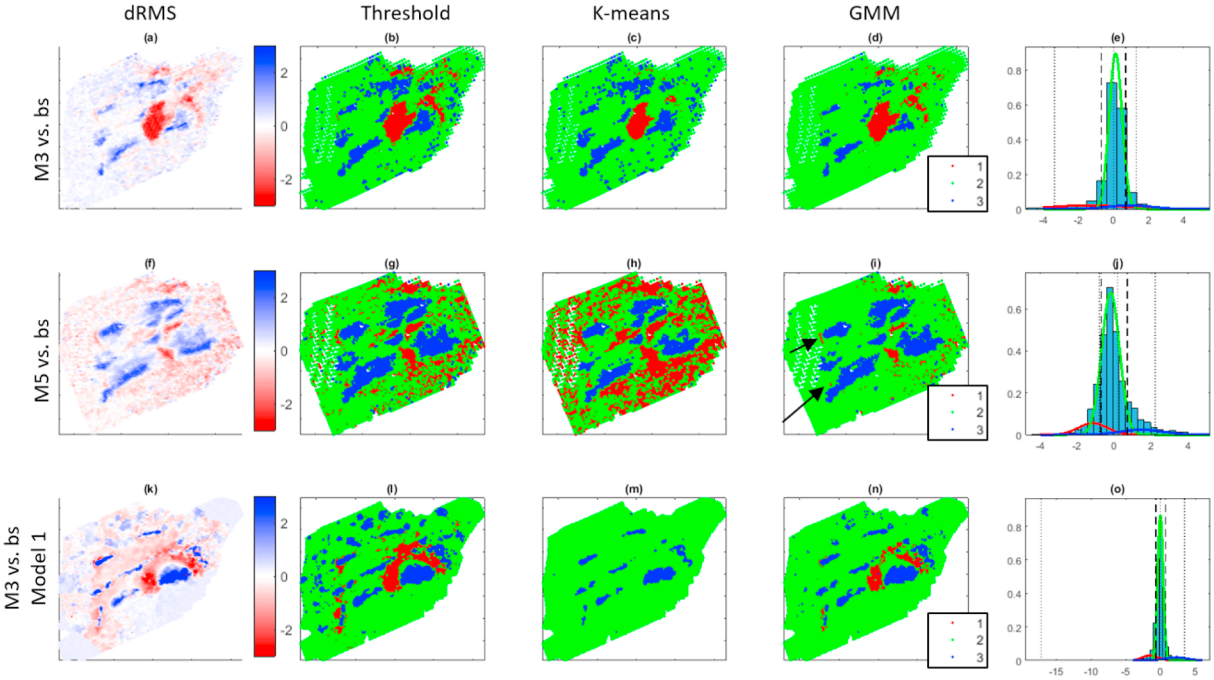

Fig. 3. dRMS maps ternarized using threshold, k-means and GMM, and their corresponding histograms. (a) to (e) for observed monitor 3 vs. baseline, (f) to (j) for observed monitor 5 vs. baseline and (k) to (o) for the synthetic 4DS seismic resulted from forward modeling of model 1 considering monitor 3 and baseline times. The histograms show the Gaussian model mixture distributions (continuous lines), the k-means centroids (dotted line) and the threshold values (dashed line) overlaid at the dRMS values distributions.

$$Out_{SM,r} = \mu_{SM,r} + a\,\sigma_{SM,r} \tag{11}$$

$$Out_{MM,r} = \mu_{MM,r} + a\,\sigma_{MM,r} \tag{12}$$

where the coefficient a may be project-dependent. We propose the reservoir models with *SM* and *MM* values above $Out_{SM,r}$ and $Out_{MM,r}$ values respectively, for any region, to be filtered out. Note that a single region with SM and MM values above these limits is enough to filter out a reservoir model.

4. Application to a siliciclastic field

4.1. Field setting

The methodology is applied to a heavy oil deepwater turbidite field located in the Campos Basin, at the Brazilian east margin. The reservoir is thin (average 25 m), with a trough reflection at the top and peak at the bottom, and therefore dRMS maps between top and base are considered appropriate to capture the main 4DS anomalies. The reservoir is stratigraphically trapped, pinching out to the northeast. To the west, the reservoir is structurally contained by 3 major faults with NE-SW direction. The sand's quality is good with an average porosity of 25%, which may be contaminated with thin (sub-seismic resolution) shale intercalations.

The field was initially developed with 7 horizontal producer wells and 4 horizontal water injector wells. Production started in year 0, with initial pressure just above the bubble point. The baseline survey was acquired and water injection started 4 months later. Since then, several seismic monitors were acquired using 100 km of ocean-bottom cables (OBC) arranged in 14 lines: monitor 1 (7 months after baseline), monitor 2 (9 months after monitor 1), monitor 3 (almost one year after monitor 2), monitor 4 (18 months after monitor 3) and monitor 5 (almost 3 years after monitor 4).

Strong 4D anomalies related to gas going out of solution are observed up to monitor 3 in two regions: near production wells P5 and P6 and near production wells P2 and P3. The 4D signal from water replacing oil is also very dominant, where water moves both from injectors and from the aquifer (e.g. near P8 and P10). Fig. 2 shows the 4D dRMS map between monitor 3 (year 3) and baseline, illustrating the mentioned anomalies, as well as the well trajectories. More details about the field are explained in Buksh et al. (2015); Chen et al. (2015); Ebaid et al. (2017); and Maleki et al. (2019).

4.2. Petro-elastic model

Provided the geological characteristics, the Hertz-Mindlin contact model is used to estimate the dry bulk and shear modulus (*kdry, μdry*) of the rock and their dependency with effective pressure (Mavko et al., 1998). Batzle & Wang equations (Batzle and Wang, 1992) are used to define the bulk modulus for each fluid (*koil, kgas, kwater*) and Wood's equation to define the bulk module for fluid mixture (*kfluid*). Finally, Gassmann's equations (Gassmann, 1951) are used to state the final saturated bulk modulus (*ksat*) using the saturation estimates from the well logs. More details in (Santos et al., 2020).

4.3. Simulation models

The simulation models have a total of 88,768 cells, in a 73 × 38 x 32 grid, with approximate sizes of 150 m × 150 m x 4 m at the i, j and k directions respectively, simulated using the black-oil numerical reservoir simulator IMEX (CMG). The models were generated under 53 scalar uncertainties such as initial water-oil contact depth, multipliers that define the absolute permeability in vertical direction, connate water saturation, fluids relative permeability, irreducible oil saturation, and rock compressibility, with 200 geostatistical realizations of static properties such as horizontal permeability, porosity, net-to-gross ratio and facies. The full details on the uncertainty parameters and ranges are detailed in Maschio et al. (2021). These uncertainties were combined using the Discrete Latin Hypercube with Geostatistical realizations method (Schiozer et al., 2017) resulting in 200 different models. Various iterations of geomodelling were performed, according to new information acquisition or field knowledge increase. Posterior ensembles of

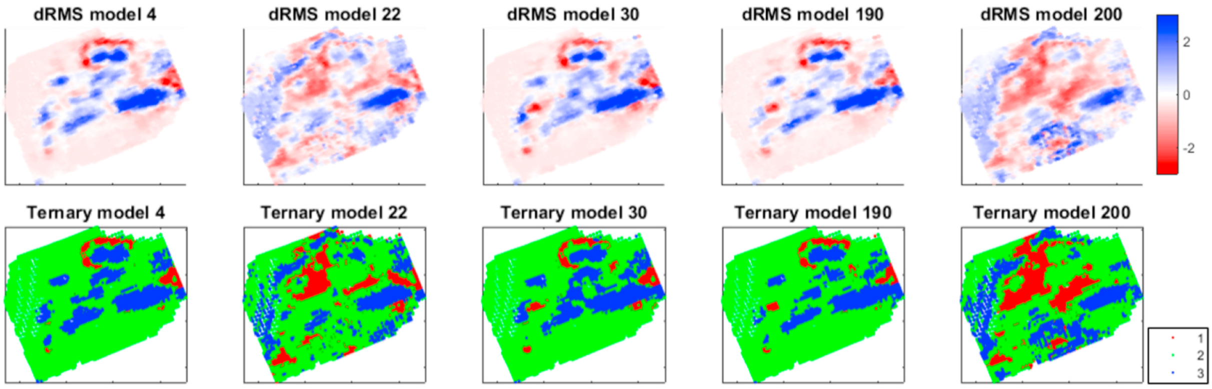

Fig. 4. Predicted dRMS maps between monitor 5 and baseline for 5 random models (top), and their correponding ternary maps (bottom).

models (after data assimilation) were also considered. The following sets were selected in this work, all of them comprising 200 reservoir simulation models with different level of reservoir characterization:

Set S3D: Geomodelling iteration 1, using 3D seismic (from the baseline survey) as co-variable without introducing features interpreted from 4DS.

Set S4D: Geomodelling iteration 2, adding features interpreted from 4DS introduced (up to monitor 3), as described in Maleki et al. (2021), and improved knowledge on the reservoir behavior and its heterogeneities.

Set S4D_post_W: Set S4D after data assimilation using the ES-MDA method, including well history data only, up to year 5). The models were updated in four iterations, using BHP data for all wells and oil rates for producers, and total liquid and water rates for producers and injectors, respectively, as boundary conditions.

Set S4D_post_WS: Set S4D after data assimilation using the ES-MDA method, including well and 4DS data. The settings and well data used are the same as Set S4D_post_W, with the inclusion of one 4DS map corresponding to the ratio of inverted acoustic impedances between monitor 3 and baseline, extracted between reservoir top and base.

5. Results

5.1. Region separation

This process requires knowledge on the field's dynamic behavior and well trajectories. In this study, the regions are defined according to polygons that contain the 4D anomalies and proximity with wells. The absence of 4D signal is equally important. The black dashed lines from Fig. 2 show the region segmentation (region names in green) over the dRMS map between monitor 3 and baseline. The misfit between observed data (dRMS of monitor 3 and simulation models) are calculated for the entire reservoir and for each region, in terms of shape and magnitude.

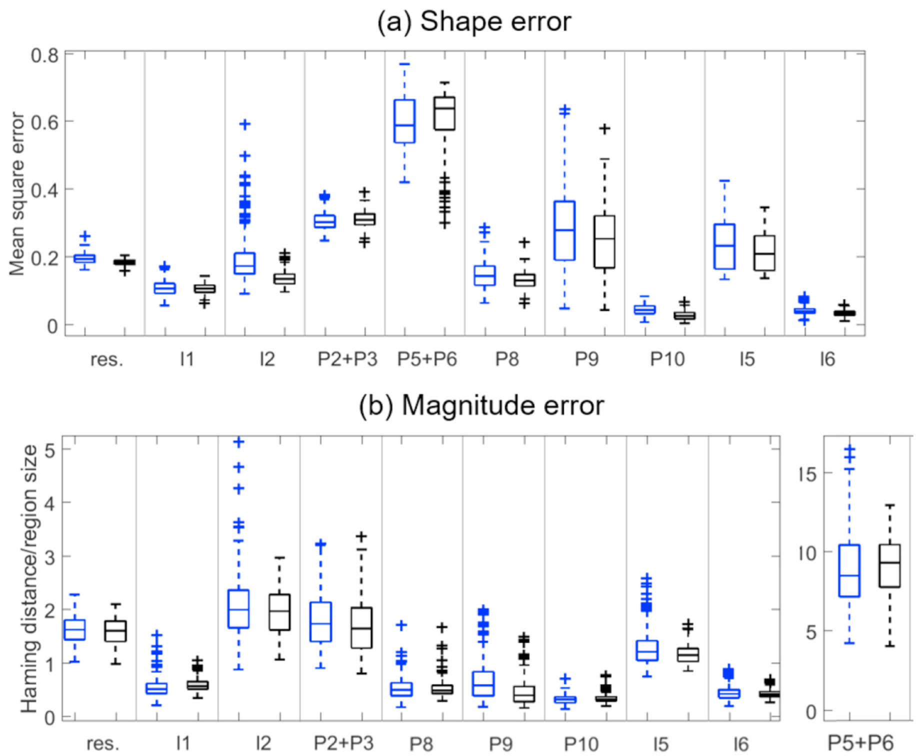

Fig. 5. (a) Shape error and (b) magnitude error for the set S3D (blue) set S4D (black). Note the error scale difference for P5+P6 due to higher error. (For interpretation of the references to colour in this figure legend, the reader is referred to the Web version of this article.)

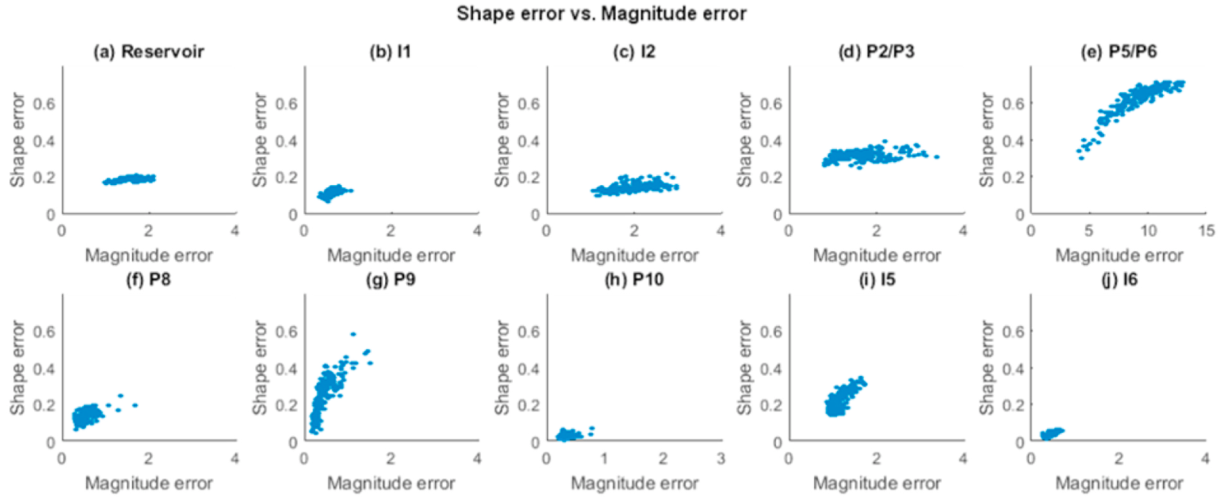

Fig. 6. Shape error vs. Magnitude error for set S4D.

5.2. *Maps ternarization and the shape metric*

As mentioned in section 4.1, the field application contains different 4DS anomalies in terms of polarity, magnitude, and shapes. Fig. 3 shows three examples of the resulting ternary maps using conventional methods (threshold and k-means) and the proposed method (GMM), generated from the standardized dRMS between monitor 3 and monitor 5 vs. baseline. The histograms show the fitted mixture models, k-means centroid and the threshold values overlaid (Fig. 3i, j and o). The GMM method works as expected, clustering the softening anomalies, zeroes, and hardening anomalies within clusters 1, 2 and 3 respectively, even in the presence of noise which had dubious interpretations. It also picks detailed 4D features such as the fluid front indicated by the arrows from Fig. 3i, resulting from the injected water pushing oil. The examples also suggest that threshold values are not the same within all surveys, in this case, due to noise content (dashed lines in Fig. 3i, j and o). The k-means optimization method, using minimization of Euclidean distances, may push the centroids too far from initialization values and result in an empty cluster, as seen in Fig. 3m. Therefore, the GMM is a good compromise between clustering noise and picking the important 4D features.

Fig. 4 shows the GMM clustering performance on dRMS maps predicted for five random simulation models (extracted between monitor 5 and baseline), from where we can observe the GMM successfully captured the three clusters of data in different model settings.

6. Discussion

6.1. *Evaluating geomodelling*

In the closed-loop field development and management workflow it is common to have various iterations of geomodelling as new information is acquired and as the knowledge on the field's behavior increases, emerging the need to generate new prior models. One approach to quantify improvements within these iterations is to measure errors against observed data. Conventionally, a simulation model uses quadratic errors against well production data, which are very local measurements and do not always reflect problems from the geological model. The 4D similarity metric complements the error evaluation due to its spatial significance. Fig. 5a and Fig. 5b show a shape and magnitude measure respectively, for two sequential iterations of geomodelling (set S3D in blue and set S4D in black), highlighting two problematic regions: P5/P6, in which both magnitude and shape mismatch are higher than other regions, and P9, with higher shape errors. They also show that the improvement from geomodelling set S3D to set S4D is not very straightforward to quantify. For example, the I2 region improves for the shape metric but not so much for the magnitude metric. The cross plots from Fig. 6 highlight the shape and magnitude metrics do not always present a good correlation, suggesting that the decisions to reject or accept a certain model would be different depending on the kind of error metric used.

Region P5/P6 is highly influenced by a strong gas anomaly, which affects the errors the most. Figs. 7 and 8 show the best and worst models

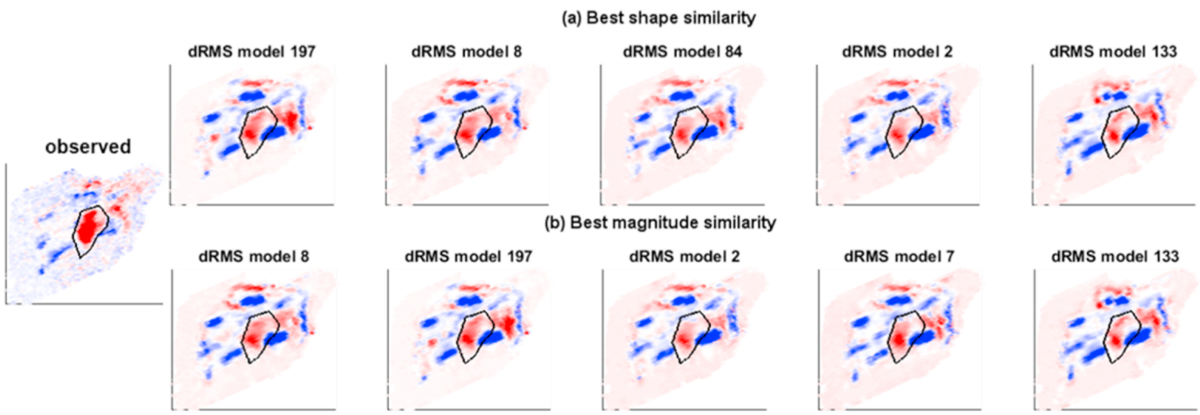

Fig. 7. Best 5 models according to (a) shape, and (b) magnitude similarity with 4DS (set S4D), measured at region P5/P6 defined by the black polygon.

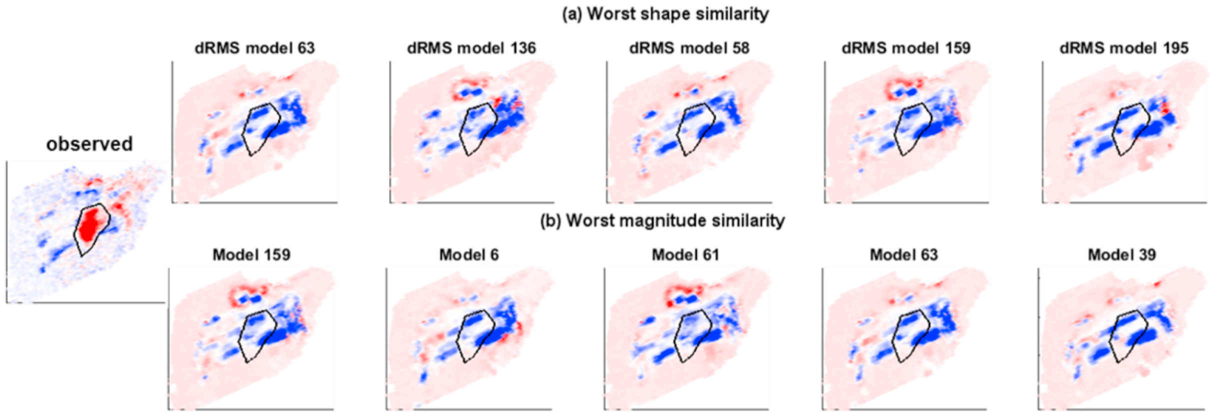

Fig. 8. Worst 5 models according to (a) shape, and (b) magnitude similarity with 4DS (set S4D), measured at region P5/P6 defined by the black polygon.

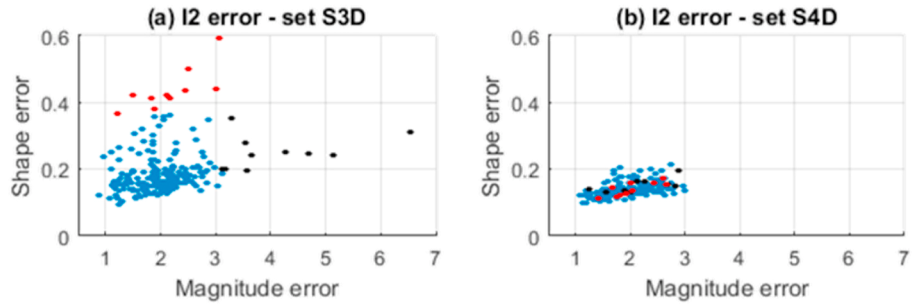

Fig. 9. Shape error vs. Magnitude error for region I2 at set S3D(a) and set S4D (b).

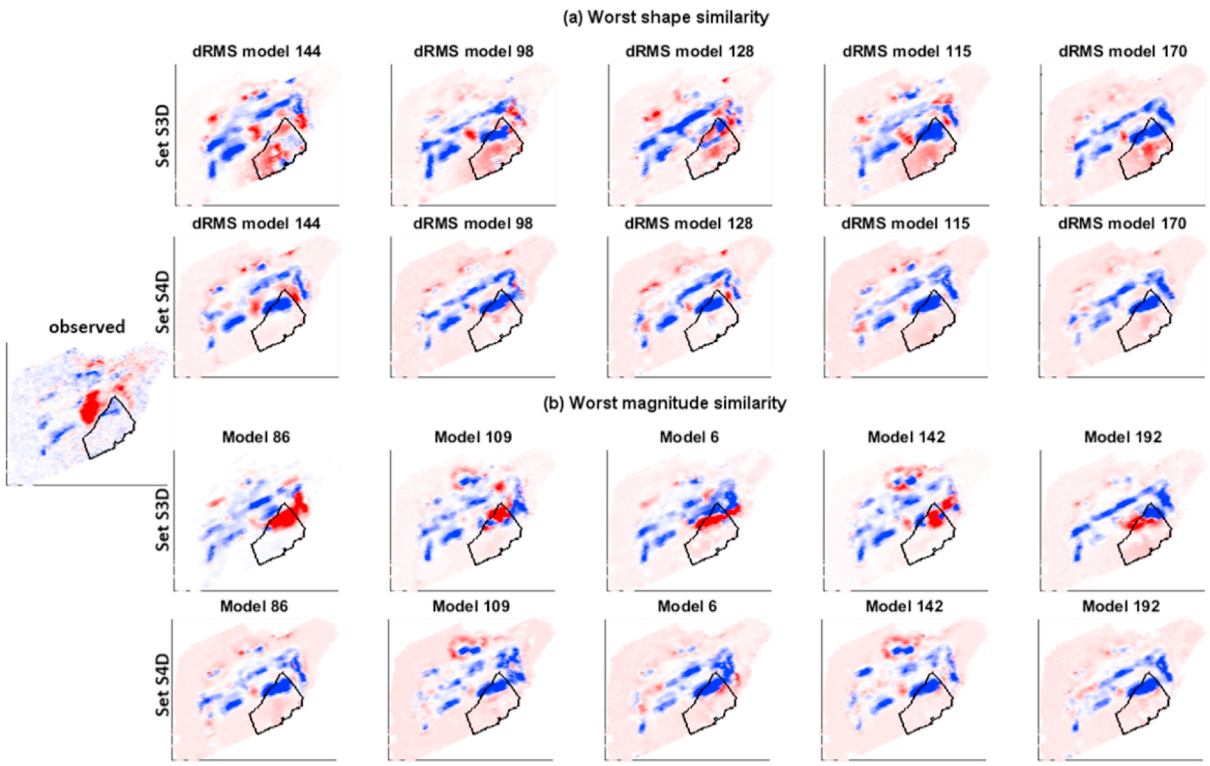

Fig. 10. Worst 5 models according to (a) shape, and (b) magnitude similarity with 4DS measured at set S3D for region I2 in the black polygon. The bottom figures show their similarity increase in set S4D.

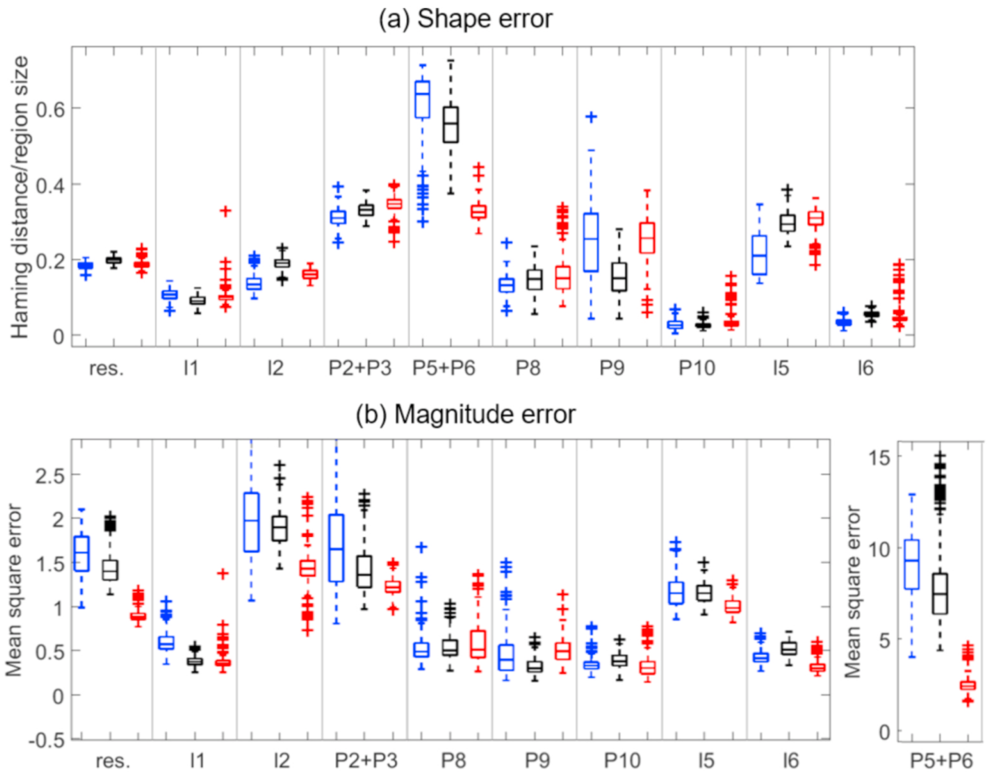

Fig. 11. (a) Shape error and (b) magnitude error for the set S4D (blue), set S4D_post_W (black), and set S4D_post_WS (red). Note the error scale difference for region P5+P6 due to higher error. (For interpretation of the references to colour in this figure legend, the reader is referred to the Web version of this article.)

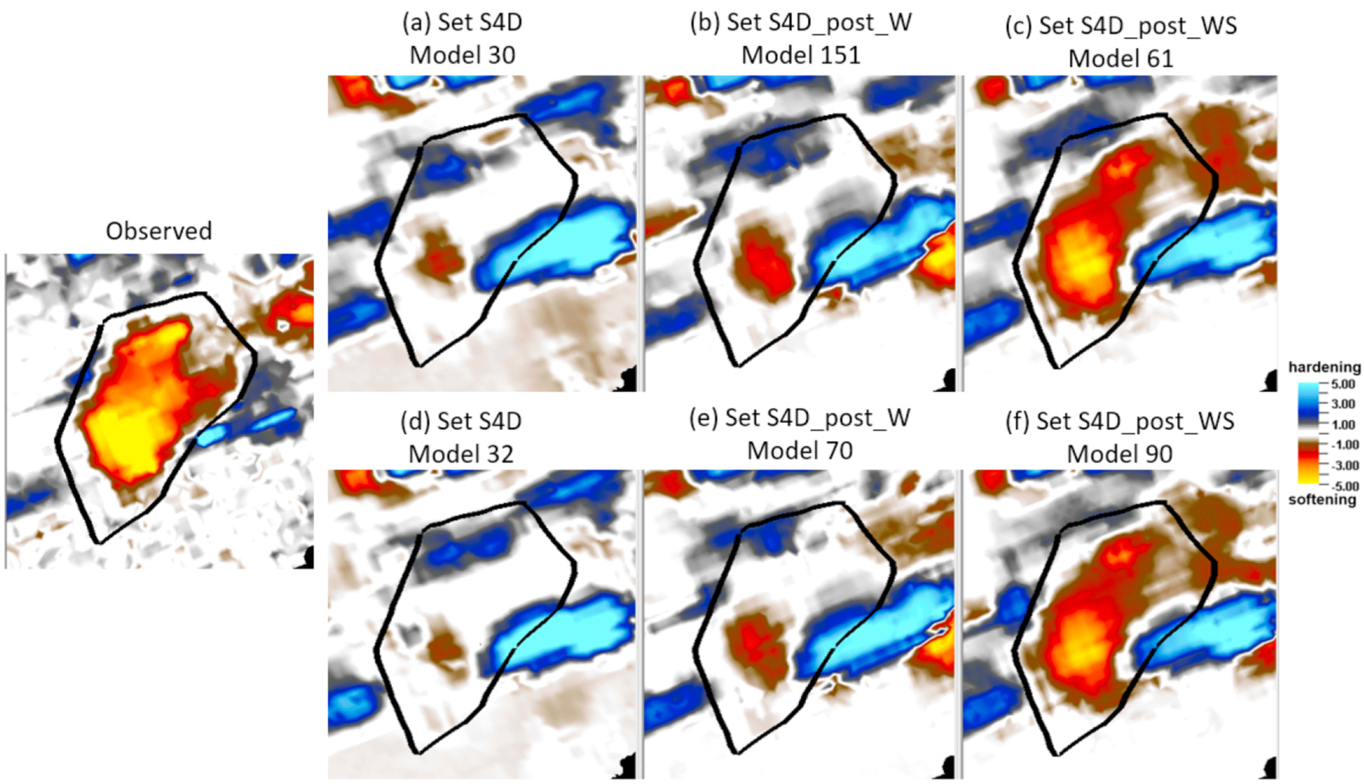

Fig. 12. Models with errors closest to the median error measured at region P5+P6, for models from set S4D, S4D_post_W, and S4D_post_WS. (a) to (c) use the shape metric, and (d) to (f) use the magnitude metric.

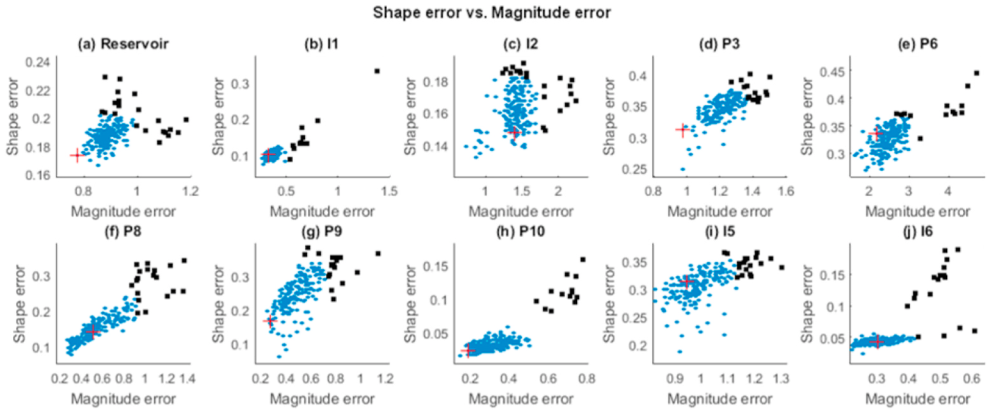

Fig. 13. Shape error vs. Magnitude error for set S4D_post_WS. The red plus sign represents model 11. (For interpretation of the references to colour in this figure legend, the reader is referred to the Web version of this article.)

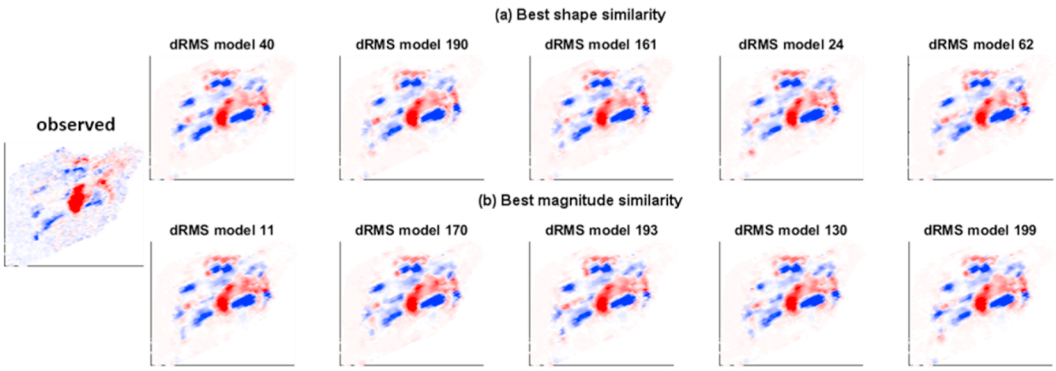

Fig. 14. Best 5 models according to (a) shape, and (b) magnitude similarity with 4DS (set S4D_post_WS), measured at the entire reservoir.

selected by both metrics in set S4D considering only the region P5/P6. The ranks obtained from both metrics are very similar, where the same models are considered top best and top worst at both, differing only a few positions. In fact, there is a strong correlation between both metrics in this region, which is illustrated in Fig. 6e.

The introduction of features detected on 4DS monitor and better knowledge on vertical heterogeneities on set S4D decreased the P8, P9 and P10 shape errors. However, this is not detected by the magnitude metric from regions P8 and P10, and the cross plots from Fig. 6f and 6h suggest a poor correlation between both metrics for these two regions. The shape error also decreases significantly for region I2 between iterations from set S3D and set S4D.

Fig. 9 shows the region I2 case in detail, demonstrating that although the mean of the magnitude errors did not change significantly, the set S4D presents fewer high error outliers. The worst models for the shape metric (red points) and for the magnitude metric (black points) from set S3D are indicated in the set S4D, being collapsed towards the shape and magnitude error means. Fig. 10a and b illustrate 5 of these worst models ranked in region I2 according to the shape and magnitude metric respectively at the set S3D, and their similarity improvement in set S4D.

Although the metrics flagged some regions to address in the geomodelling iteration (from set S3D to set S4D), an actual improvement was observed only after the model calibration/data assimilation process, as shown in the next discussion (6.2) for the region P5/P6 case.

6.2. Evaluating data assimilation

Fig. 11 shows a comparison between the set S4D from the previous

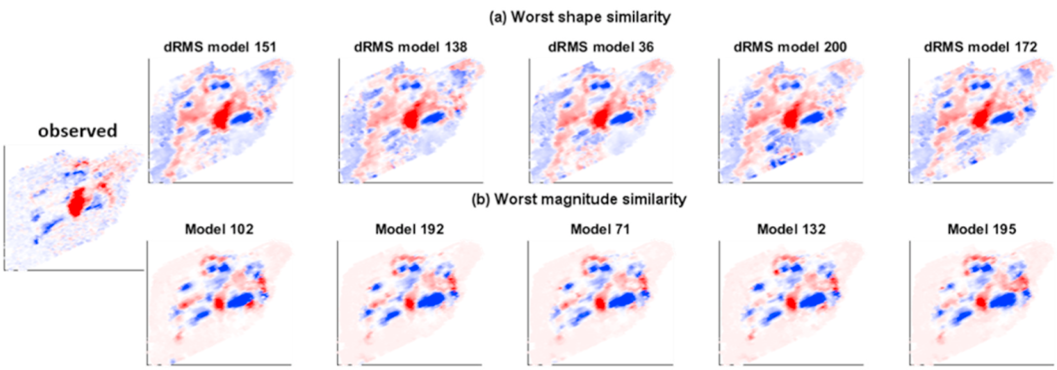

Fig. 15. Worst 5 models according to (a) shape, and (b) magnitude similarity with 4DS (set S4D_post_WS), measured at the entire reservoir.

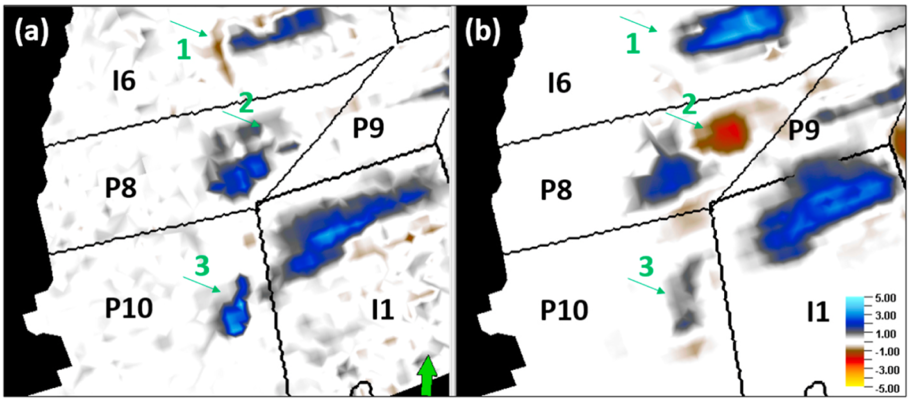

Fig. 16. Region detail of (a) observed dRMS and (b) Model 11 predicted dRMS at set S4D_post_WS.

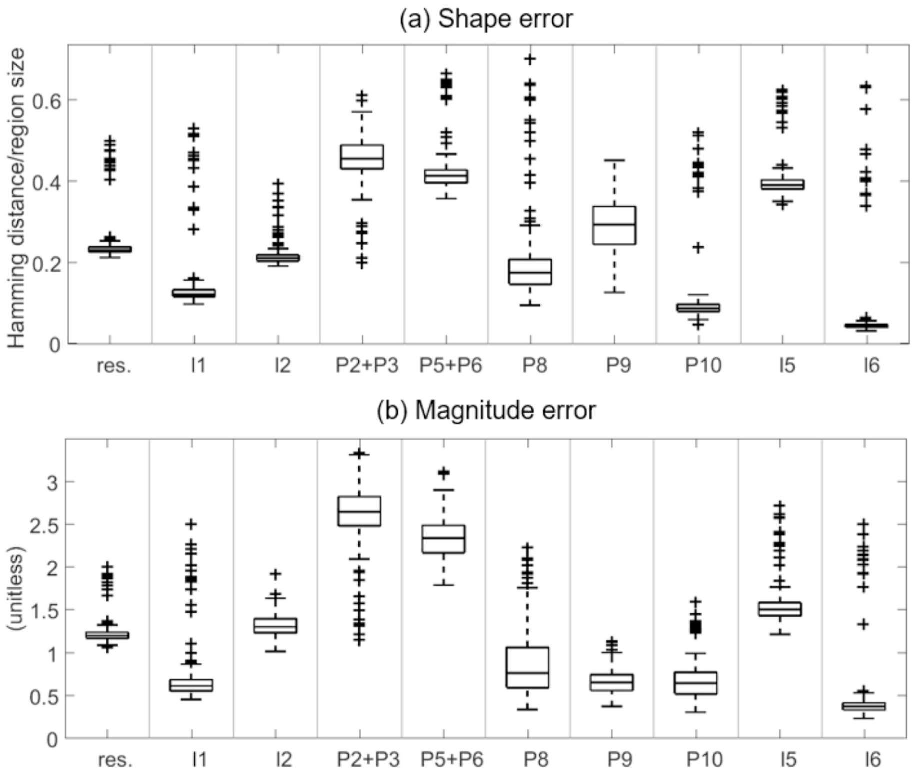

Fig. 17. (a) Shape error and (b) magnitude error for set S4D_post_WS (red) – new monitor (monitor 5).

section before data assimilation (blue), after data assimilation using only well data (set S4D_post_W, in black) and after assimilation with well and 4DS data simultaneously (set S4D_post_WS, in red). Most improvements from data assimilation are visible in the magnitude metric, as the ES-MDA technique uses the least-squares calculation on the data-mismatch objective function. Note that the shape errors are larger or similar before and after data assimilation in some regions, but region P5+P6 presents the most error decrease for both metrics. The data assimilation process has a significant impact on this region because it contains the strongest gas anomaly, thus its error level decreases towards the same error level as the other regions. Fig. 12 shows the models which errors are closest to the median error from each of the three sets, using both the shape (Fig. 12a–c) and magnitude (Fig. 12d–f) metrics, highlighting the incremental 4DS similarity improvement as the 4DS is assimilated, as expected. These plots also confirm that at least 50% of the models for the two sets S4D and S4D_post_W do not present the expected 4D signal, enhancing the need to quantitatively assimilate the 4DS data for these models. Note that the same does not happen for all regions, for instance, the data assimilation did not perform very well for region P8. The methodology assisted us to evaluate the data assimilation results of various sets resulting from different data assimilation parameters and inputs.

6.3. Models filtering

The previous applications demonstrate both magnitude and shape metrics are complementary. This section proposes to filter models using the metrics individually for each region and each metric. The cross plots from Fig. 13 show that the correlation between both metrics worsens as the errors increase. This is demonstrated by the models from Figs. 14 and 15: the best models according to the entire reservoir error look similar for both metrics but the worst do not. Besides, a global error given by the sum of magnitude and shape metrics may have a good overall average error for the entire reservoir, but local errors can vary depending on the

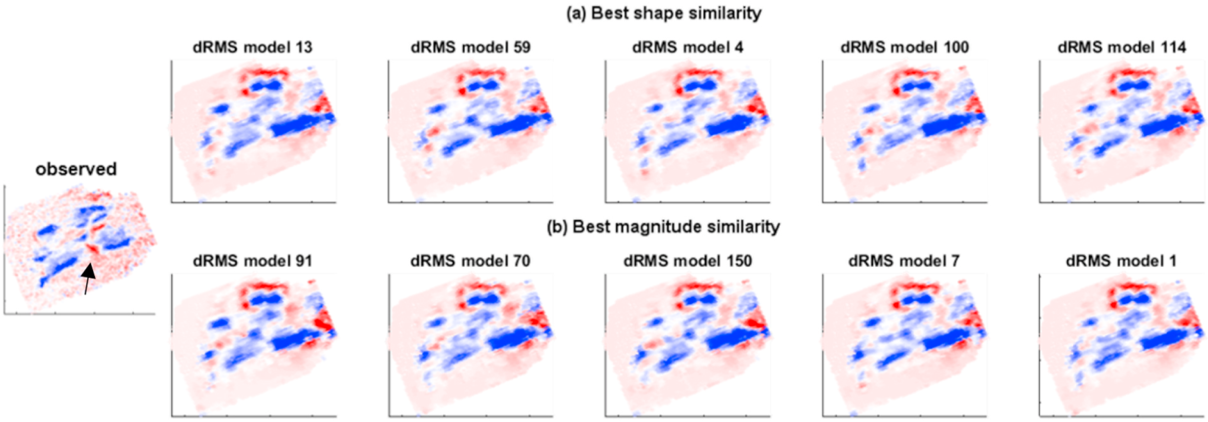

Fig. 18. Best 5 models according to (a) shape, and (b) magnitude similarity with 4DS (new monitor 5) for set S4D_post_WS, measured at the entire reservoir.

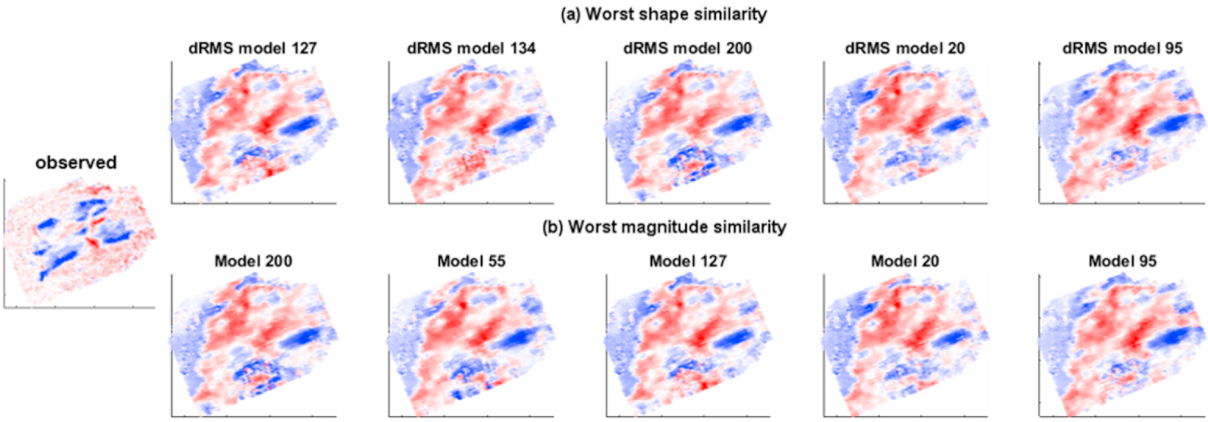

Fig. 19. Worst 5 models according to (a) shape, and (b) magnitude similarity with 4DS (new monitor 5) for set S4D_post_WS.

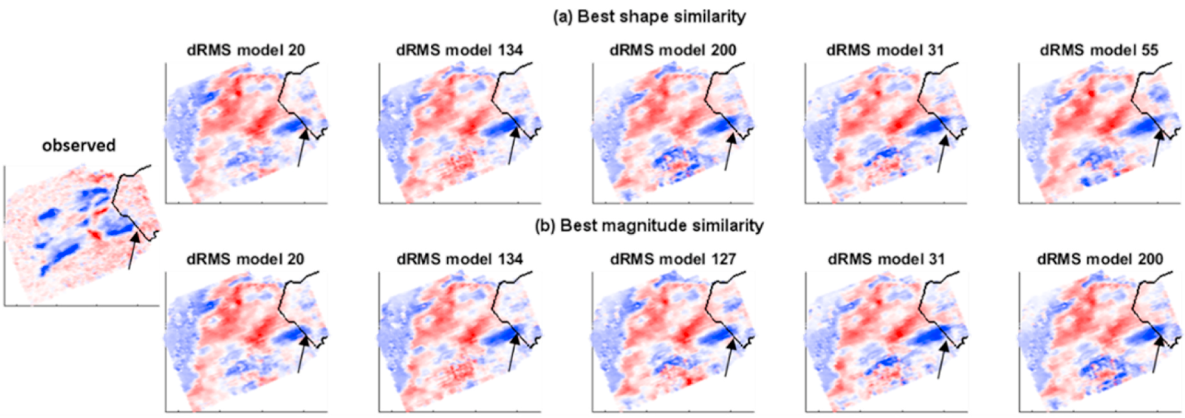

Fig. 20. Best 5 models according to (a) shape, and (b) magnitude similarity with 4DS (new monitor 5) for set S4D_post_WS, errors measured at region P2+P3 within the black polygon.

region. Model 11, represented by the red cross in the cross plots from Fig. 13 Fig. 14, presents the best overall error (lowest sum of magnitude and shape errors for the entire reservoir). However, cross plots from Fig. 13 b, e, f, i and j show this model is ranked as intermediate for these regions. The green arrow 1 from Fig. 16 indicates the lack of softening anomaly from injector I1 (water pushing oil) in this model, arrow 2 shows a non-existent softening anomaly in the observed data, wrongly predicted by the model, and arrow 3 shows a major magnitude and shape mismatch for the hardening anomaly caused by the water saturation increase. Note also the anomaly from region I1 is not contained, invading part of region P9, which also affects its errors.

The examples suggest that ranking and selecting models using error cutoffs considering each region and each metric separately is a better solution than summing and averaging errors as we guarantee that all regions are good. Also, the framework here proposed to evaluate 4DS misfits, as in Figs. 14 and 15, can be essential for some goals, such as defining an infill drilling position. We propose to filter out high error models, black squares from Fig. 13 cross-plots, according to their

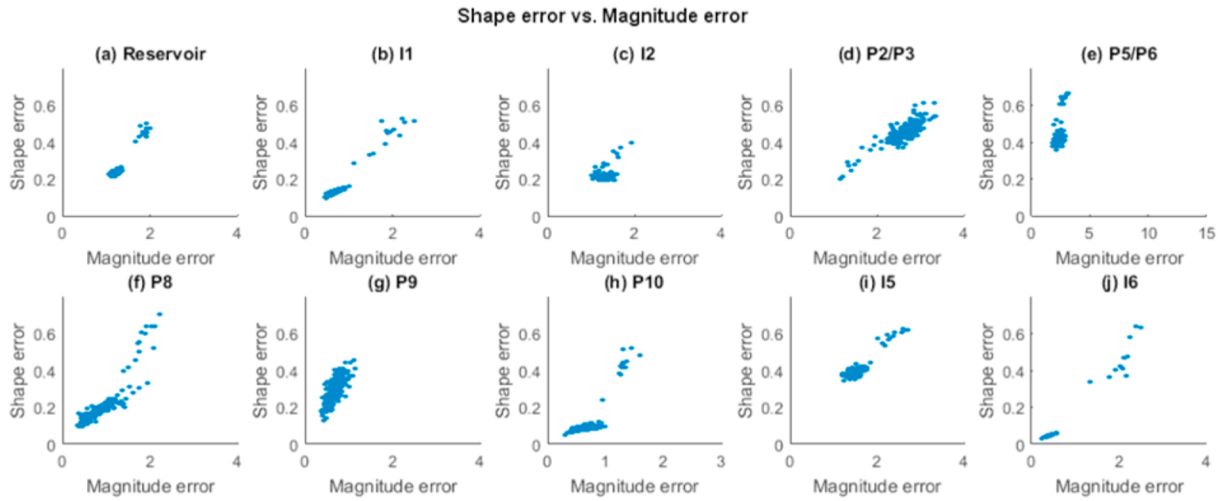

Fig. 21. Shape error vs. Magnitude error for set S4D_post_WS, measured at monitor 5 vs. baseline.

statistical measures, as defined in equations (10) and (11).

6.4. Adding a new monitor survey

A new seismic monitor was acquired in year 5 and the workflow assisted us to quickly diagnose if the simulation models were honoring the new vintage. Fig. 17a and b shows the shape and magnitude error for set S4D_post_WS. Although the data assimilation of set S4D_post_WS did not include monitor 5 (only monitor 3), the metrics suggest the models can honor subsequent seismic vintages. The problematic P5+P6 region improves considerably, and its error shifts to the same level as the other regions, this happens because the gas anomaly becomes weaker due to re-pressurization, visible in the black arrow at the observed map from Fig. 18. The boxplots from Fig. 17 show the highest errors now occur in region P2+P3. This is explained by the blue hardening signal from neighbor region I2 not being contained within this region, extrapolating towards region P2+P3, even at the best ranked models (black arrows from Fig. 20).

Figs. 18 and 19 show respectively the best and worst models considering the shape and magnitude metrics for set S4D_post_WS, measured at the entire reservoir. The worst models picked from both metrics are very similar, which corroborates with the high correlation between the metrics shown in cross plots from Fig. 21.

The subsequent monitor survey was evaluated without having to review any of the methodology parameters, reinforcing the practical and robust aspect of the workflow. Besides, this analysis supports the decision of assimilating new monitors.

7. Conclusions

Selecting the best similarity indicator between predicted and observed 4DS is a very complex task. We developed an automatic tool to convert these multiple models into synthetic seismic maps, and to rapidly evaluate these large datasets according to the observed 4DS. The study was applied in a real case dataset with considerable 4DS signal complexity, with several of variations in terms of shape, magnitude, and sizes.

For the shape metric, we applied a fast, reliable, and unsupervised method that flags mismatches in shapes, sizes, polarity differences, and anomalies absence. We propose a magnitude metric complement that flags seismic magnitude mismatches. The metrics can be obtained successfully on any 4DS vintage, and we suggest further investigation of their use in other domains, such as P-impedance.

The regional similarity metrics provide two information: if the shapes/magnitude inside each region are well matched and if the 4D signal is being contained or not within the regions. The examples demonstrate the importance of region-by-region analysis, as global errors may mask local misfits that are important for further decision-making processes, such as an infill well.

The methodology can be applied in any step of a reservoir management framework to validate possible models, such as ranking and selecting the best models for production forecast and the decision-making process, identifying 4D anomalies not predicted by the dynamic model, for feedback on iterations of geomodelling, and for analyzing new seismic monitors against the current reservoir simulation models. This study lays the groundwork for future research into understanding the impact of the working domain (P-impedances, amplitudes, saturations) into the decision-making process.

Authorship statement

J. M. C. Santos: conceptualization, methodology, formal analysis, investigation, writing. D. R. L. Rosa: provided posterior datasets, results discussions, text revisions. D. J. Schiozer: work supervision, results discussions. A. Davolio: work supervision, results discussions, and text revisions.

Declaration of competing interest

The authors declare that they have no known competing financial interests or personal relationships that could have appeared to influence the work reported in this paper.

Acknowledgements

This work was carried out in association with the ongoing project registered under ANP number 20372-9 as ″Desenvolvimento de integração entre simulação de reservatórios e sísmica 4D - Fase 2″ (UNICAMP/Shell Brazil/ANP) funded by Shell Brasil Petróleo Ltda. under the ANP R&D levy as “Compromisso de Investimentos com Pesquisa e Desenvolvimento”. The authors are grateful for the support of the Center of Petroleum Studies (CEPETRO-UNICAMP/Brazil), the Department of Energy (DE-FEM-UNICAMP/Brazil), the Research Group in Reservoir Simulation and Management (UNISIM-UNICAMP/Brazil) and Energi Simulation. In addition, special thanks to Schlumberger, CGG and CMG for software licenses. We also thank Felipe Mesquita, Frances Abbots, Jorge Lopez and Felipe Vilela for technical discussions.

References

Amini, H., Rodriguez, M., Wilkinson, D., Gadirova, G.R., MacBeth, C., 2019. A case study of effective metrics for history matching the 4D seismic data. In: 81st EAGE Conf. Exhib. https://doi.org/10.3997/2214-4609.201900948, 2019.

Astic, T., Heagy, L.J., Oldenburg, D.W., 2021. Petrophysically and geologically guided multi-physics inversion using a dynamic Gaussian mixture model. Geophys. J. Int. 224, 40–68. https://doi.org/10.1093/gji/ggaa378.

Avansi, G.D., Schiozer, D.J., 2015. A new approach to history matching using reservoir characterization and reservoir simulation integrated studies. Proc. Annu. Offshore Technol. Conf. 6, 4406–4434. https://doi.org/10.4043/26038-ms.

Batzle, M., Wang, Z., 1992. Seismic properties of pore fluids. Geophysics 57, 1396–1408. https://doi.org/10.1190/1.1443207.

Buksh, G., Farmer, H.G., Galarraga, M.A., Lydon, M.T., Mautz, W.A., Norberg, D., 2015. Life of field seismic in the deepwater BC-10 phase 2 development, Brasil. Proc. Annu. Offshore Technol. Conf. 3, 1792–1798. https://doi.org/10.4043/25803-ms.

Chassagne, R., Aranha, C., 2020. A pragmatic investigation of the objective function for subsurface data assimilation problem. Oper. Res. Perspect. https://doi.org/10.1016/j.orp.2020.100143.

Chen, Y., Farmer, H.G., Liu, Z., Lydon, M., Wu, H., 2015. LoFS processing for 4D attributes at the BC10 field – offshore Brazil. Third EAGE Work. Perm. Reserv. Monit. https://doi.org/10.3997/2214-4609.201411967, 2015 2014–2016.

Davolio, A., Schiozer, D.J., 2018. Probabilistic seismic history matching using binary images. J. Geophys. Eng. 15, 261–274. https://doi.org/10.1088/1742-2140/aa99f4.

Derfoul, R., Da Veiga, S., Gout, C., Le Guyader, C., Tillier, E., 2013. Image processing tools for better incorporation of 4D seismic data into reservoir models. J. Comput. Appl. Math. 240, 111–122. https://doi.org/10.1016/j.cam.2012.08.022.

Dovera, L., della Rossa, E., 2011. Multimodal ensemble Kalman filtering using Gaussian mixture models. Comput. Geosci. 15, 307–323. https://doi.org/10.1007/s10596-010-9205-3.

Ebaid, H., Wang, K., Seixas, M., Kumar, G., Brew, G., Mashiotta, T., 2017. Practical example of data integration in a PRM environment, BC-10, Brazil. 1st EAGE Work. Pract. Reserv. Monit. PRM 35, 71–76. https://doi.org/10.3997/2214-4609.201700019, 2017.

Emerick, A.A., Reynolds, A.C., 2013. Ensemble smoother with multiple data assimilation. Comput. Geosci. 55, 3–15. https://doi.org/10.1016/j.cageo.2012.03.011.

Fjeldstad, T., Avseth, P., Omre, H., 2021. A one-step Bayesian inversion framework for 3D reservoir characterization based on a Gaussian mixture model-A Norwegian Sea demonstration. Geophysics 86, R221–R236. https://doi.org/10.1190/geo2020-0094.1.

Formentin, H.N., Almeida, F.l.R., Avansi, G.D., Maschio, Cé, Schiozer, D.J., Caiado, C., Vernon, I., Goldstein, M., 2019. Gaining more understanding about reservoir behavior through assimilation of breakthrough time and productivity deviation in the history matching process. J. Petrol. Sci. Eng.

Gassmann, F., 1951. Elastic Waves through a Packing of Spheres. Geophysics 16, 673–685.

La Rosa Almeida, F., Formentin, H.N., Maschio, C., Davolio, A., Schiozer, D.J., 2018. Influence of additional objective functions on uncertainty reduction and history matching. In: Soc. Pet. Eng. - SPE Eur. Featur. 80th EAGE Conf. Exhib. https://doi.org/10.2118/190804-ms, 2018.

Luo, X., Bhakta, T., Jakobsen, M., Nædal, G., 2016. An ensemble 4D seismic history matching framework with sparse representation based on wavelet multiresolution analysis. Soc. Pet. Eng. - SPE Bergen One Day Semin. 985–1010. https://doi.org/10.2118/180025-ms.

Luo, X., Bhakta, T., Jakobsen, M., Naevdal, G., 2018. Efficient big data assimilation through sparse representation: a 3D benchmark case study in petroleum engineering. PloS one. https://doi.org/10.1371/journal.pone.0198586.

Luo, X., Lorentzen, R.J., Bhakta, T.M., 2021. Accounting for model errors of rock physics models in 4D seismic history matching problems: a perspective of machine learning. J. Petrol. Sci. Eng. https://doi.org/10.1016/j.petrol.2021.109728.

Maleki, M., Danaei, S., Davolio, A., Schiozer, D.J., 2019. Fast-track qualitative interpretation of seismic data in a permanent reservoir monitoring PRM setting for a Brazilian field. In: Proc. - SPE Annu. Tech. Conf. Exhib. 2019-Septe. https://doi.org/10.2118/196185-ms.

Maleki, M., Danaei, S., Mesquita da Silva, F.B., Davolio, A., Schiozer, D.J., 2021. Stepwise uncertainty reduction in time-lapse seismic interpretation using multi-attribute analysis. Petrol. Geosci. 27 https://doi.org/10.1144/petgeo2020-087 petgeo2020-087.

Maschio, C., Avansi, G.D., da Silva, F.B.M., Schiozer, D.J., 2021. Data assimilation for uncertainty reduction using different fidelity numerical models. J. Petrol. Sci. Eng. https://doi.org/10.1016/j.petrol.2021.109851.

Mavko, G., Mukerji, T., Dvorkin, J., 1998. The Rock Physics Handbook.

Obidegwu, D., Chassagne, R., MacBeth, C., 2015. Seismic assisted history matching using binary image matching. EUROPEC 1119–1140. https://doi.org/10.2118/174310-ms, 2015.

Oliver, D.S., Alfonzo, M.A., 2018. Seismic data assimilation with an imperfect model. In: 16th Eur. Conf. Math. Oil Recover. ECMOR. https://doi.org/10.3997/2214-4609.201802283, 2018 889–905.

Oliver, D.S., Fossum, K., Bhakta, T., Sandø, I., Nævdal, G., Lorentzen, R.J., 2021. 4D seismic history matching. J. Pet. Sci. Eng. 207, 109119. https://doi.org/10.1016/j.petrol.2021.109119.

Rollmann, K., 2020. Klaus Rollmann Techniques for Comparing 4D Seismic Data in Oil Reservoir Fields Técnicas para Comparação de Imagens Sísmicas 4D em Campos de Petróleo.

Santos, J.M.C., Schiozer, D.J., Davolio, A., 2020. Multi attribute approach for quantifying competing time lapse effects and implications for similarity indicators in data assimilation. In: Proc. - SPE Annu. Tech. Conf. Exhib. 2020-Octob. https://doi.org/10.2118/201426-ms.

Schiozer, D.J., Avansi, G.D., de Souza dos Santos, A.A., 2017. Risk quantification combining geostatistical realizations and discretized Latin Hypercube. J. Brazilian Soc. Mech. Sci. Eng. 39, 575–587. https://doi.org/10.1007/s40430-016-0576-9.

Schiozer, D.J., De Souza Dos Santos, A.A., De Graçą Santos, S.M., Von Hohendorff Filho, J.C., 2019. Model-based decision analysis applied to petroleum field development and management. Oil Gas Sci. Technol. 74 https://doi.org/10.2516/ogst/2019019.

Seydoux, L., Balestriero, R., Poli, P., Hoop, M. de, Campillo, M., Baraniuk, R., 2020. Clustering earthquake signals and background noises in continuous seismic data with unsupervised deep learning. Nat. Commun. 11 https://doi.org/10.1038/s41467-020-17841-x.

Soares, R.V., Luo, X., Evensen, G., Bhakta, T., 2020. 4D seismic history matching: assessing the use of a dictionary learning based sparse representation method. J. Petrol. Sci. Eng. 195, 107763. https://doi.org/10.1016/j.petrol.2020.107763.

Soriano-Vargas, A., Rollmann, K., Almeida, F., Davolio, A., Hamann, B., Schiozer, D.J., Rocha, A., 2020. A synthetic case study of measuring the misfit between 4D seismic data and numerical reservoir simulation models through the Momenta Tree. Comput. Geosci. 145 https://doi.org/10.1016/j.cageo.2020.104617.

Souza, R., Lumley, D., Shragge, J., Davolio, A., Schiozer, D.J., 2018. Analysis of time-lapse seismic and production data for reservoir model classification and assessment. J. Geophys. Eng. 15, 1561–1587. https://doi.org/10.1088/1742-2140/aab287.

Stammeijer, J.G.F., Hatchell, P.J., 2014. Standards in 4D feasibility and interpretation. Lead. Edge 33, 134–140. https://doi.org/10.1190/tle33020134.1.

Tillier, E., Da Veiga, S., Derfoul, R., 2013. Appropriate formulation of the objective function for the history matching of seismic attributes. Comput. Geosci. 51, 64–73. https://doi.org/10.1016/j.cageo.2012.07.031.

Trani, M., Wojnar, K., Moncorgé, A., Philippe, B., 2017. Ensemble-based assisted history matching using 4d seismic fluid front parameterization. In: SPE Middle East Oil Gas Show Conf. MEOS, Proc., pp. 640–652. https://doi.org/10.2118/183901-ms, 2017-March.

Wallet, B.C., Hardisty, R., 2019. Unsupervised seismic facies using Gaussian mixture models. Interpretation 7. https://doi.org/10.1190/int-2018-0119.1. SE93–SE111.

Zhang, Y., Leeuwenburgh, O., 2017. Image-oriented distance parameterization for ensemble-based seismic history matching. Comput. Geosci. 21, 713–731. https://doi.org/10.1007/s10596-017-9652-1.

Zhao, Y., Li, G., Reynolds, A.C., 2007. Characterization of the measurement error in time-lapse seismic data and production data with an EM algorithm. Oil Gas Sci. Technol. 62, 181–193. https://doi.org/10.2516/ogst:2007016.

APPENDIX E – PUBLICATION PERMISSIONS

The following license agreements grant permission to republish the manuscripts in this thesis.

CCC | Marketplace

Order Date	28-Mar-2023	Type of Use	Republish in a thesis/dissertation
Order License ID	1338923-1	Publisher	Society of Petroleum Engineers
ISBN-13	9781613997239	Portion	Chapter/article

LICENSED CONTENT

Publication Title	SPE Annual Technical Conference & Exhibition (20ATCE)	Country	United States of America
Date	01/01/2020	Rightsholder	Society of Petroleum Engineers (SPE)
Language	English	Publication Type	e-Book

REQUEST DETAILS

Portion Type	Chapter/article	Rights Requested	Main product
Page Range(s)	1-9	Distribution	Worldwide
Total Number of Pages	9	Translation	Original language of publication
Format (select all that apply)	Electronic	Copies for the Disabled?	No
Who Will Republish the Content?	Academic institution	Minor Editing Privileges?	No
Duration of Use	Life of current edition	Incidental Promotional Use?	No
Lifetime Unit Quantity	Up to 499	Currency	USD

NEW WORK DETAILS

Title	Diagnosing Reservoir Models Using Similarity Indicators with 4D Seismic Data: A Multi-Domain and Multi-Attributes Approach	Institution Name	UNICAMP
		Expected Presentation Date	2023-03-30
Instructor Name	Prof. Dr. Alessandra Davolio		

ADDITIONAL DETAILS

Order Reference Number	N/A	The Requesting Person/Organization to Appear on the License	Juliana M C Santos

REQUESTED CONTENT DETAILS

Title, Description or Numeric Reference of the Portion(s)	Multi Attribute Approach for Quantifying Competing Time Lapse Effects and Implications for Similarity Indicators in Data Assimilation (SPE-201426-MS)	Title of the Article/Chapter the Portion Is From	SPE Annual Technical Conference and Exhibition, Virtual, October 2020.
		Author of Portion(s)	Juliana Maia Santos; Denis José Schiozer; Alessandra Davolio
Editor of Portion(s)	Juliana M C Santos	Issue, if Republishing an Article From a Serial	N/A
Volume of Serial or Monograph	N/A		
Page or Page Range of Portion	1-9	Publication Date of Portion	2020-10-19

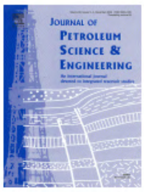

Fast diagnosis of reservoir simulation models based on 4D seismic similarity indicators

Author: Juliana Maia Carvalho dos Santos,Daiane Rossi Rosa,Denis José Schiozer,Alessandra Davolio

Publication: Journal of Petroleum Science and Engineering

Publisher: Elsevier

Date: March 2022

Journal Author Rights

Please note that, as the author of this Elsevier article, you retain the right to include it in a thesis or dissertation, provided it is not published commercially. Permission is not required, but please ensure that you reference the journal as the original source. For more information on this and on your other retained rights, please visit: https://www.elsevier.com/about/our-business/policies/copyright#Author-rights

BACK | CLOSE WINDOW